ABSTRACT

Title of Dissertation: FABRICATION AND FUNDAMENTAL STUDIES OF A 4-KW, VARIABLE-VOLTAGE, DISTRIBUTED HYBRID-ELECTRIC POWERTRAIN FOR EVTOL AIRCRAFT

Brent Mills,
Doctor of Philosophy, 2022

Dissertation directed by: Professor Anubhav Datta
Department of Aerospace Engineering

In this research, a small-scale, 4-Kw, variable-voltage, hybrid-electric powertrain was constructed and tested to understand the fundamental behavior of such a system. The powertrain is meant for distributed propulsion for a multirotor electric vertical take-off and landing (eVTOL) aircraft. The powertrain was examined component by component, as well as in combination with one to four distributed rotors. Steady-state mathematical models for the engine, generator, and motor were developed for performance and weight. The component models were calibrated with the test data. It was found that a simple physics-based model of brake specific fuel consumption (bsfc) is possible to build if certain thermal efficiency constants could be calibrated with test data. The impact of various losses on the electric motor efficiency plots were revealed. Statistical weight models were developed by gathering a database of commercial reciprocating engines, electric motors, and power electronics, which were accurate to within ±30%. However, given the importance of electric motors for eVTOL design, a geometry- and material-based model was also developed. This model was accurate to within a 6% average error.

The principal findings of this work are that the generator voltage is a key parameter in a hybrid-electric powertrain, and engine efficiency is closely coupled to the controls and aeromechanics of an eVTOL aircraft. The ability to vary the generator voltage with operating state appears crucial for the optimal specific fuel consumption. Generator voltage is a function of engine speed. For any operating state—defined by rotor torque and RPM—the generator voltage should be minimized as far as possible. However, generator voltage limits the maximum rotor RPM; so not all rotor RPM can be achieved at the same generator voltage. Hence, the optimal generator voltage will vary with rotor RPM as needed during specific mission segments. This implies for an RPM controlled aircraft, generator voltage is not simply a criterion for design but also for control, if the optimal bsfc is to be achieved. Additionally, for any generator voltage and rotor RPM, there is a rotor torque that maximizes overall efficiency, i.e., minimizes bsfc. A method for adjusting the rotor torque, such as collective pitch control, is also desired if the optimal bsfc is to be achieved. Therefore, the most efficient change is power results from a combination of reducing engine RPM and increasing rotor torque and vice versa.

In summary, a hybrid-electric powertrain is an attractive option for multi-rotor aircraft if it is judiciously designed together with the platform. It is hoped that the data generated in this dissertation and the accompanying understanding will help the future designer accomplish this task.

FABRICATION AND FUNDAMENTAL STUDIES OF A 4-KW,VARIABLE-VOLTAGE, DISTRIBUTED HYBRID-ELECTRIC POWERTRAIN FOR eVTOL AIRCRAFT

by

Brent Mills

Dissertation submitted to the Faculty of the Graduate School of the
University of Maryland, College Park, in partial fulfillment
of the requirements for the degree of
Doctor of Philosophy
2022

Advisory Committee:
Professor Anubhav Datta, Chair/Advisor
Professor Inderjit Chopra
Professor James Baeder
Professor Allison Flatau
Professor Nikhil Chopra

Dedicated to my wife and children. Without their constant love and support this would not be possible.

I would like to acknowledge to support of my Army coworkers as well as the University of Maryland's staff, faculty, and fellow students that helped make this possible.

This work was performed at the University of Maryland's Alfred Gessow Rotorcraft Center, in collaboration with the U.S. Army Combat Capabilities Development Command Data and Analysis Center, with technical monitoring from Mr. Rick Grote. Additional support was provided by the U.S. Army Research Laboratory Cooperative Research Agreement (W911NF1620155), with technical monitoring from Dr. Rajneesh Singh, and the Vertical Lift Research Center of Excellence (W911W61120012), with technical monitoring from Dr. Mahendra Bhagwat and Dr. William Lewis. We gratefully acknowledge these supports.

Table of Contents

List of Tables

List of Figures

Chapter 1: Introduction

This chapter introduces the topic of this dissertation. It describes the motivation of the research, a description of the problem, and a survey of past work to bring the reader up to the state-of-the-art.

1.1. Distributed Propulsion in Large Aircraft

For multi-rotor Vertical and/or Short Takeoff and Landing (V/STOL) aircraft, distributed propulsion appear to promise certain desirable attributes. Distributed propulsion in rotorcraft means multiple rotors providing lift and thrust, a terminology usually reserved for four or more rotors to distinguish from conventional single main rotor, coaxial, tiltrotor, and compound helicopters. The perceived advantages include weight reduction due to swashplate elimination, better maneuverability, improved gust stability and station keeping from thrust vectoring, and increased safety and survivability due to propulsor redundancy. However, lack of systematic experimentation, test data, and peer review have prevented any clear or concrete conclusions.

In large aircraft, distributed propulsion attempts have been historically through mechanical means. Experimental aircraft such as the Curtiss-Wright X-19 [1], shown in Figure 1.1, and the Bell X-22 [2], shown in Figure 1.2, were flown during the 1960s but were plagued by weights. Another experimental aircraft flown during the 1960s was the Ling-Temco-Vought XC-142A [3], shown in Figure 1.3, which suffered major problems specifically related to inter-connecting drive shafts. All three crashed during prototype testing and none were carried to production. Thus historically, distributed propulsion has been infeasible in large aircraft due to the prohibitive weight and complexity of mechanical transmissions. In Reference 4, Gohardani postulates that electric propulsion could provide a revolutionary breakthrough, if the transmission can be made electric at dramatically lighter weight.

Figure 1.1. Curtiss-Wright X-19 experimental VTOL passenger transport

Figure 1.2. Bell X-22 experimental V/STOL troop transport

Figure 1.3. Ling-Temco-Vought XC-142A experimental V/STOL cargo transport

1.2. Distributed Propulsion in Small Aircraft

Many small-scale unmanned-aerial-systems have distributed propulsion with battery-powered electric transmission. Batteries are a direct current (DC) power source, and they can be connected directly to multiple inverter-fed electric motors. The inverter converts DC to alternating current (AC). The motors are AC permanent-magnet synchronous (PMS) machines, commonly constructed with trapezoidal windings and fed with trapezoidal currents—the so-called brushless DC motors. They scale proportionally with torque and have good specific power, but batteries have poor specific energy and are too heavy for the kind of range, endurance, and payload desired for military missions. In this case the power source is the principal barrier not the transmission. Thus, in small aircraft, distributed propulsion has been all-electric, which eliminated the transmission problem but are starved of energy.

1.3. Distributed Propulsion in Large eVTOL

The concept of electric distributed propulsion is now being scaled up to light-VTOL aircraft meant for manned flight. These aircraft are considered electric vertical takeoff and landing (eVTOL) aircraft, that is to say a manned aircraft that uses electric power to hover, takeoff and land vertically. The Vertical Flight Society maintains a database of over 650 eVTOL concepts and prototypes. The propulsion efficiency is expected to improve dramatically with an electric drive, since the RPM can now be easily varied in flight with reductions down to 30-40% of the hover RPM without a significant loss in motor efficiency. This reduction can have dramatic impact on aircraft lift to drag ratios for both edgewise and prop-rotor flight. Additionally, rapid transients can eliminate the need for a swashplate and enable simpler vehicle controls, similar to small drones. Obviously, these aircraft are even more burdened by the same problem as the small aircraft—energy-starved batteries. One possible avenue to relieve this burden is to retain the combustion engine of the large aircraft but introduce the electric transmission of the small aircraft to harness the best of both technologies [5]. The objective of this research is to explore this concept.

1.4. Motivation

To achieve the benefits of distributed propulsion, while maintaining significant ranges and payload, new powertrains are required. The use of electric transmissions has eliminated the mechanical complexity and weights that plagued earlier mechanical attempts. While batteries are suitable for small-scale distributed propulsion aircraft, they are energy starved limiting range and payload. As a result, current eVTOL aircraft are typically limited in range and payload due to their reliance on batteries. Hybrid-electric powertrains may be the key enabler for distributed propulsion in eVTOL due to the high energy density of gasoline and diesel while still eliminating the mechanical transmission. However, there is a lack of systematic experimentation and test data of this concept. The intent of this research is to fill this void, albeit in a small-scale.

1.5. Brief History of Electric and Hybrid-Electric Transportation

The history of electric transportation begins in 1880 with the first public electric tramway in St. Petersburg, Russia. However, individual electric transportation did not begin until 1890 with the first practical electric car utilizing a lead/acid battery. Then in 1916 one of the first hybrid-electric cars, the Owen Magnetic, was produced. However, by 1935 electric car production had all but ended at large scale. From 1930, advances in electric cars were minimal until 1971 with the electric lunar rover. Then in 1975 the USPS electric jeep became the first production vehicle with regenerative braking. However, it was not until 1997 that the first modern hybrid-electric car sparked individual all-electric and hybrid-electric car production. Today all-electric and hybrid-electric automobiles have become a core segment of the market.

During the same period, advances in electric propulsion were also being made in naval vessels. In 1887, the first parallel hybrid-electric submarine, later christened the USS Holland, was introduced. The USS Holland utilized a 34-kW, 4-stroke gasoline engine for surface running and to charge a lead-acid storage battery to power a 37-kW DC commutation motor for under water operations. Shortly thereafter, diesel-electric powertrains became common place in navies across the globe. Then in 1913, the first turbo-electric ship, the USS Jupiter, later commissioned as the USS Langley, was developed. The ship utilized two coal-boiler and a Curtis steam turbine to power a primary 5,000 kW AC turbogenerator and three 35-kw DC generators (service power). The primary generator powered two wound-rotor, induction motors, which twinned the propellers, for primary propulsion. By 1927, six turbo-electric battleships and two turbo-electric aircraft carriers had entered U.S. Navy service. Both the diesel-electric and turbo-electric powertrains continued to be advanced in naval vessels. In 1957, nuclear-boilers with steam turbines were utilized in the turbo-electric powertrains for the USS Tullibee submarine and the Lenin icebreaker. Today, both the diesel-electric and turbo-electric powertrains are still used in marine transportation and have transitioned to locomotive and heavy-construction usages.

Advances in electric aviation lagged behind electric land and naval vehicles until electric motor power-to-weight ratios and power sources became more suitable for aviation usages. As such electric aviation matured first with small-scale unmanned technology in 1957, with the first officially recorded unmanned radio-controlled fixed-wing aircraft. Then in 1973, the first manned flight of an electric fixed-wing aircraft was conducted in 1973 by Fred Militky, an early pioneer in unmanned gliders, with the self-launching MB-E1 motor glider, Figure 1.4. The Militky Brditschka MB-E1 motor glider utilized a 10-kW electric motor and nickel-cadmium batteries for powered flight.

Figure 1.4. Fred Militky and the Militky Brditschka MB-E1 motor glider

However, it was not until 2003 that the Lange Antares 20E became the first production self-launching, electric glider. Electric concepts continued to advance electric powered-flight with the Antares DLR-H2 and Boeing Dimona in 2009. In 2011 NASA Centennial challenge for greener aviation, manned fixed-wing electric aviation, was primarily limited to high-lift platforms like gliders and sailplanes due to power and weight requirements. Eight all-electric and one hybrid-electric concepts were submitted for the NASA Centennial challenge for greener aviation, sparking additional concepts from individual electric fixed-wing aircraft to regional and continental airliners.

More than for electric, fixed-wing aviation, Electric, rotor-wing aviation matured first with micro- and small-scale unmanned technology. Academic programs like the U.S Army Research Laboratory CTA-MAST in 2008 advanced the state-of-art in rotor-wing micromechanics, controls, and logistics. In 2009, the first commercially successful unmanned VTOL drone, the Parrot AR, was introduced. The first manned eVTOL flights occurred in 2011 with Solution F/Chretien Helicopter, shown in Figure 1.5, and the Volocopter VC1 shown in Figure 1.6. Battery power, however, has kept large-scale aircraft with practical range and payload out of scope. The Workhorse Surefly, introduced in 2018, was one of the first hybrid-electric eVTOL aircraft to undergo flight testing. The inclusion of the hybrid-electric powertrain was intended to enable a significant increase in range and payload, although there is no published data. With the advent of the Urban Air Mobility initiative, over 650 eVTOL concepts have been introduced since 2016. Most, if not all, are battery powered aircraft. The hybrid-electric option has been less investigated.

Figure 1.5. Pascal Chretien and the Solution F/Chretien Helicopter eVTOL helicopter in flight

1.6. Review of Hybrid-Electric Powertrains for Fixed-Wing Aircraft

Large-scale concepts for hybrid-electric powertrains have not been physically realized. However, there have been small- and mid-scale hybrid-electric powertrain concepts and efforts that present useful data for fixed-wing aircraft. Table 1.1 summarizes a recent survey of small- and mid-scale for fixed-wing aircraft. These aircraft are primarily motor gliders, capable of sustained soaring flight without propulsive thrust, with modified propulsion systems.

Figure 1.6. Volocopter VC1 eVTOL helicopter in flight

Table 1.1. Manned, hybrid-electric, fixed-wing aircraft utilizing internal combustion engine generators

Organization	Year	Aircraft Type	MTOW (kg)	Power (kW)	Battery Power	Battery Recharge	Data Published
Cambridge University	2010	Fixed Wing	235	12	Yes	No	No
Embry-Riddle Aeronautical University	2011	Fixed Wing	980	30	Yes	No	Limited
Siemens, EADS, Diamond Aircraft	2011	Fixed Wing	770	70	Yes	Yes	No
Cambridge University	2014	Fixed Wing	235	12	Yes	Yes	Limited
Siemens, EADS, Diamond Aircraft	2018	Fixed Wing	NA	150	Yes	Yes	No

In 2010, the Engineering Department at the University of Cambridge in association with Flylight Airsports Ltd, modified the powertrain of a Alatus-M motor glider with a parallel-hybrid-electric powertrain for flight testing, Figure 1.7. A Lithium-ion polymer battery was used to power an 11.2-kW brushless DC motor to supplement the 2.2-kW four-stroke engine during take-off, climb, and cruise. The hybrid-electric powerplant was successfully demonstrated in flight testing; however, the system was underpowered. While the basic system information was published in the Council of European Aerospace Societies (CEAS) Aeronautical Journal [6], the flight test data was not published. Similarly, individual characterization of the components and powertrain is not available.

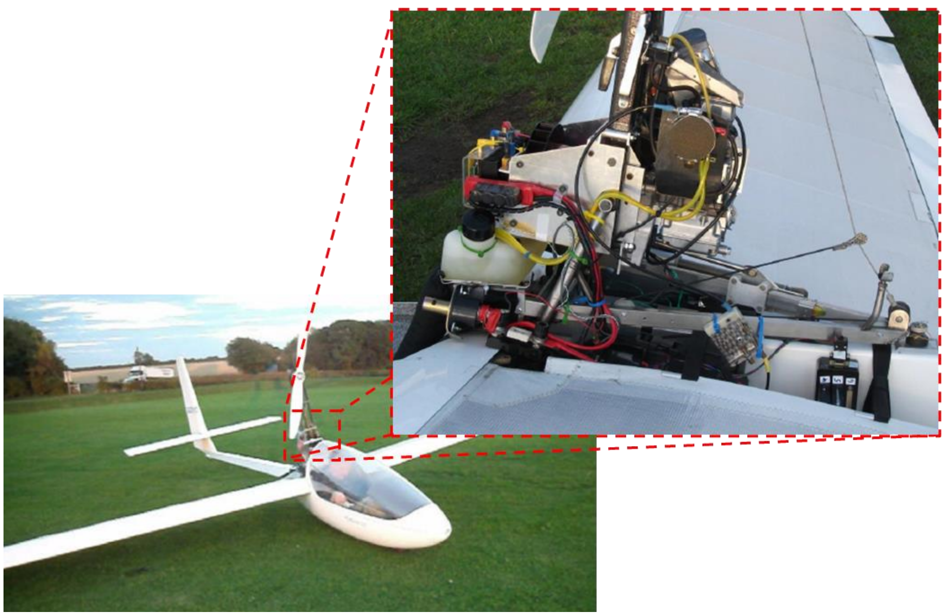

Figure 1.7. Cambridge University Hybrid-Electric Alatus-M.

In 2011, the Aerospace Engineering Department at the Embry-Riddle Aeronautical University Eagle Flight Research Center modified the powertrain of a Stemme S10 self-launching sailplane with a parallel-hybrid-electric powertrain, Figure 1.8. A 75-kW Rotax 912 engine was used to provide take-off and climb power. A Lithium-ion Polymer battery was used to power a 30-kW brushless DC motor to provide cruise power. The Eco-Eagle was developed as a demonstrator for the NASA's Green Flight Challenge competition. This work demonstrated the feasibility of electric-powered cruise flight and examined the effects of aircraft lift and drag on performance for electric aircraft. Details on the powertrain and design are published in M.S. theses. However, the full flight test data was not published. Similarly, individual characterization of the components and powertrain is not available.

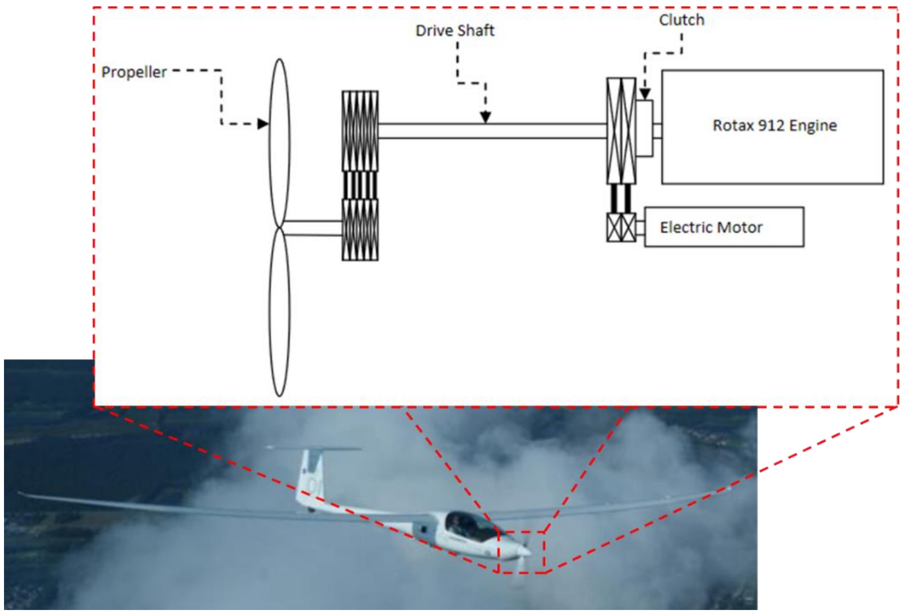

Figure 1.8. Embry-Riddle Aeronautical University Eco-Eagle.

In 2011, Siemens in collaboration with the European Aeronautic Defence and Space Company (EADS) and Diamond Aircraft, modified a HK 36 Super Dimona motor glider with a serial-hybrid electric powertrain, the DA 36 E-Star, Figure 1.9. A 30-kW Wankel engine/generator module was electrically coupled to a 70-kW brushless motor. A battery system provided supplemental power to the motor during take-off and climb. The battery is recharged with excess power during the cruise phase. Flight testing, conducted in 2011, demonstrated the feasibility of a serial hybrid-electric aircraft. A second-generation design was also flight tested in 2013. The E-star demonstrated noise reduction during electric take-off and a reduction in fuel consumption and emissions due to the hybrid-electric powertrain. While the powertrain was documented in press releases and tradeshow briefings, the flight data was not published. Similarly, individual characterization of the components and powertrain is not available.

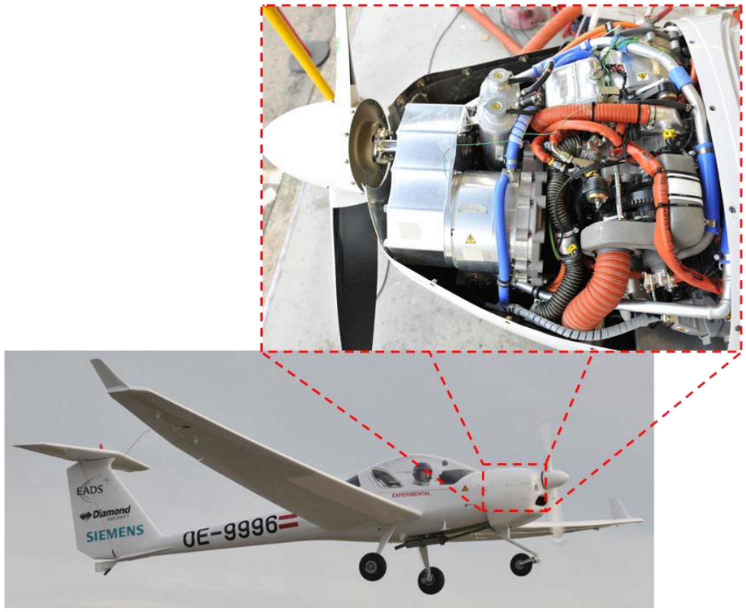

Figure 1.9. Siemens, EADS, Diamond Aircraft DA 36 E-Star.

In 2014, the Engineering Department at the University of Cambridge in association with Gramex, modified a motorized SONG glider with additional wing area and a parallel-hybrid-electric powertrain, Figure 1.10. An 8-kW Honda GX160 is supplemented by a 12-kW JM1 Joby motor. The powertrain and design analysis were published in the CEAS Aeronautical Journal [6]. The powertrain could operate in an engine-only, electric-motor-only, and hybrid modes. The performance references of mission points, based on aircraft speed, as well as limited engine and electric motor characterizations were published [7]. Additionally, an informational briefing contains test data from one of the test flights. Flight tests, conducted in 2014, demonstrated that reduction in fuel consumption proportional to the electrical/mechanical power balance. However, a full characterization of the components, powertrain, and flight data was not published.

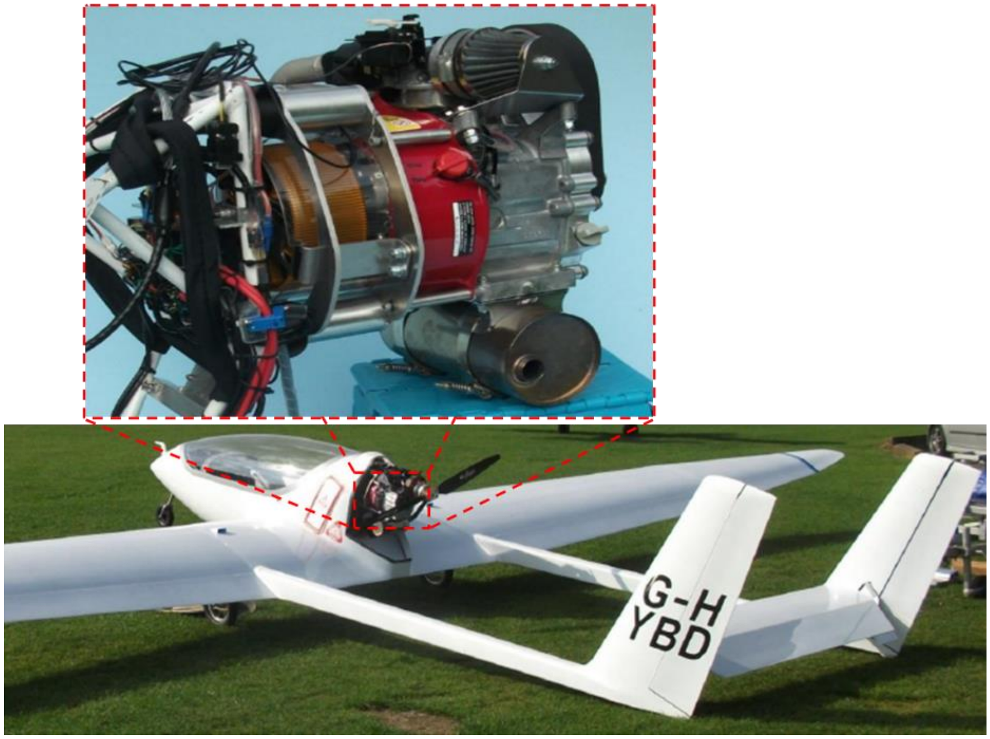

Figure 1.10. Cambridge University Hybrid-Electric Gramex SONG

In 2018, Siemens in collaboration with the EADS and Diamond Aircraft, modified a DA 40 light aircraft with serial-hybrid electric powertrain, Figure 1.11. A 110-kW Diesel engine/generator module was electrically coupled to two 75-kW brushless motor (150-kW combined power). A 24-kWh battery system provided supplemental power to the motor in response to pilot battery controls. The system operates in a pure electric mode (100 % battery), cruise mode (100% generator), and charge mode (generator recharges the batteries). Flight testing, conducted in 2018, demonstrated the feasibility of a serial hybrid-electric aircraft with distributed propulsors. The aircraft has a hybrid power endurance of 5 hrs. In this aircraft the energy production, energy storage, and thrust generation locations are separate. While the powertrain was documented in press releases and tradeshow briefings, the flight data was not published. Similarly, individual characterization of the components and powertrain is not available.

Figure 1.11. Siemens, EADS, Diamond Aircraft Hybrid-Electric DA 40.

1.7. Review of Hybrid-Electric Powertrains for Rotor-Wing Aircraft

Similar to hybrid-electric powertrains for fixed-wing aircraft, there have been small- and mid-scale concepts and efforts that present useful data for rotor-wing aircraft. Table 1.2 summarizes a recent survey of small- and mid-scale for rotor-wing aircraft.

Table 1.2. Manned, hybrid-electric, rotor-wing aircraft utilizing internal combustion engine generators

Organization	**Year**	**Aircraft Type**	**MTOW (kg)**	**Power (kW)**	**Battery Power**	**Battery Recharge**	**Data Published**
Oregon State University	2017	VTOL	<25	1	Yes	Yes	Yes
Workhorse	2018	VTOL	680	150	Emergency	NA	No
Launchpoint EPS	2021	VTOL	40.5	5.5	Transient	Transient	Limited

In 2017, the Energy Systems Engineering Department at Oregon State University developed a 1-kW quad-rotor UAV with a serial-hybrid-electric powertrain, Figure 1.12. A 2.5-kW two-stroke, 3W-28i engine was connected to a KDE 8218 brushless DC motor generator with KDE UAS-95 electronic speed controller with synchronous rectification. The engine operated at 1.25 kW to charge lithium-ion batteries. The electric motors for the rotors were powered solely by the batteries. Flight tests, conducted in 2017, demonstrated that significant (~3.5x) range and endurance increases when compared to an all-electric quadcopter. Some engine performance as a function of fuel pulse width and ignition timing was published as an American Society of Mechanical Engineers conference paper [8]. Generator performance as a function rectifier duty cycle was published as part of a M.S. thesis. Motor, battery, and engine specific fuel consumption characteristics were published in the Journal of Propulsion and Power [9].

Figure 1.12. Oregon State University Hybrid-Electric UAV

In 2018 Workhorse, an electric vehicle company, developed the SureFly, a two-seat hybrid-electric VTOL aircraft, shown in Figure 1.13 (now the Moog SureFly). A 150-kW gasoline engine/generator module used to power eight brushless motors (150-kW combined power). A battery system of four Lithium-ion packs was provided for emergency backup. Flight testing demonstrated the feasibility of a serial hybrid-electric VTOL aircraft with distributed propulsors without intermediate batteries and recharging. While the powertrain was documented in press releases and tradeshow infographics, there were no scientific publications. Similarly, individual characterization of the components and powertrain was not available.

Figure 1.13. Workhorse Surefly Hybrid-Electric Octocopter

In 2021, Launchpoint EPS in collaboration with Offshore Aviation LLC, modified an OA-8C quad copter with HPS055 serial-hybrid electric powertrain, Figure 1.14. The HPS055 is a 5.5-kW serial-hybrid-electric powertrain. The system utilizes a battery set to supply transient power requirements increasing response time and reducing the risk of overloading the engine. In contrast to the limited published data from of the previously detailed endeavors, this contemporary effort published the developmental and flight test results as a Vertical Flight Society conference paper [10]. The paper gave details of the system specifications and the power management unit developed to control the engine in response to changing power requirements. The power sharing between the generator and battery system with programmable loads on a test bed were also documented. Then two test flights were reported, with voltage and current data reported as a function of altitude and flight speed. The paper demonstrated an increase in endurance (~4x) when compared to an equivalent all-electric battery system. Additionally, the paper examined the requirements of the hybrid-electric system in supplying power for transient take-off and climb conditions. The paper demonstrated that batteries can be strategically included to improve transient responses as well as take-off. The generator set, battery, and power management unit were integrated and testing in a laboratory test cell as well as flight test vehicle as a function of voltage and current. However, an individual characterization of all components to include fuel consumption and efficiency were not included.

Figure 1.14. Launchpoint EPS/Offshore Aviation Hybrid-Electric VTOL UAV.

1.8. Definition of Distributed, Hybrid-electric Powertrains

There is a vast literature on hybrid-electric powertrains in automobiles. So, it is important to make a clear distinction between these and those envisioned for aircraft.

A common design in automobiles is the parallel-hybrid system were the engine and electric motor connects to the driveshaft through mechanical coupling and the driveshaft can be powered by both. The purpose of this hybridization is to increase fuel economy through regenerative braking that charges a battery, and to provide supplemental power from an alternative (e.g., battery) source. A second common design is the series-hybrid system where the motor connects directly to a generator, and the drive is powered by a separate motor. The purpose of this hybridization is to increase fuel economy by isolating the engine from demand, allowing it to consistently operate at its most efficient speed. In both systems, the wheels are typically connected to mechanical differentials and not independently controlled by the drive motors [11].

An aircraft lacks regenerative braking regimes where batteries could be recharged [12,13,14,15]. As such batteries are parasitic and should not be the primary components of hybridization. However, they might be used for strategic purposes, such as increasing transient power responses, low-noise flight, and emergency power backups. Additionally in rotorcraft with distributed-propulsion rotors with independent control are desired. Thus, from generation to transmission to distribution, a distributed eVTOL powertrain bears little resemblance to an automobile powertrain.

In this work, we define a distributed, hybrid-electric powertrain as one where the primary power source is still a combustion engine, but the shaft power is converted first to electrical power by a generator, and then transmitted to distributed motors by wires as shown in Figure 1.15. The generator produces AC power. This power is converted first to DC power by a rectifier. The rectifier would also allow power to be supplemented by another DC source, although that is not pursued in this work. More importantly, the rectifier allows for independent control of the motors. This independent control is essential for eVTOL aircraft where varying rotor speed (revolutions per minute (RPM)) independently for multiple rotors is a key attraction for electric propulsion. Thus, the mechanical drive is now eliminated and replaced with a generator, electric motors, and accompanying accessories.

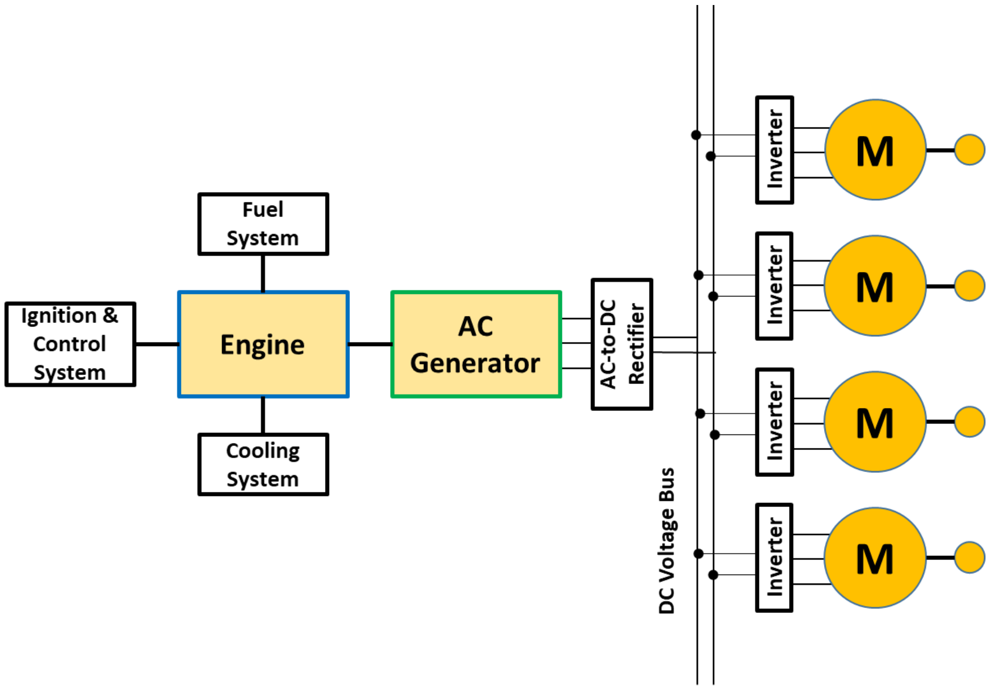

Figure 1.15. Block Diagram of the Distributed, Hybrid-Electric Powertrain.

1.9. Objective of Dissertation

The objective is to design, fabricate, and conduct fundamental studies on a 4-kW, variable-voltage, distributed, hybrid-electric powertrain for eVTOL aircraft component by component.

1.10. Outline of the Dissertation

As part of this research, first a fundamental characterization of a 4-kW, variable-voltage hybrid-electric powertrain was conducted. This characterization included the piston engine, electric generator, and electric motor performance individually and in combination, for single and distributed drives [16]. Second, steady-state mathematical models of the engine, generator, and motor performance were developed based on operational theory and fundamental phenomena. The component models were then validated with the database. Finally, component weight models were developed, based on geometry and materials, and validated with commercial weight data where available.

The dissertation is organized into seven chapters. Following Chapter 1, Chapters 2 and 3 deal with the fundamental characterization of the powertrain. Chapter 2 details the powertrain design and fabrication. Revelation of key barriers with regards to engine startup and operation for future integration are presented. Chapter 3 reports the fundamental characterization study for the powertrain. Chapters 4-6 deal with the performance and weight modeling. Chapter 4 develops the performance and weight models for a two-stroke piston engine. Chapter 5 develops the performance and weight models for an AC PMS motor/generator. Chapter 6 presents validation of the models with the integrated powertrain. Throughout, fundamental understanding is stressed. Finally, Chapter 7 lists the key conclusions.

Chapter 2: Design and Fabrication of the Powertrain

This chapter describes the design and fabrication of the 4-kW, variable-voltage hybrid electric powertrain. It includes the architecture of the powertrain, components of the powertrain (engine, generator, motors, power electronics), instrumentation and integration.

2.1. Introduction

In 2018, University of Maryland conducted a scalability study of quadrotor, biplane, tailsitter (QBiT) aircraft configuration [17]. QBiT concepts of 1,000-, 50-, and 20-lb gross weight were developed with a generalized sizing analysis. The 50-lb concept included an all-electric powertrain, as well as a hybrid-electric. This 50-lb hybrid-electric concept considered a 3-kW piston engine to provide 2.5-kW rotor power. That is the objective powerplant for this dissertation. In collaboration with the U.S. Army Research Laboratory, a smaller 8-lb QBit was built, flown, and then later scaled up to a 20-lb aircraft to establish the feasibility of the 50-lb concept. These were all battery powered aircraft. A 50-lb aircraft of similar type is the Bell APT-20. The APT-20 is also a battery-powered aircraft. The powerplant developed in this dissertation is meant for this class of aircraft.

2.2. Powertrain Architecture

With power specified, a detailed design schematic was built with commercial off-the-shelf components, as shown in Figure 2.1. Figure 2.1 details the mechanical and electrical connections of the powertrain and its data collection requirements. The engine system, top right, consists of the engine, an ignition timing module, and a DC power supply. The DC power supply powers the ignition timing module which has an electrical connection for the sparkplug on each cylinder of the engine. The engine throttle is controlled by a throttle lever which should be connected to a servo-actuator and controlled with a pulse-width modulation signal. The engine will require an external fuel system. To characterize the engine system, the fuel mass consumed, output torque, and the output angular velocity should be measured. The angular velocity of the engine can be measured utilizing the ignition timing signals. However, engine torque requires a separate torque transducer. As such the engine output shaft is mechanically connected to a shaft-to-shaft torque transducer.

The generator system, left, consists of the generator and an AC-to-DC rectifier. The generator input shaft is mechanically coupled transducer shaft opposing the engine output shaft. The generator input torque and angular velocity is the same as the engine output shaft due to the no-slip conditions shaft-to-shaft coupling. As such the torque and angular velocity are transmitted to the permanent magnet rotor of the generator which induce a three-phase electromotive voltage and current. The electric wire of each phase is connected to the input block of an AC-to-DC rectifier. The DC voltage of the generator system should be measured at the DC output block of the rectifier. Current can be measured at the same location. Note, that current requires a closed DC circuit.

The drive system, lower right, consisted of the individual AC permanent magnet synchronous (ACPMS) motors and their respective electronic speed controllers (ESC). The ESCs are connected in parallel to the DC output block of the rectifier. The ESC converts the supplied DC voltage three-phase voltage and is connected to the ACPMS motor three-phase input wires, which creates a closed-circuit with the generator. The motors are controlled by an additional PWM signal supplied to the ESCs, which controls the opening and closing of the electric circuit regulating the voltage and motor current. Current and voltage should be measured for a motor at

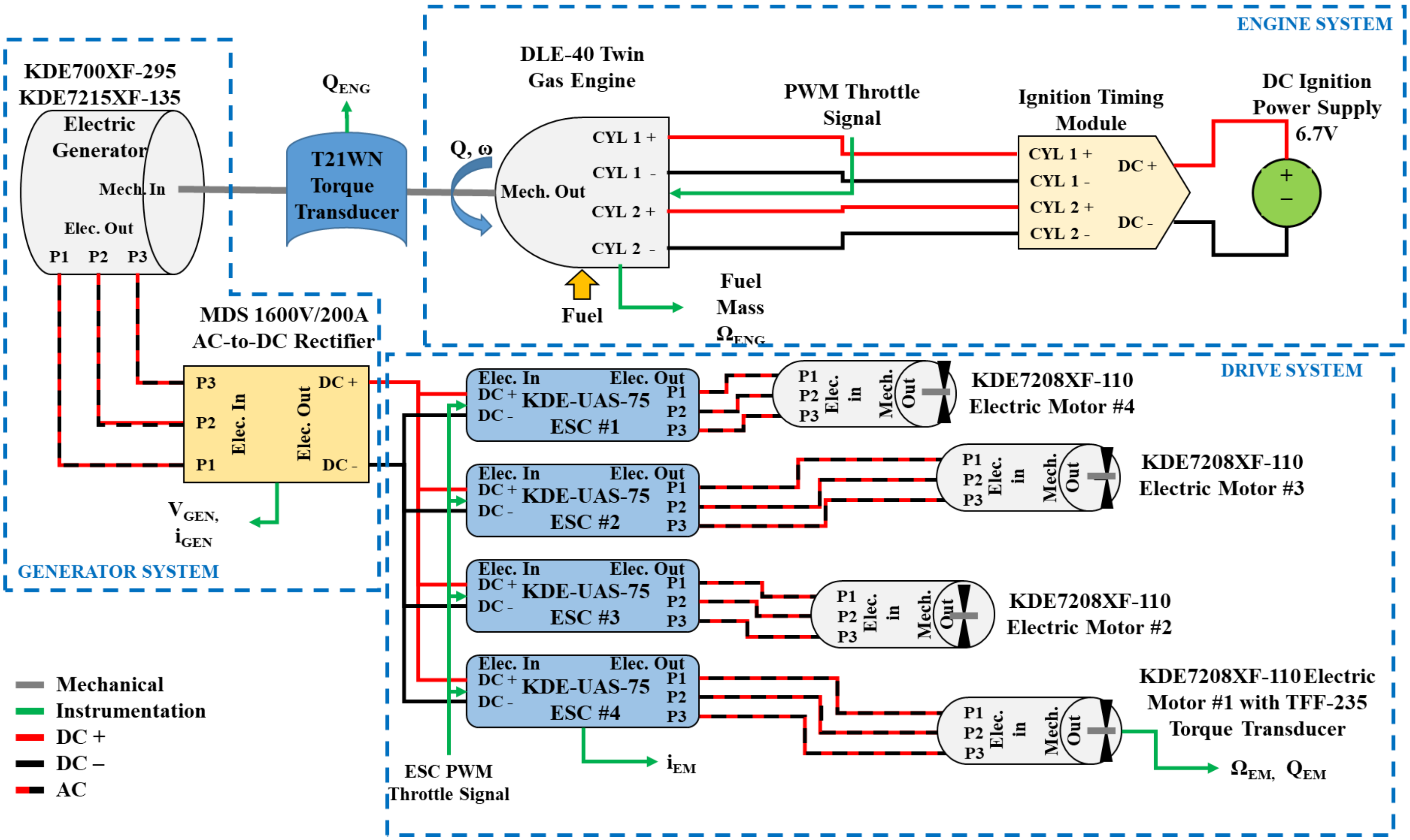

Figure 2.1. Schematic of the Distributed, Hybrid-Electric Powertrain.

the ESC input DC connection. The output torque and angular velocity of the same motor should also be collected.

2.3. Components of the Powertrain

The principal components of the powertrain are one reciprocating engine, one ACPMS generator, and four ACPMS motors. Two generators were ultimately used which could be swapped in and out effectively creating two powertrains. The principal components of the power electronics are one AC-to-DC rectifier and four ESCs. The principal instrumentation is fuel mass, engine torque, engine angular velocity, generator DC current, generator DC voltage, motor DC current, motor DC voltage, motor torque, and motor angular velocity.

2.4. Reciprocating Engine

The objective aircraft on paper envisioned a 3.5-kW Lycoming El-005 two-stroke, fuel-injected engine. However, that engine was outside the resources available for this research. A less expensive, two-stroke, carbureted engine was utilized as a starting point for this research. A DLE-40cc engine, shown in Figure 2.2, was used as the primary power source. The DLE-40 engine is a 40-cc, two-stroke twin-opposed-cylinder engine. The engine has a maximum continuous power of 3.58 kW. This engine uses a fuel-oil mixture and does not require a separate lubrication system. This enables lubrication regardless of the engine attitude. For this engine, the fuel consumption and speed limits are a function of the fuel-air settings of the carburetor. The carburetor was adjusted to provide a maximum engine speed of 9,000 RPM with minimal exhaust smoke at low RPM.

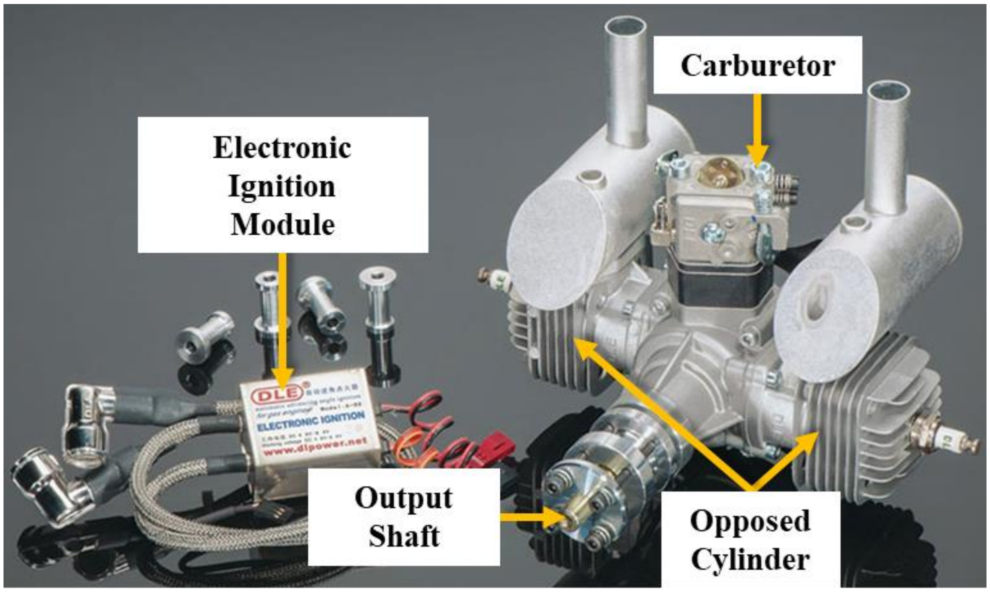

Figure 2.2. The off-the-shelf components of the DLE-40 two-stroke twin-, opposed-cylinder engine

Ignition is automatically timed by the electronic ignition module and preset at 44° before top dead center. The ignition module fires both cylinders at the same time. A flywheel is required to complete the compression stroke when there is no rotor load connected to the output shaft. Flywheels are used in piston engines to store enough energy to complete the compression stroke of the piston cycle and hence smooth the output torque. Normally the DLE-40cc engine utilizes the mass moment of inertia of the rotor as a flywheel to complete the compression stroke. However, in an electrical drive the rotor is mechanically isolated from the engine, and hence without a flywheel the engine could not operate. Therefore a 0.36-kg flywheel was installed on the engine output shaft to ensure engine operation.

Additionally, engines of this weight-class typically lack integrated starters and often rely on external starters attached directly to the engine output shaft. This technique cannot be used when the output shaft is connected to a generator. For this reason, a rope pull-start was incorporated, and the test frame was strengthened. Another option would be a flywheel with gearing to allow for an external starter attachment or utilizing the generator itself as a starter. While both options incur a weight penalty, the former is lighter whereas the latter would provide inflight restart (with additional power requirements). The latter option will be important for integration on a future aircraft but was not necessary for the research reported here.

2.5. ACPMS Generator

Two ACPMS generators were selected and used for the distributed, hybrid electric powertrain: KDE7215XF-135 and KDE700XF-295-G3.

The KDE7215XF-135 generator, shown in Figure 2.3, is an ACPMS motor configured as a torque absorber. This motor is made of trapezoidal-wound copper windings, silicon-steel stator laminations with Kevlar tie-wraps, a triple-bearing supported shaft, and Neodymium N45UH magnets. The generator is rated for a maximum continuous power of 4.4 kW at 85 A. It has a motor velocity constant (k_v) of 135 RPM/V and a motor torque constant (k_t) of 0.0707 N-m/A.

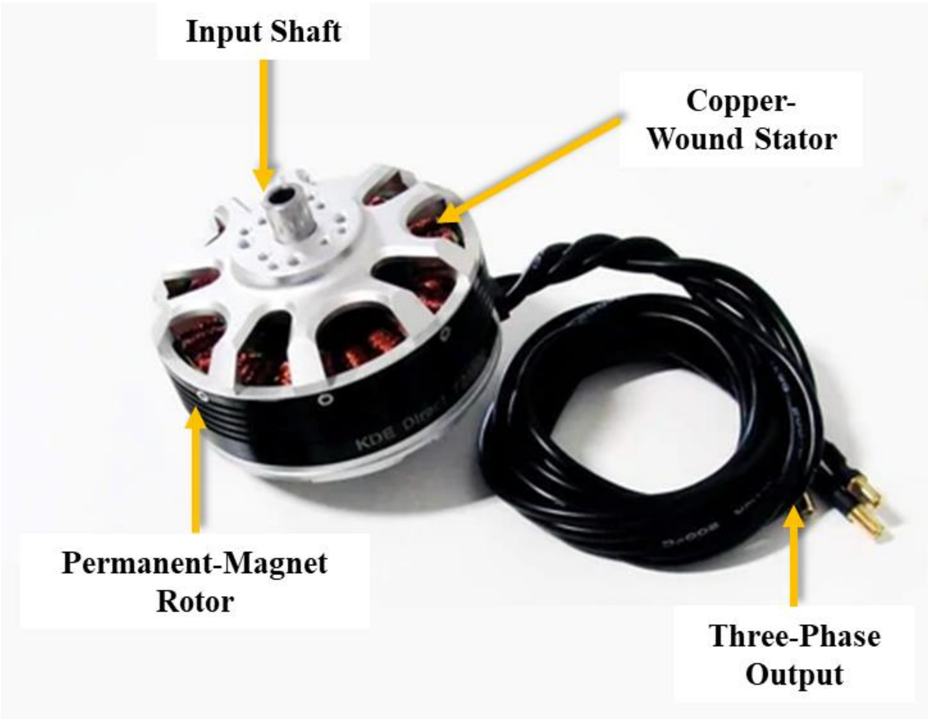

Figure 2.3. KDE7215XF-135 permanent-magnet generator

The KDE700XF-295-G3 generator, shown in Figure 2.4, maintains the same construction. However, it is larger and rated for a maximum continuous power of 7.195 kW at 139 A. It has a velocity constant of 295 RPM/V and a torque constant of 0.0324 N-m/A.

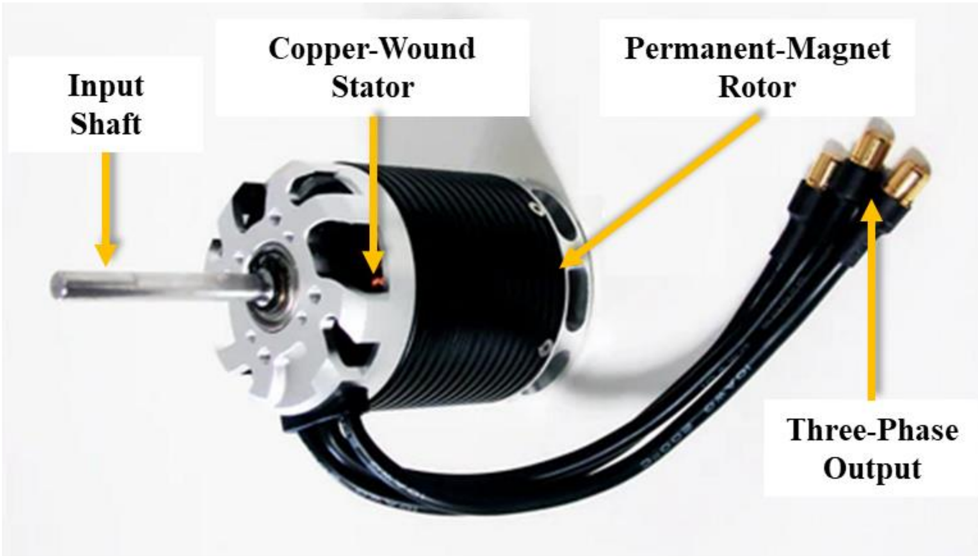

Figure 2.4. KDE700XF-295-G3 permanent-magnet generator

2.6. ACPMS Motor

Four KDE7208XF-110 ACPMS motors were selected and used for the distributed, hybrid electric powertrain.

The KDE7208XF-110 motor, shown in Figure 2.5, is an ACPMS motor. It has the same construction as the generators. The motor is rated for a maximum continuous power of 2.225 kW at 50 A. It has a velocity constant of 110 RPM/V and a torque constant of 0.0868 N-m/A.

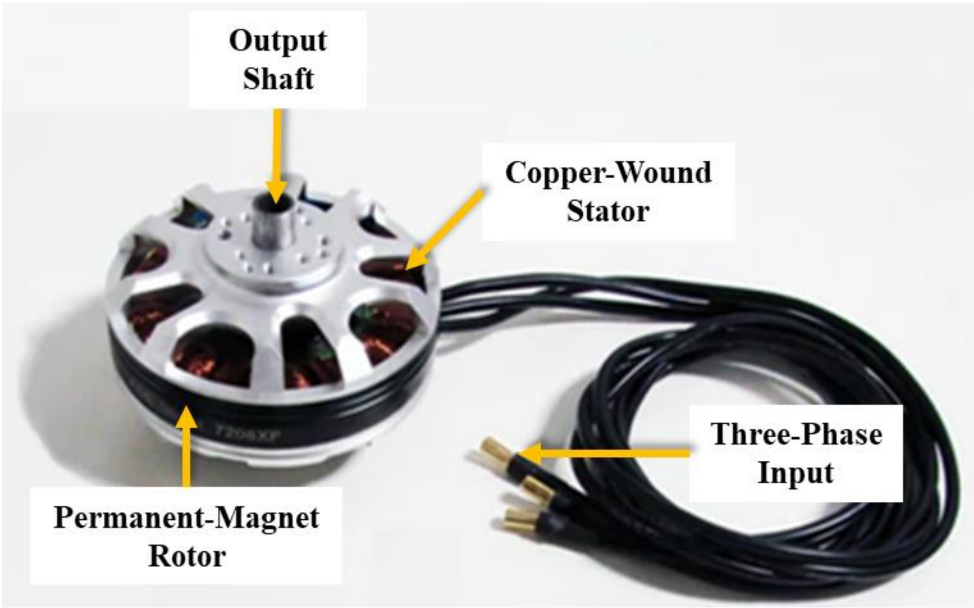

Figure 2.5. KDE7208XF-110 permanent-magnet motor

2.7. Power Electronics

The power electronics consisted of on MDS-200A diode bridge inverter and four KDE-UAS75HVC electronic speed controllers.

An MDS-200A, 1600V three-phase bridge rectifier, shown in Figure 2.6, was selected, and used to convert a 3-phase AC input into a DC output. The bridge rectifier is constructed of six diodes and is rated for 200 A DC output with a maximum voltage of 1600 VRMS. This rectifier was selected for its high thermal conductivity.

The KDE-UAS75HVC ESC, shown in Figure 2.7, is a waterproof DC-to-AC inverter designed to control the KDE7208XF-110 motor. The ESC is rated for a maximum continuous power of 3.330 kW at 75 A. While the ESC is programmable through USB firmware, there was no need for it for this test program.

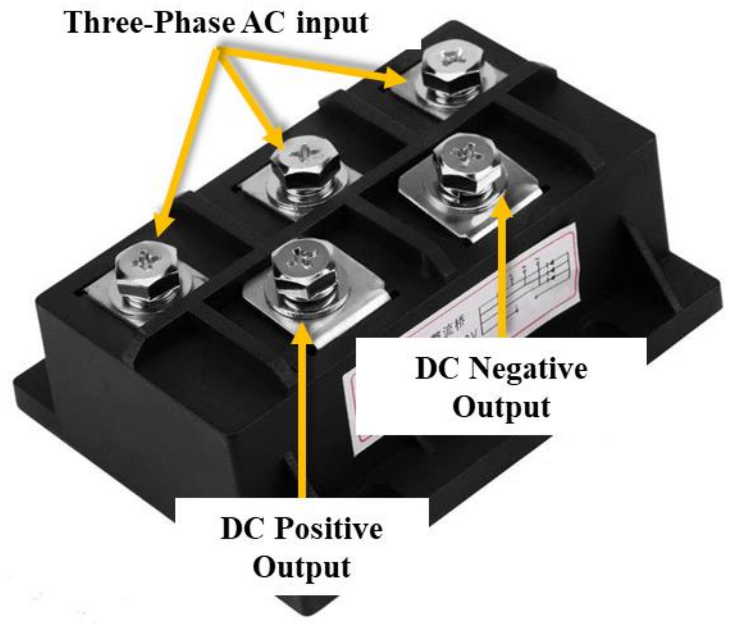

Figure 2.6. MDS-200A, 1600V three-phase AC-to-DC bridge rectifier

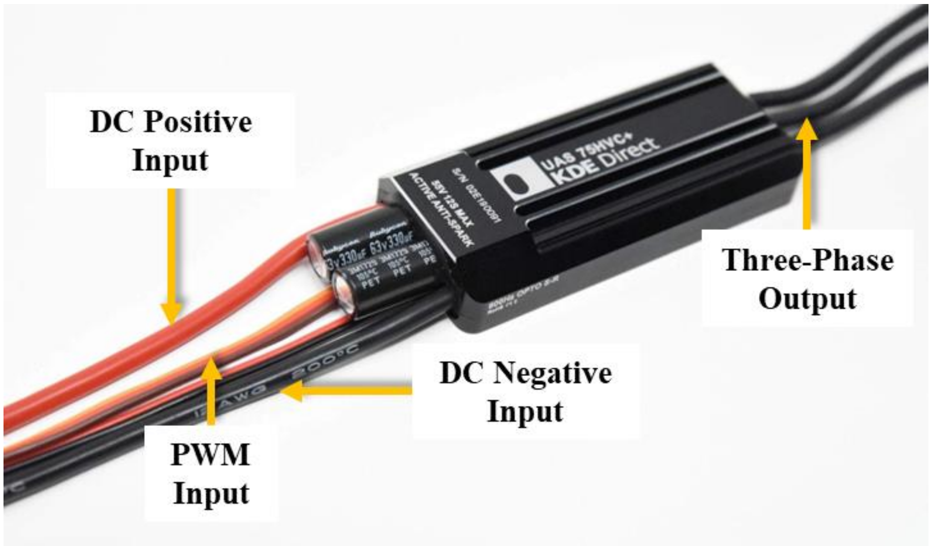

Figure 2.7. KDE-UAS75HVC Electronic Speed Controller

2.8. Instrumentation

The principal instrumentation requirements are engine and motor angular velocity, engine and motor torque, generator and motor DC current, generator and motor DC voltage, and fuel mass. As such the instrumentation consisted of two Hall-effect sensors, two torque transducers, two current sensors, two voltmeters, and one weight scale.

Engine angular velocity was measured using a 1/rev Hall-effect sensor on the engine output shaft, as shown in Figure 2.8. Engine angular velocity was measured in RPM. The sensor was powered from the ignition power supply. Engine torque was measured with an HBM T21WN torque transducer, shown in Figure 2.9, powered with a 10V DC power supply. Because the engine is rigidly connected to the generator with the torque transducer in between, the engine output torque and RPM is identical to the generator input torque and RPM. The fuel tank was mounted to an Adam CBK-35a weighing scale, shown in Figure 2.10, powered by a 120V, 15A electric outlet. Fuel consumption was measured by the difference in tank weight. Engine power was controlled by regulating the amount of fuel and air entering the engine. The carburetor regulates fuel flow based on the throttle valve position controlled using a servo-actuator. The servo-actuator was controlled remotely with a manual digital controller powered from the ignition power supply.

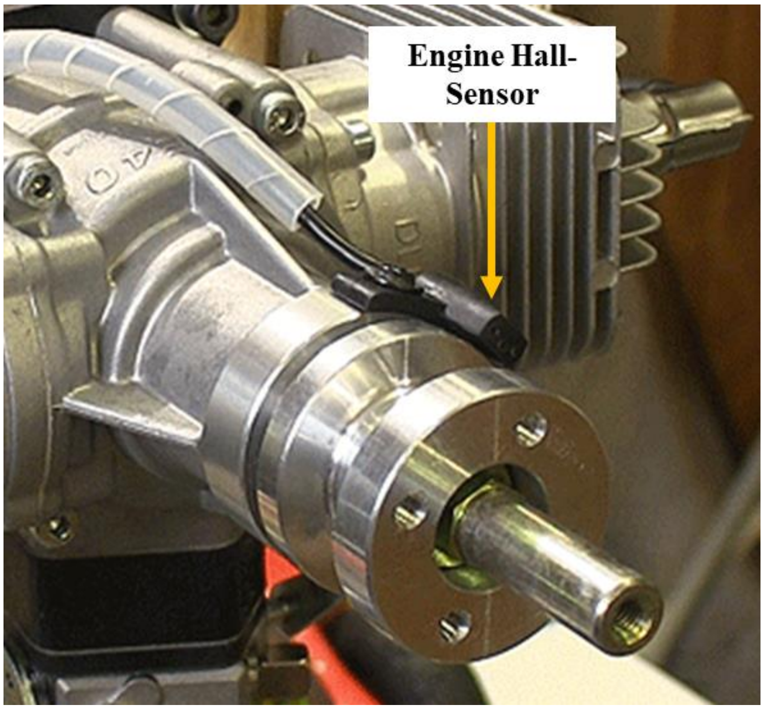

Figure 2.8. DLE-40 integral hall sensor

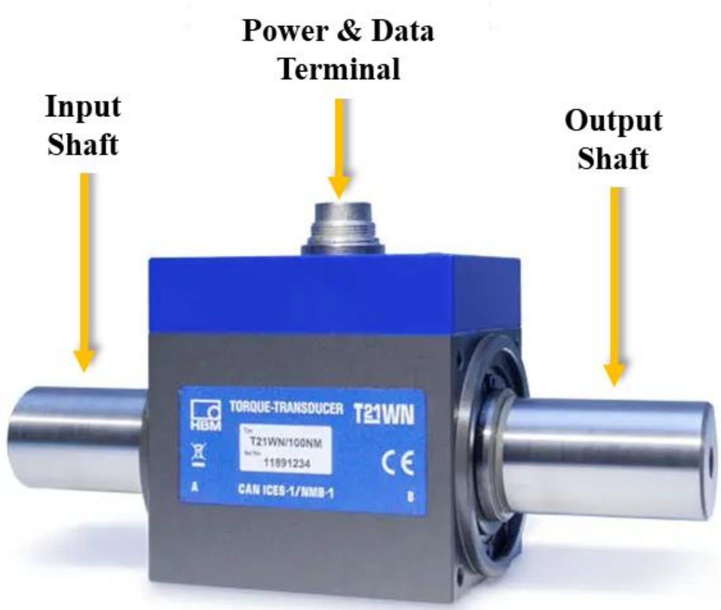

Figure 2.9. T21WN 10 Nm torque transducer

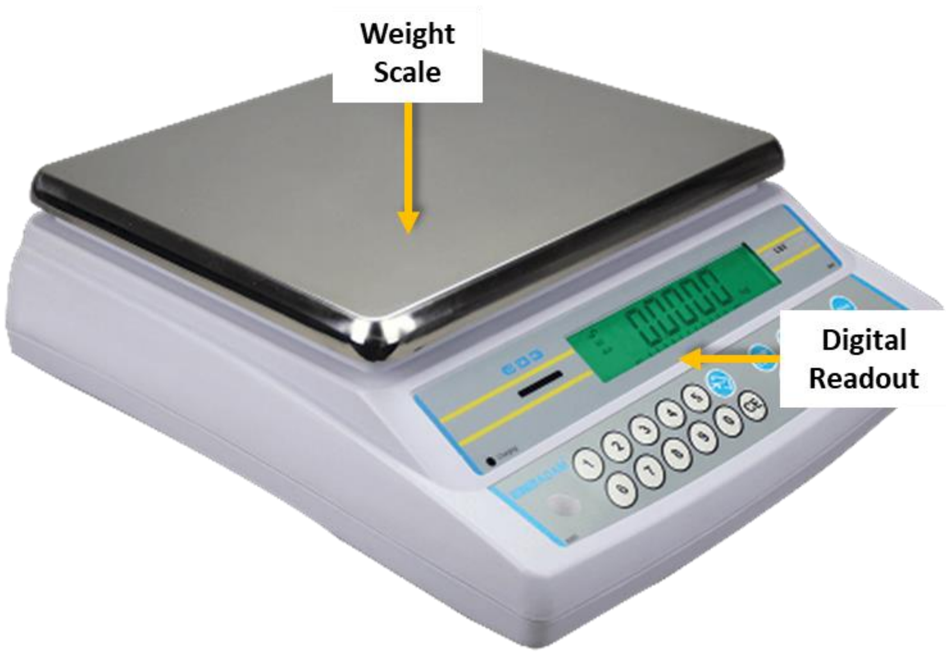

Figure 2.10. Adam CBK-35a weighing scale

The generator output voltage was measured at the + DC pin of the rectifier using the voltmeter function of the data acquisition (DAQ) unit. An 11:1 voltage divider circuit was fabricated to reduce voltage to within ±5V. The generator output current was measured using either an Allegro ACS-770LCB-100U-PFF-T (4.4kW generator) or an Allegro ACS-770LCB-200U-

PFF-T (7.2 kW generator) current sensor, as shown in Figure 2.11. The current sensors were mounted at the + DC pin of the rectifier. A second order RC filter was used to convert the digital output of the sensor to an analog output prior to the DAQ unit. The current sensors were powered using a 5V DC power supply.

The electric motor input voltage was measured at the + DC input pin of the motor ESC using the voltmeter function of the DAQ unit with an 11:1 voltage divider circuit. The input current was measured using an Allegro ACS-770LCB-100U-PFF-T current sensor. The current sensor was mounted at the + DC input pin of the motor ESC in series with the ESC. A second order RC filter was used to convert the digital output of the sensor to an analog output prior to the DAQ unit. The current sensor was powered using a 5V DC power supply.

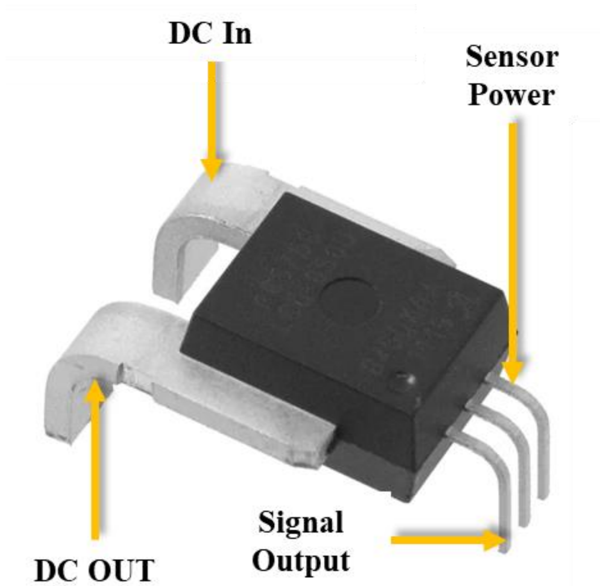

Figure 2.11. Allegro ACS-770LCB-100/200U-PFF-T current sensor

Rotor torque was measured using a Futek TFF325 reaction torque transducer, as shown in Figure 2.12. The Futek torque transducer was mounted between the motor body and the test cell. The torque transducer was connected to an IAA100 analog strain amplifier which was powered with a 10V DC power supply. Rotor angular velocity was measured using an additional DLE-40 1/rev Hall-effect sensor installed on the body of the electric motor. The rotor Hall-effect sensor was powered with the engine ignition power supply. The rotor speed was controlled remotely with a battery-powered, manual PWM motor controller.

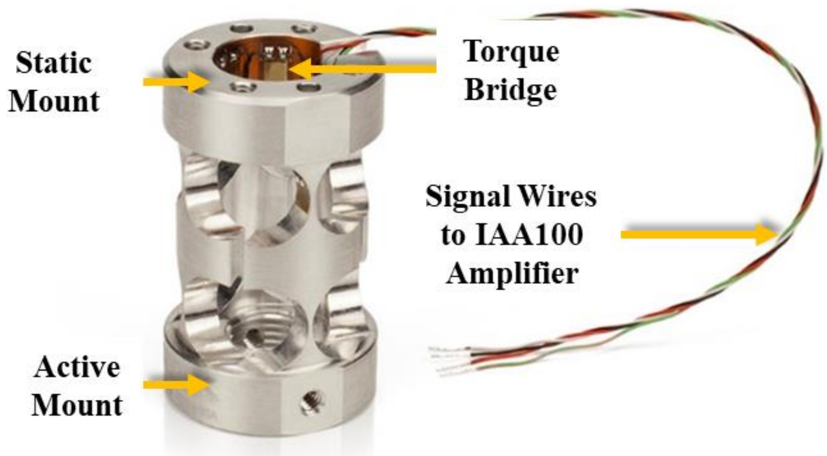

Figure 2.12. Futek TFF325 reaction torque transducer

A National Instruments USB-6002 Multifunction I/O Device, shown in Figure 2.13, and a National Instruments PXI-8106 controller with PXI-6133S Multifunction DAQ cards, shown in Figure 2.14, were used with LabVIEW 2017 as a data acquisition unit. The USB-6002 is an eight-channel, analog, 0-10V, voltmeter capable of data logging. The PXI-8106 with two PXI-6133S Multifunction DAQ cards is a sixteen-channel, analog, 0-10V, voltmeter capable of data logging.

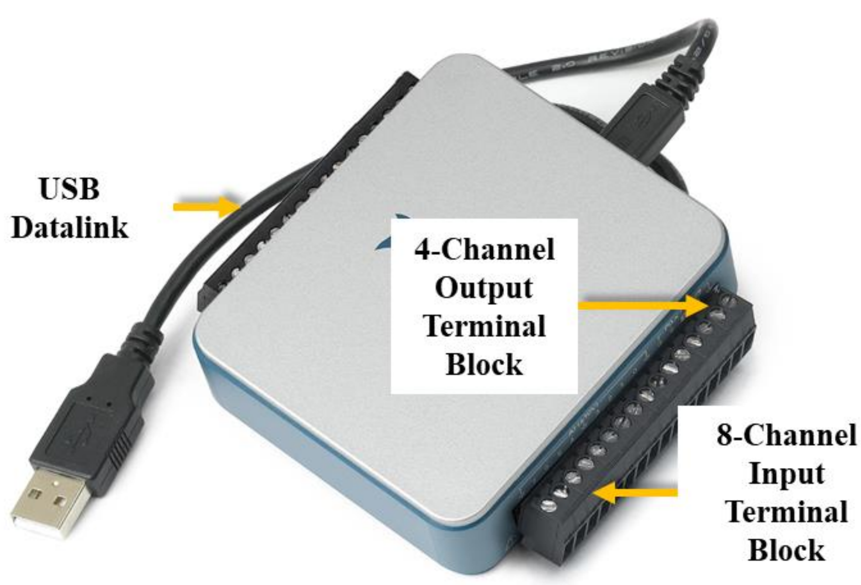

Figure 2.13. National Instruments USB-6002 Multifunction I/O Device

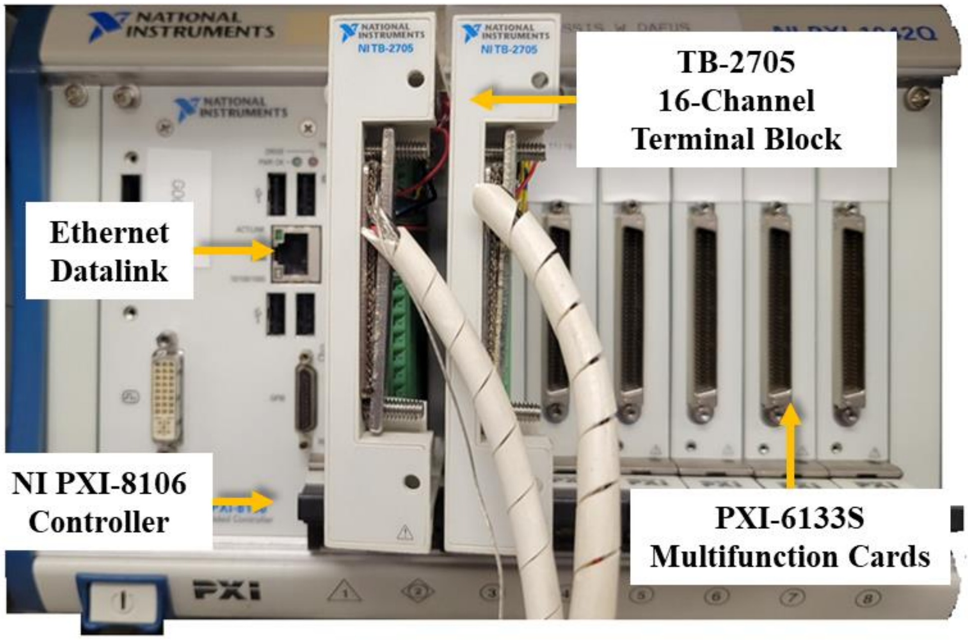

Figure 2.14. National Instruments PXI-8106 controller with PXI-6133S Multifunction DAQ cards

2.9. Integrated Powertrain Test Cell

CAD models of the components were developed, and a virtual testbed was created first. This virtual model was used to design the testbed as well as ensure proper assembly and integration. This model is shown in Figure 2.15. The assembled testbed is shown in Figure 2.16 and Figure 2.17. The test frame was constructed from 6115 aluminum slotted frames. The mechanical couplings from the engine to the torque transducer and from the torque transducer to the generator were clamping aluminum hubs with polyurethane vibration-damping flexible spiders. Soldered bullet connectors were used to couple the current transducer, motors, generator, and ESC wires. All wiring utilized the recommended AWG sizes or larger.

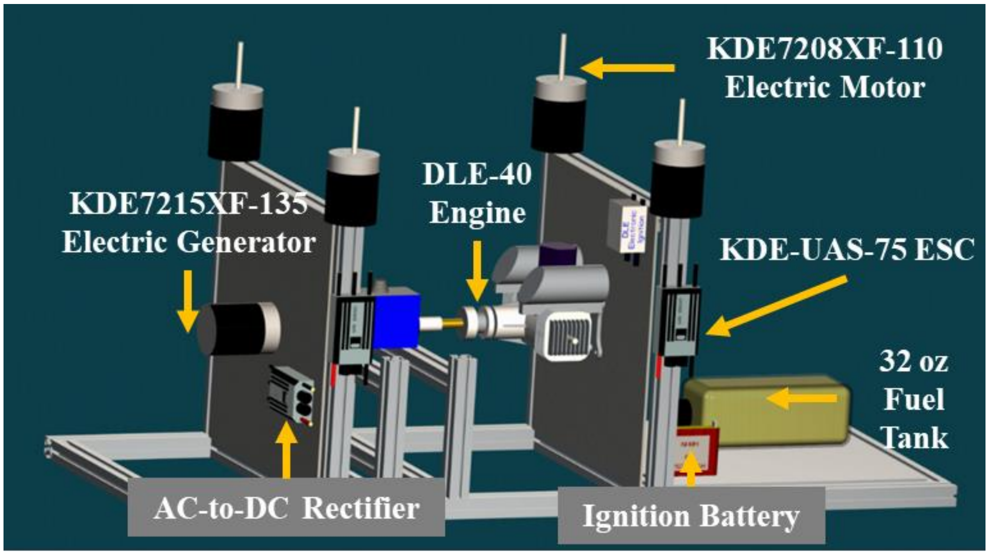

Figure 2.15. CAD model of the components and experimental test bed

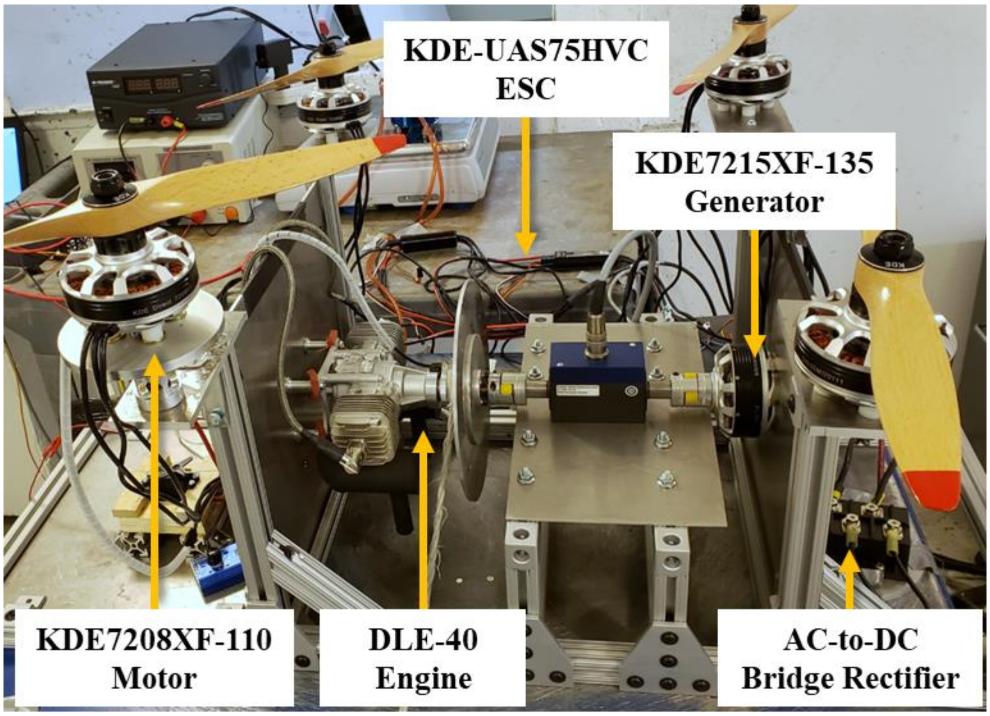

Figure 2.16. The integrated powertrain test cell

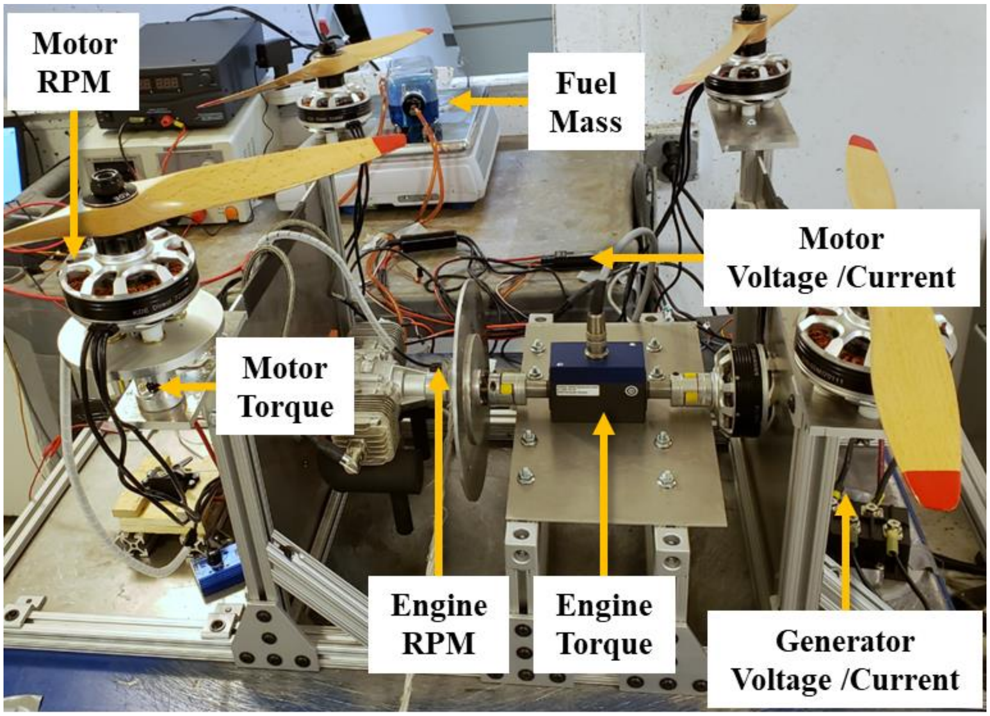

Figure 2.17. Instrumentation for the integrated powertrain

2.10. Chapter Summary and Conclusions

A variable-voltage hybrid-electric powertrain was designed and fabricated based on a 50-lb, hybrid-electric QBiT objective aircraft. The powertrain was constructed with commercial off-the-shelf components. In addition to the primary components of the powertrain (engine, generator, motors, power electronics), the powertrain was instrumented to collect component currents, voltage, torques, and angular velocities. It was found that small engines (below 5kW) typically lack integrated starters and must rely on external starter drives that attach to a propeller. However, in distributed electric propulsion, the propeller is mechanically isolated from the engine. Typically, these engines also lack an integrated flywheel to store energy for the compression stroke and utilize the propeller instead to provide this function. The generator typically lacks the mass moment of inertia to complete the compression stroke. Thus, proper starting and operating mechanisms must be designed for in-flight operation. In this study, a simple pull-start mechanism was built.

Chapter 3: Experimental Characterization of the Distributed, Hybrid-Electric Powertrain

This chapter describes the experimental characterization of the distributed, hybrid-electric (DHE) powertrain. Three types of tests of progressively increasing complexity: 1) isolated engine-generator tests, 2) engine-generator tests with one electric drive, and 3) engine-generator tests with four electric drives including the test setup, procedure and results are covered.

3.1. Engine-Generator Tests

The goals of the isolated engine-generator tests were to measure: 1) the fuel efficiency of the engine at various engine torques and speeds, 2) the electrical efficiency of the generator at various output currents and voltages, and 3) the fuel efficiency of the combined engine-generator system at various output currents and voltages. The fuel efficiency of the engine is measured as specific fuel consumption (SFC) in kg/kW-hr.

3.1.1. Test Setup

The schematic and corresponding testbed setup are shown in Figures 3.1 and 3.2, respectively. The engine shaft is connected to a shaft-to-shaft torque transducer, which is then connected to the generator shaft. The three-phase electrical output of the generator is connected to the AC-to-DC rectifier. Connected to the rectifier is a constant current load bank, which is used to draw a range of DC currents. An EagleEye LB-48-200-CC, 48V/200A, constant current load bank was used. The test matrix consists of a set of currents drawn over a range of engine speeds.

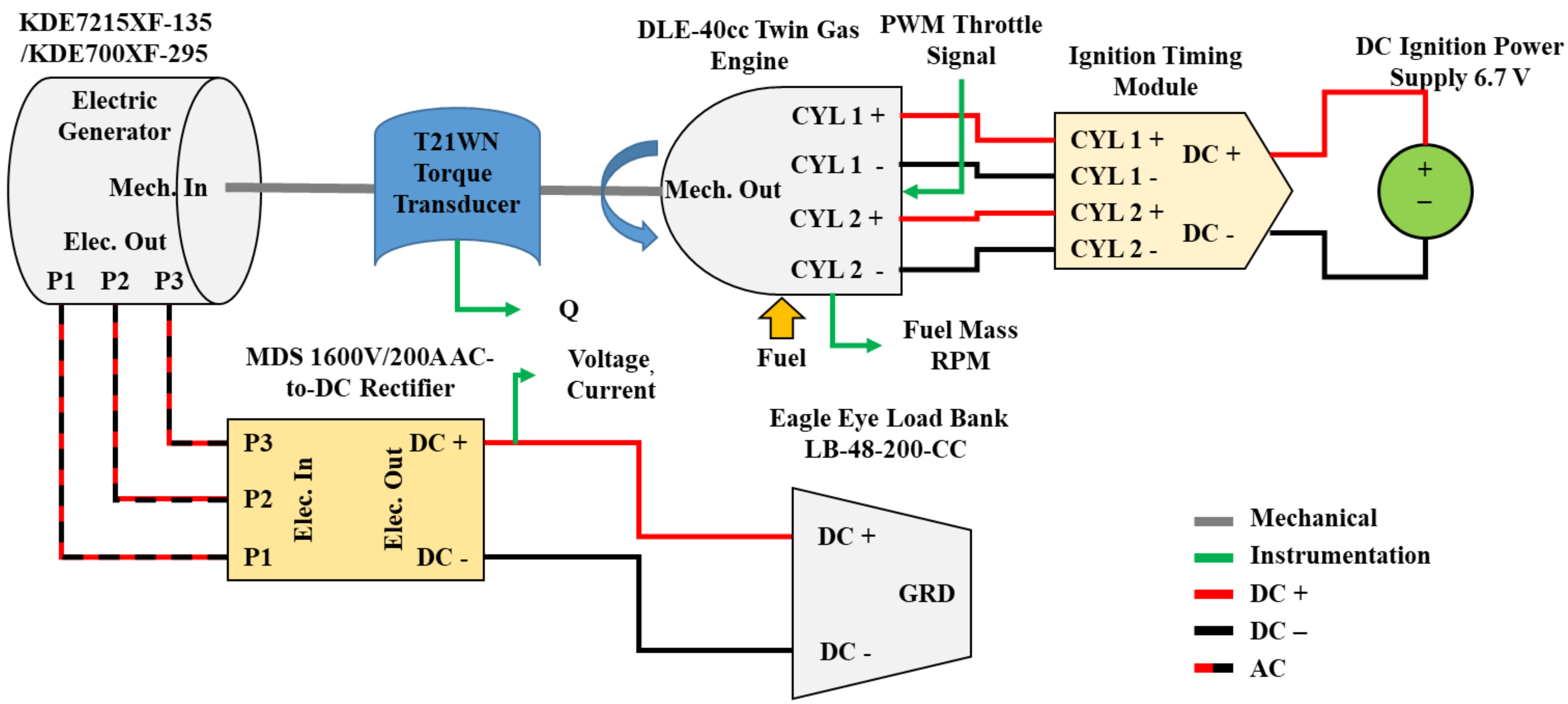

Figure 3.1. Schematic of the powertrain with DC load bank

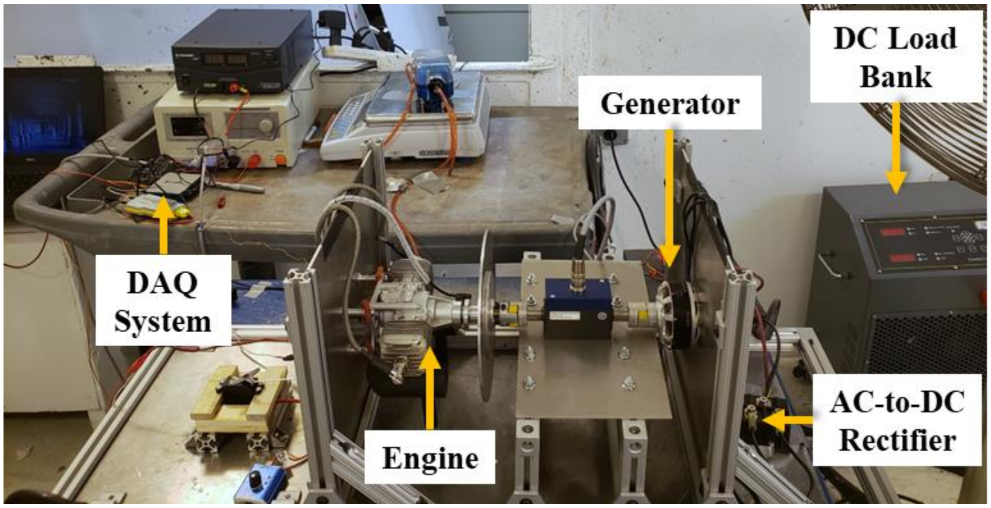

Figure 3.2. Instrumented powertrain with DC load bank

3.1.2. Test Procedure

The tests consisted of several engine speed sweeps. For each sweep, the engine speed was increased to high idle, then the specified current was drawn by activating the load bank. The engine speed was then adjusted to the first engine RPM test point and held steady. After 1 minute, data acquisition was initiated. At the end of the data acquisition period, (~3 minutes), engine speed was increased to the next test point, and the data acquisition process repeated. Current draw was held constant throughout at a specified value. During each data acquisition period, fuel consumption was measured. Due to the stiffness of the fuel line, vibrations were transmitted from the engine to the fuel tank, resulting in oscillating fuel readings. Fuel consumption was measured as the average of the peak-to-peak amplitudes. At the end of each RPM sweep, the engine was shut down and refueled. Once the engine cooled to room temperature the test sequence was repeated for the next specified current.

3.1.3. Results from the 4.4-kW KDE7215XF-135Generator

The combined engine-generator was tested at 66 conditions. Load current was varied from 10 to 60 A in 10A increments. Engine RPM was varied from 2,500 to 7,500 RPM in 500 RPM increments. At each point a set of three measurements are taken for a period of at least 3 minutes or until 100g of fuel was consumed. From the data set, the engine and generator can be examined separately as well as a combined system.

The fuel efficiency of the engine alone is shown in Figure 3.3, with constant power lines marked. The engine SFC contours are plotted as a function of engine torque and RPM. It is clear that at a given power the engine is more efficient at higher torque and lower RPM. Figure 3.4 plots the same fuel efficiency but now as a function of power, with constant torque and RPM lines marked. To reduce power, it is generally more efficient to lower the RPM and raise the torque. For example, suppose the hover point for the engine is 3.4 kW at 7,500 RPM (Point 1). Now let the cruise power be 1.5 kW. Reduction in power while maintaining RPM results in increasing SFC (Point 1 to Point 2). Reduction in power by decreasing RPM and increasing torque results in a reduction of SFC (Point 1 to Point 3). Decreasing both RPM and torque is a viable option. Thus, decreasing RPM is the key requirement. The torque can be increased or decreased, although, increasing torque provides the maximum benefit.

The electrical efficiencies of the generator (and rectifier) are shown in Figures 3.5 and 3.6, with constant power lines marked. Figure 3.5 plots the electrical efficiency contours as a function of input torque and RPM. The generator converts the torque and RPM into current and voltage. So, the efficiency can also be plotted as a function of these quantities, as in Figure 3.6. Comparing Figure 3.5 and Figure 3.6 makes it clear that voltage is analogous to engine RPM and the current analogous to torque. It is also clear that at a given power, the generator efficiency peaks at moderate voltage and current. Figure 3.7 plots the efficiency as a function of input power, with constant torque and RPM lines marked. Similarly, Figure 3.8 plots the efficiency as a function of output power with constant current and voltage lines marked. Both are useful, but the latter is more

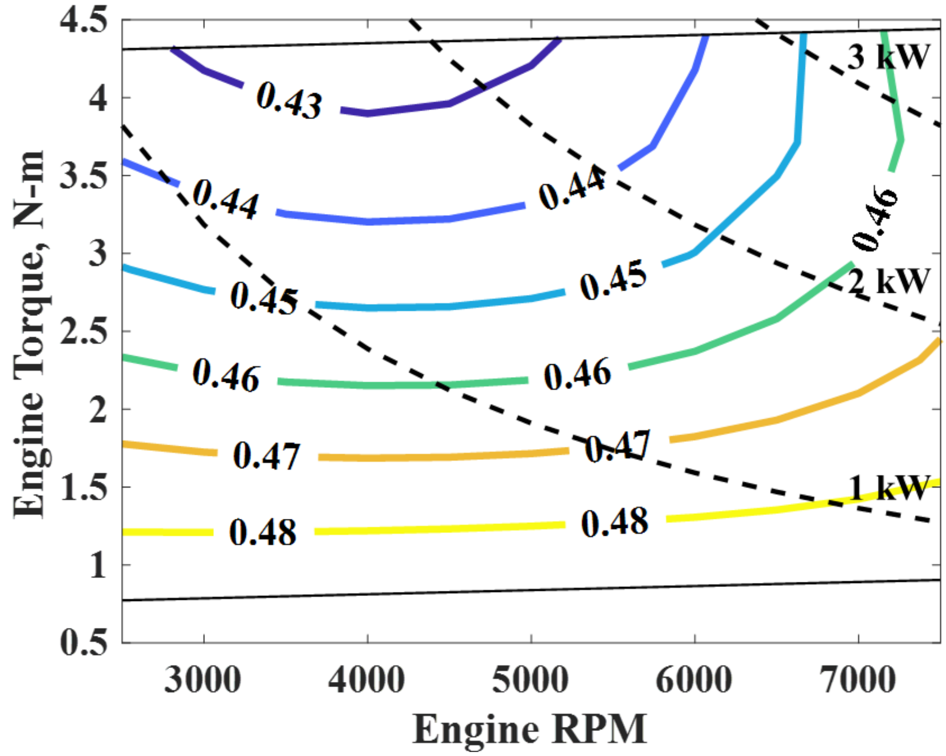

Figure 3.3. Engine torque versus RPM with specific fuel consumption contours (kg/kW-hr) and constant power curves

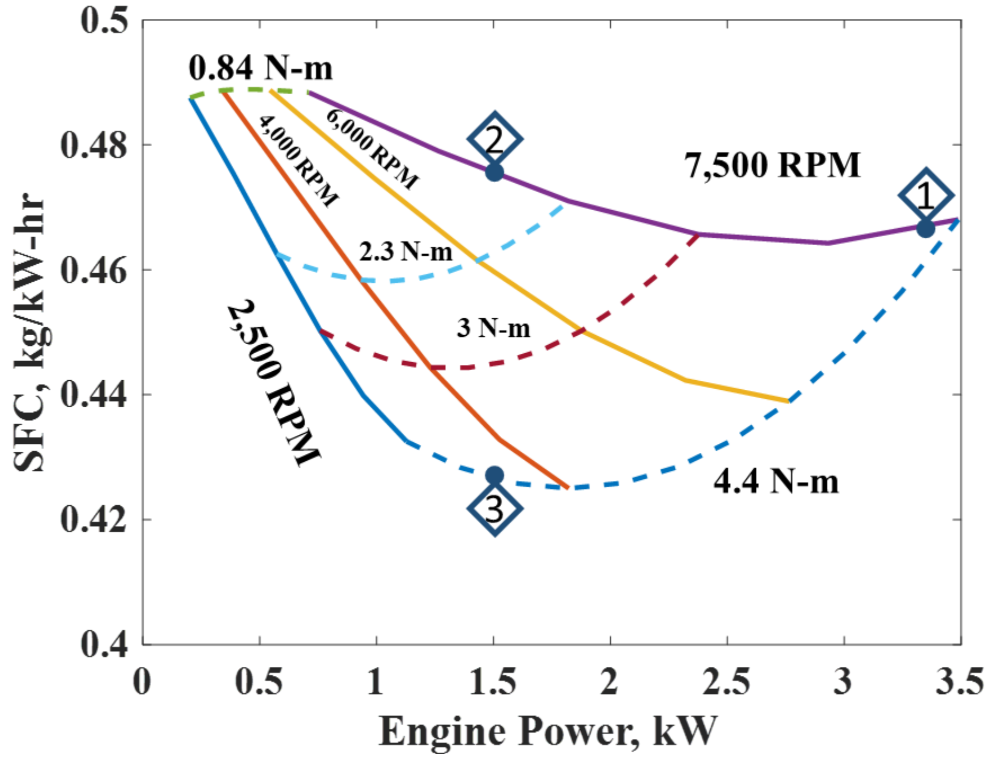

Figure 3.4. Engine specific fuel consumption versus power with constant RPM and torque contours

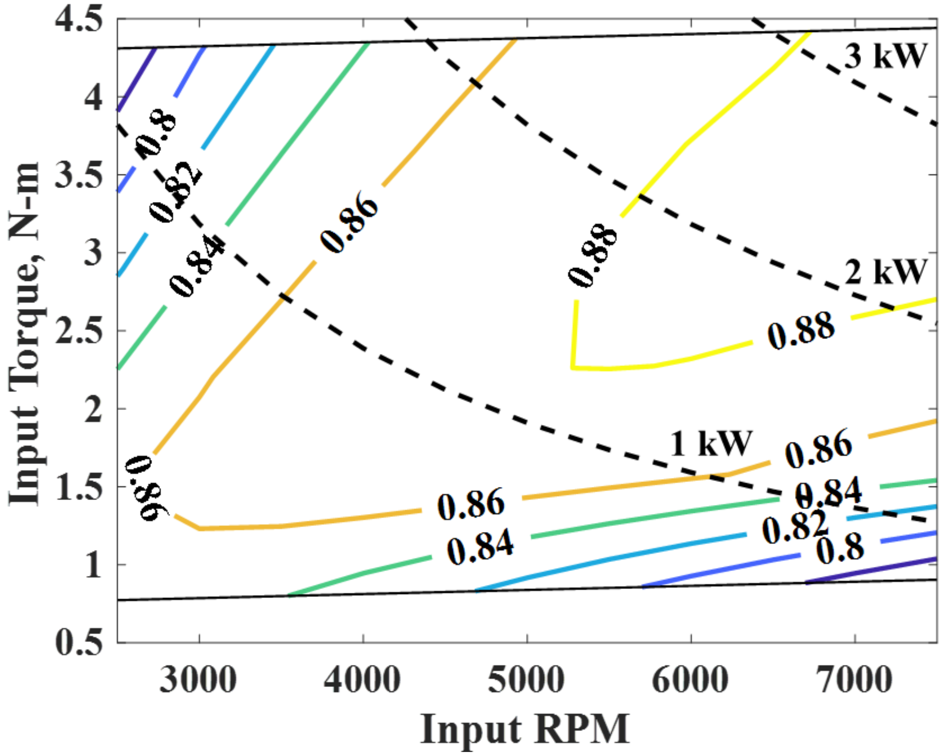

Figure 3.5. Input torque versus RPM with generator efficiency contours; 4.4 kW generator

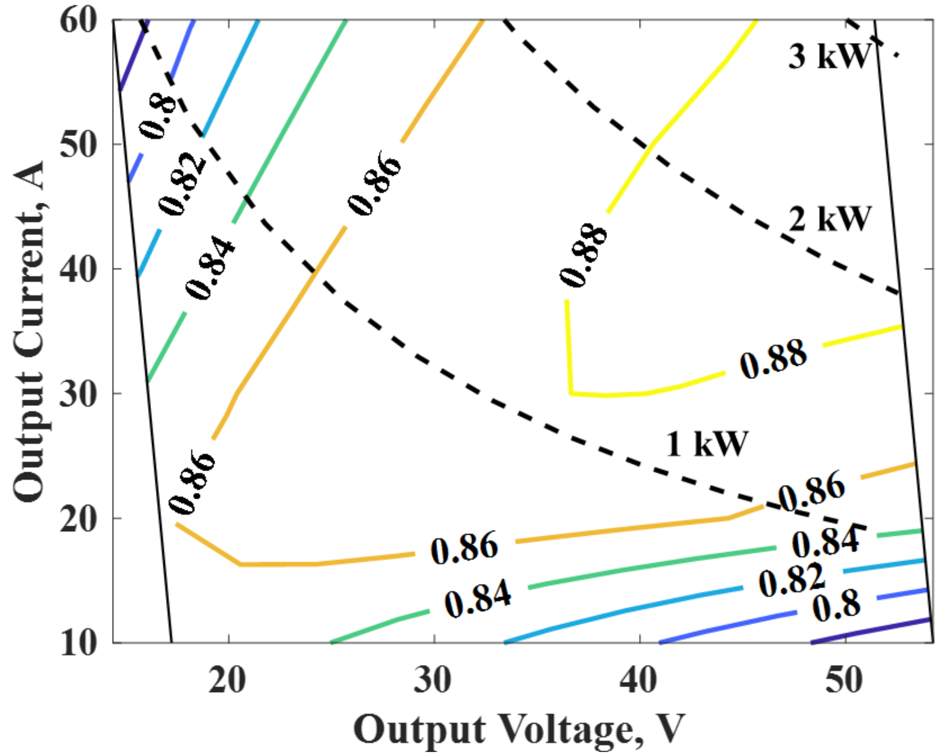

Figure 3.6. Output current versus voltage with generator efficiency contours; 4.4 kW generator

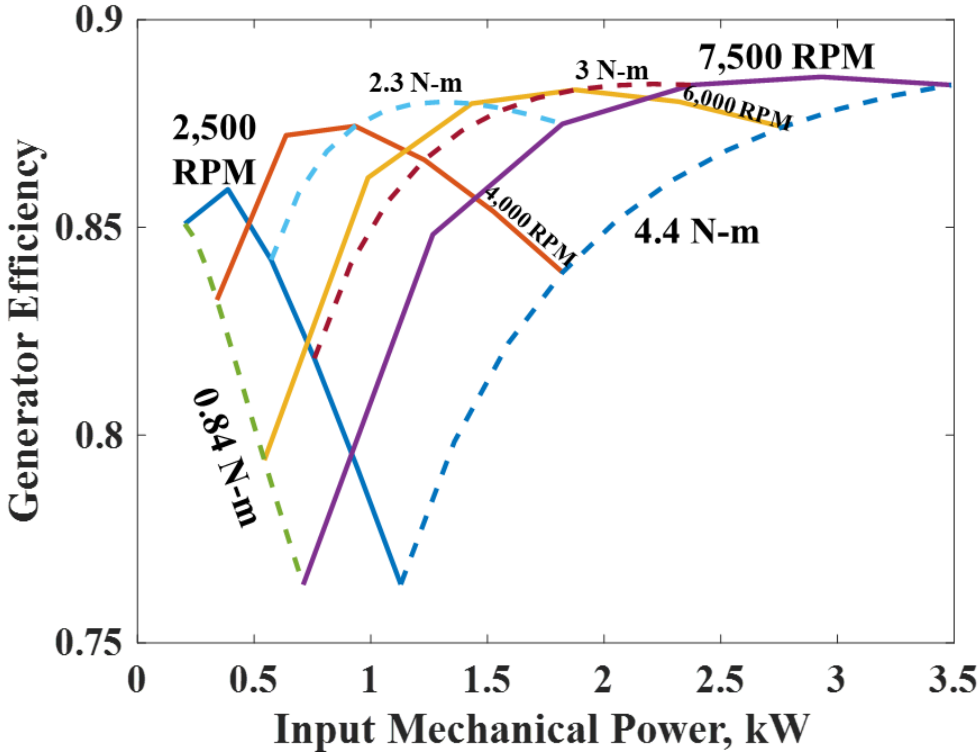

Figure 3.7. Generator efficiency versus input mechanical power with input RPM and torque contours; 4.4 kW generator

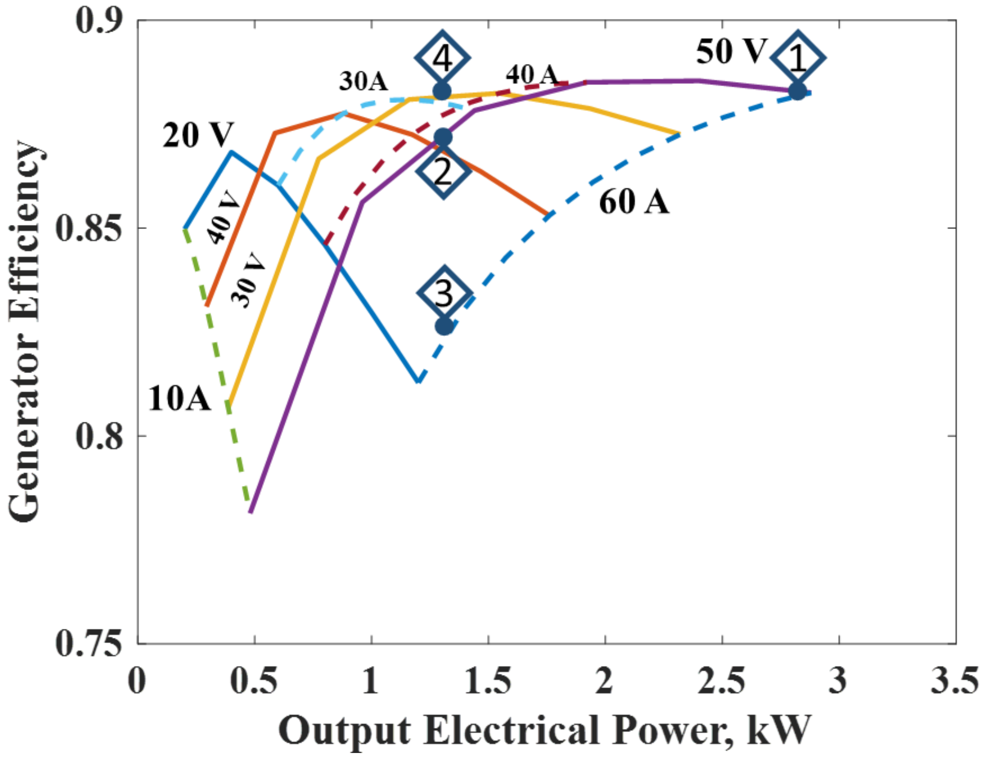

Figure 3.8. Generator efficiency versus output electrical power with output voltage and current contours; 4.4 kW generator

appropriate for interpreting the behavior of the generator. To reduce power, it is best to lower both the voltage and current. For example, suppose the hover point for the generator is 2.9 kW at 50 V (Point 1). Reduction to a cruise power of say, 1.3 kW, while maintaining either constant voltage (Point 1 to Point 2) or constant current (Point 1 to Point 3), results in decreased efficiency. However, if both voltage and current are reduced (Point 1 to Point 4), efficiency can remain near the maximum value. Thus, decreasing voltage is the key requirement. The current can be increased or decreased, although increasing current provides the maximum benefit. Because voltage is analogous to engine RPM, decreasing voltage effectively means decreasing engine RPM is essential.

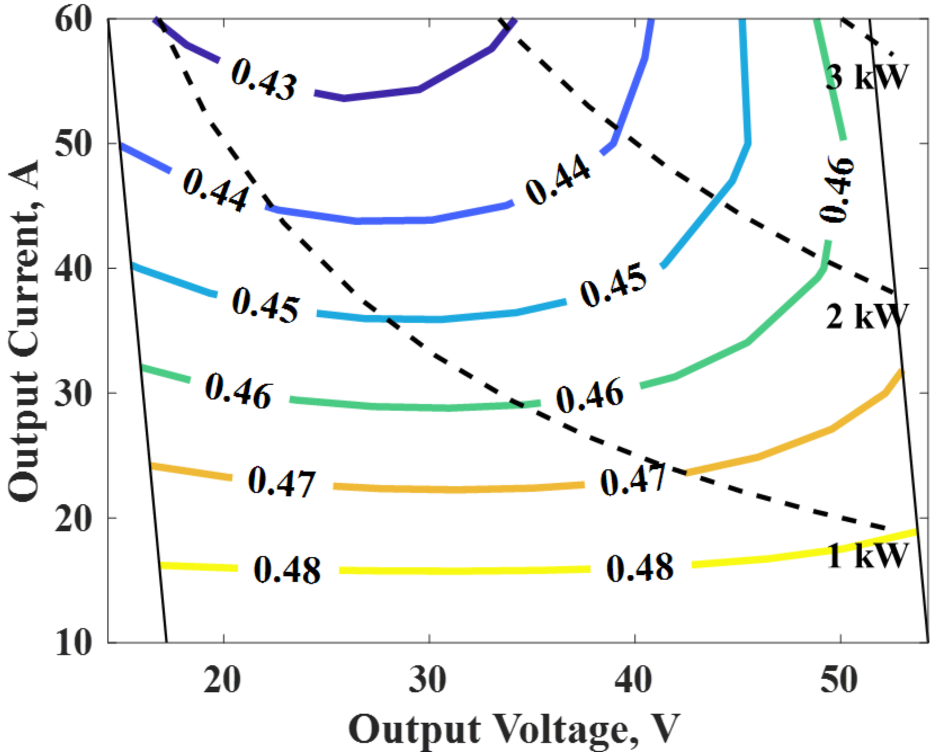

Figure 3.9. Engine-generator output current versus voltage with specific fuel consumption contours (kg/kW-hr) and constant power curves

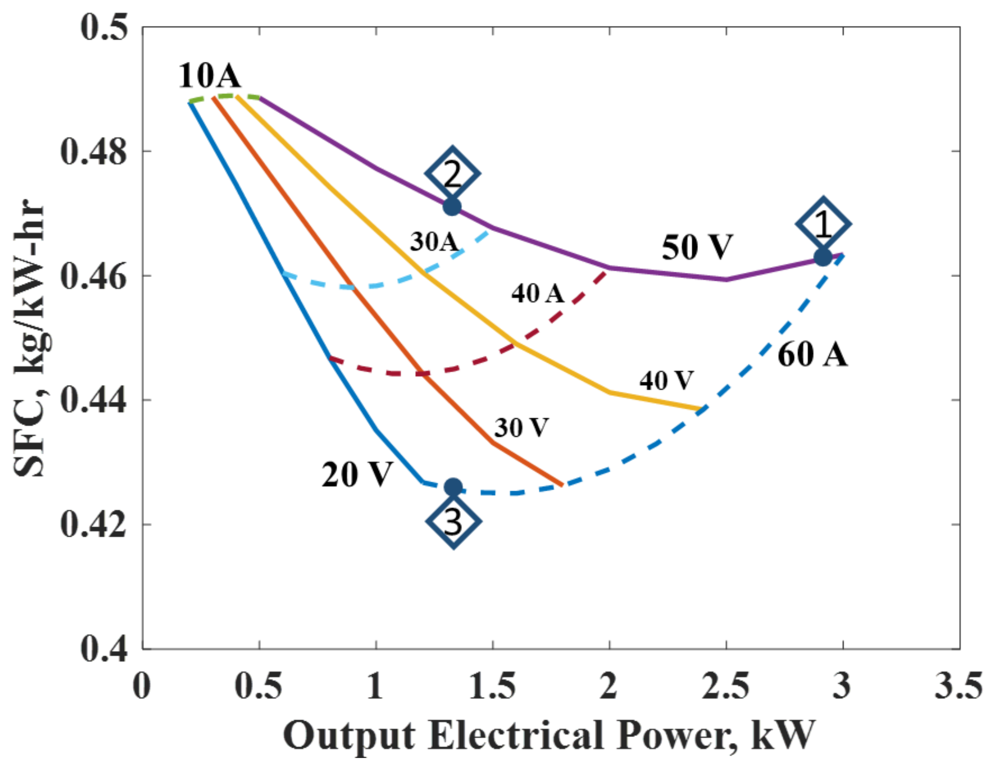

Figure 3.10. Engine-generator specific fuel consumption (kg/kW-hr) versus output electrical power with output voltage and current contours; 4.4 kW generator

3.1.4. Results from the 7.2-kW KDE700XF-295-G3 Generator

For the 7.2 kW generator, the combined engine-generator was tested at 70 points. Load current was varied from 20 to 140 A in 20A increments. Engine RPM was varied from 4,000 to 9,000 RPM in 500 RPM increments. At each point, a set of three measurements were taken for a period of at least 3 minutes or until 100g of fuel was consumed. From the data set, the engine and generator can be examined separately as well as a combined system.

The fuel efficiency of the engine alone is shown in Figure 3.9, with constant power lines marked. Figure 3.12 plots engine SFC contours as a function of engine torque and RPM. In comparing Figure 3.12 with the previous characterization shown in Figure 3.4, it is clear that changing the generator does not alter the fuel efficiency of the engine, but only extends the RPM range.

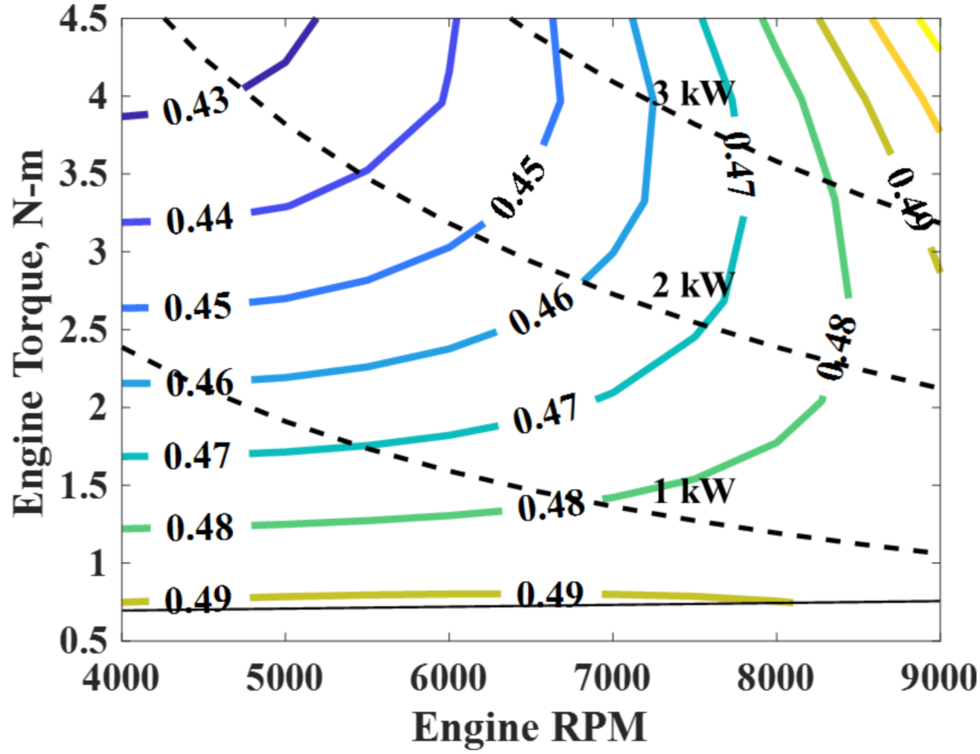

Figure 3.11. Engine torque versus RPM with specific fuel consumption contours (kg/kW-hr) and constant power curves

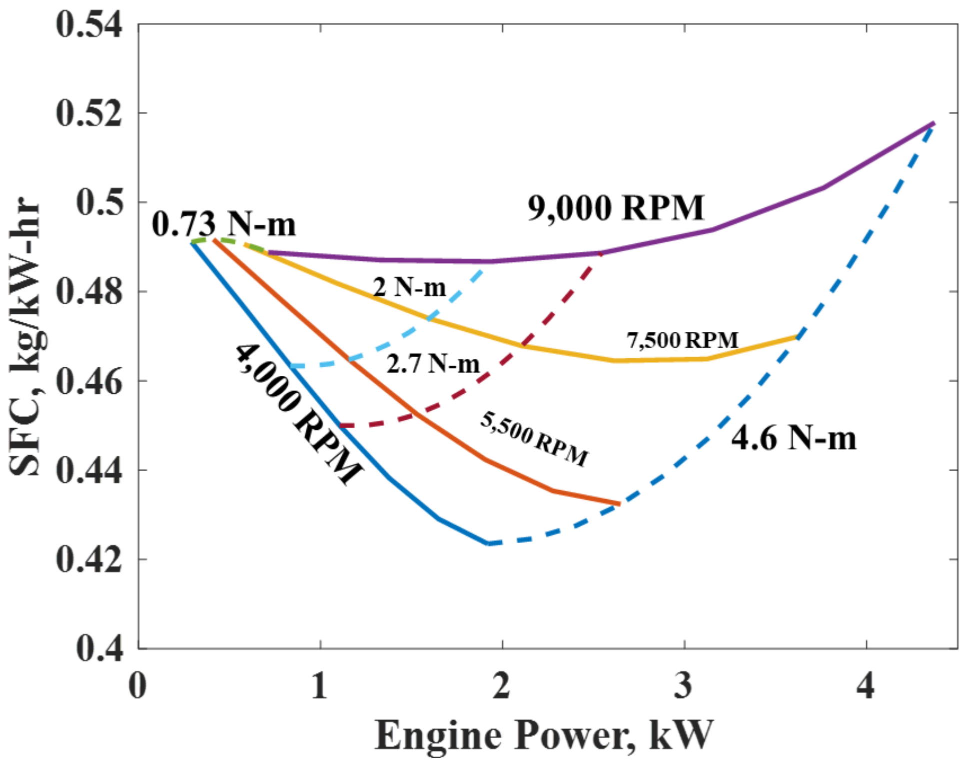

Figure 3.12. Engine specific fuel consumption versus power with constant RPM and torque contours

The electrical efficiencies of the larger generator (and rectifier) are shown in Figures 3.13 and 3.14, with constant power lines marked. Figure 3.13 plots the electrical efficiency contours as a function of input torque and RPM. The generator converts the torque and RPM into current and voltage. So, the efficiency can also be plotted as a function of these quantities as in Figure 3.14. As with the smaller generator, in comparing Figures 3.13 and Figure 3.14, it is clear that voltage is analogous to engine RPM and current analogous to torque. Similarly, at a given power the generator efficiency peaks at moderate voltage and current. Figure 3.15 plots the efficiency as a function of input power, with constant torque and RPM lines marked. Figure 3.16 plots the efficiency as a function of output power with constant current and voltage lines marked. The same conclusions carry over from the smaller generator.

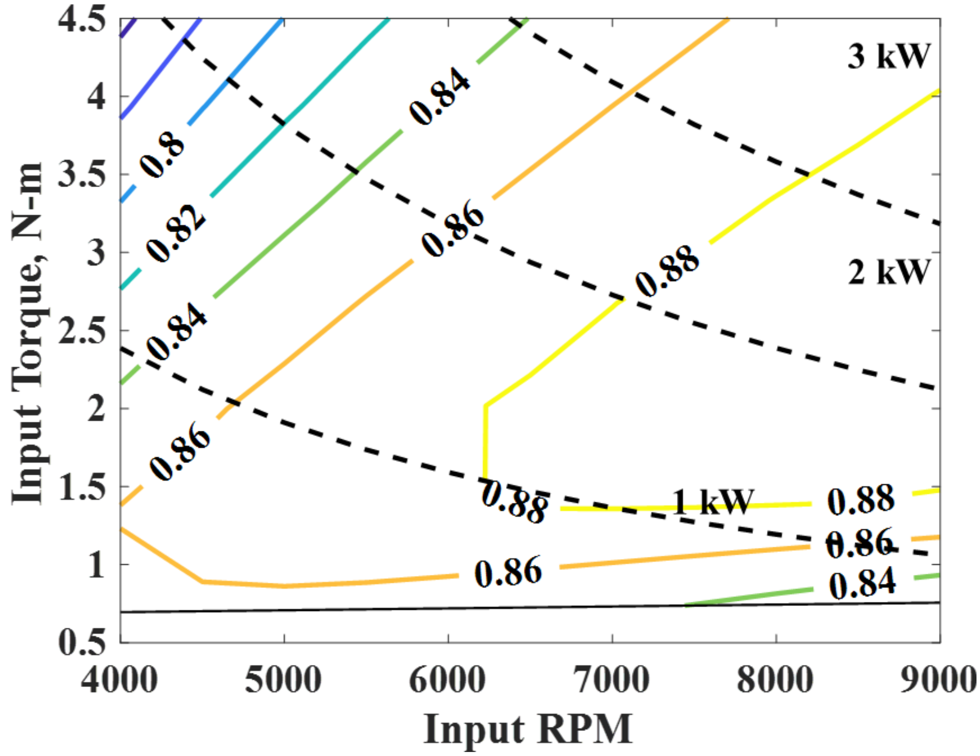

Figure 3.13. Input torque versus RPM with generator efficiency contours; 7.2 kW generator

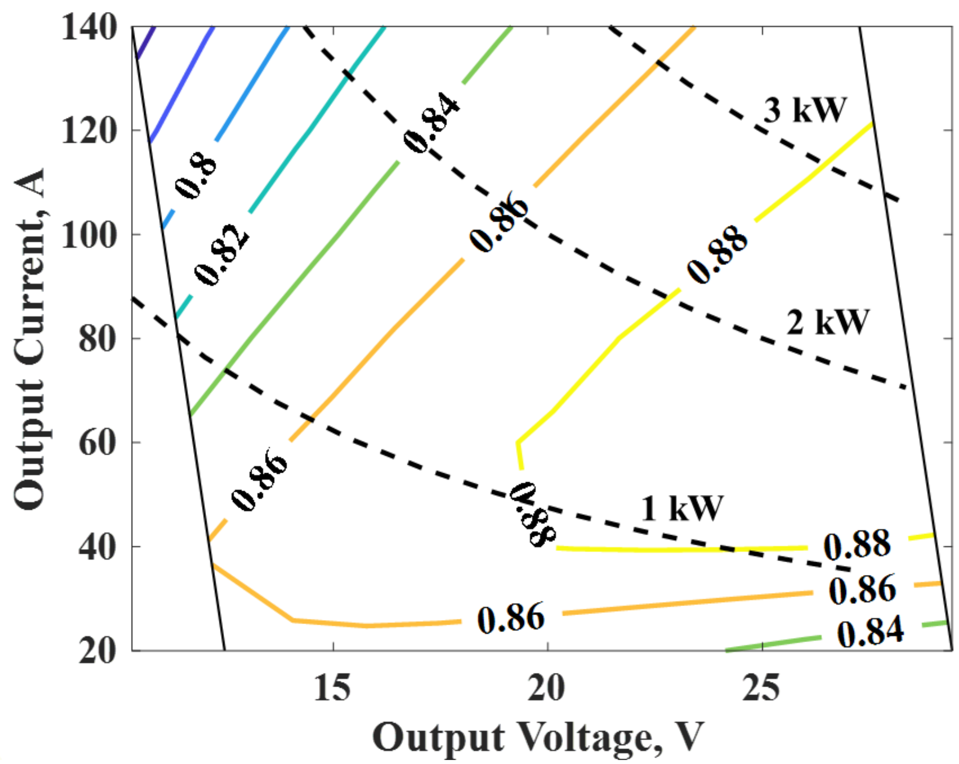

Figure 3.14. Output current versus voltage with generator efficiency contours; 7.2 kW generator

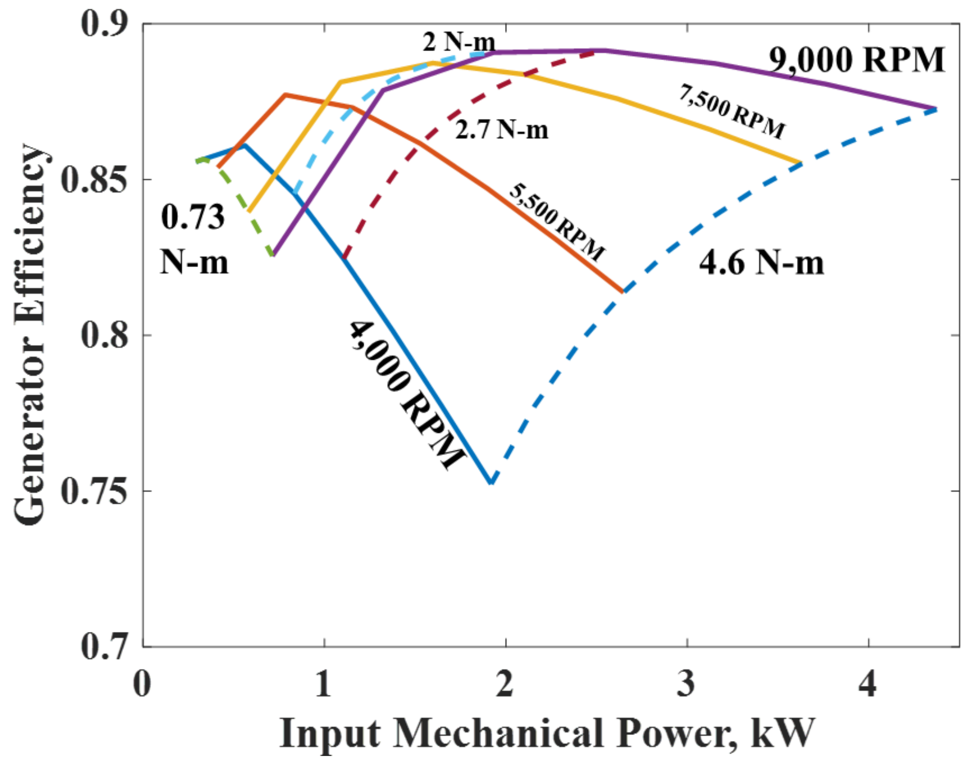

Figure 3.15. Generator efficiency versus input mechanical power with input RPM and torque contours; 7.2 kW generator

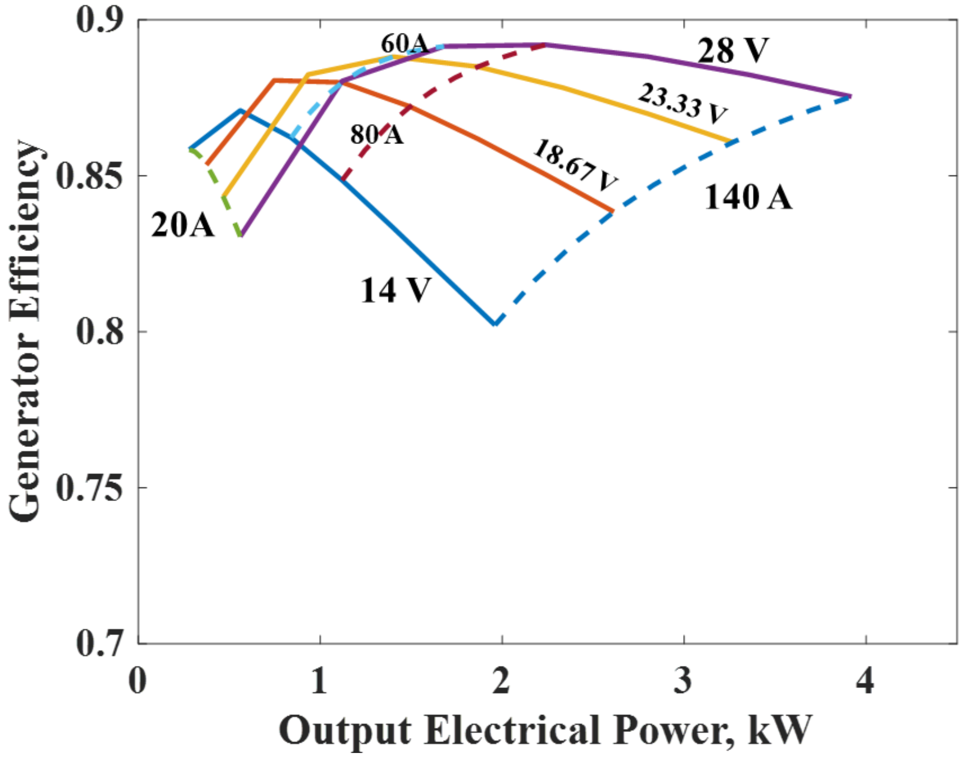

Figure 3.16. Generator efficiency versus input mechanical power with output voltage and current contours; 7.2 kW generator

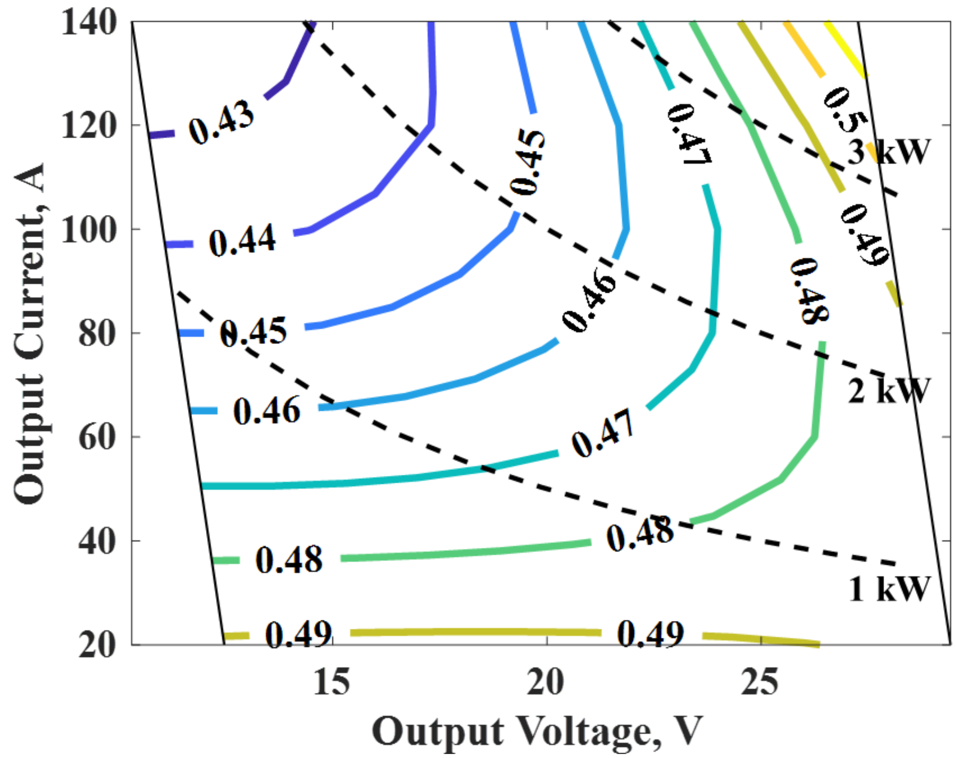

Figure 3.17. Engine-generator output current versus voltage with specific fuel consumption contours (kg/kW-hr) and constant power curves; 7.2 kW generator

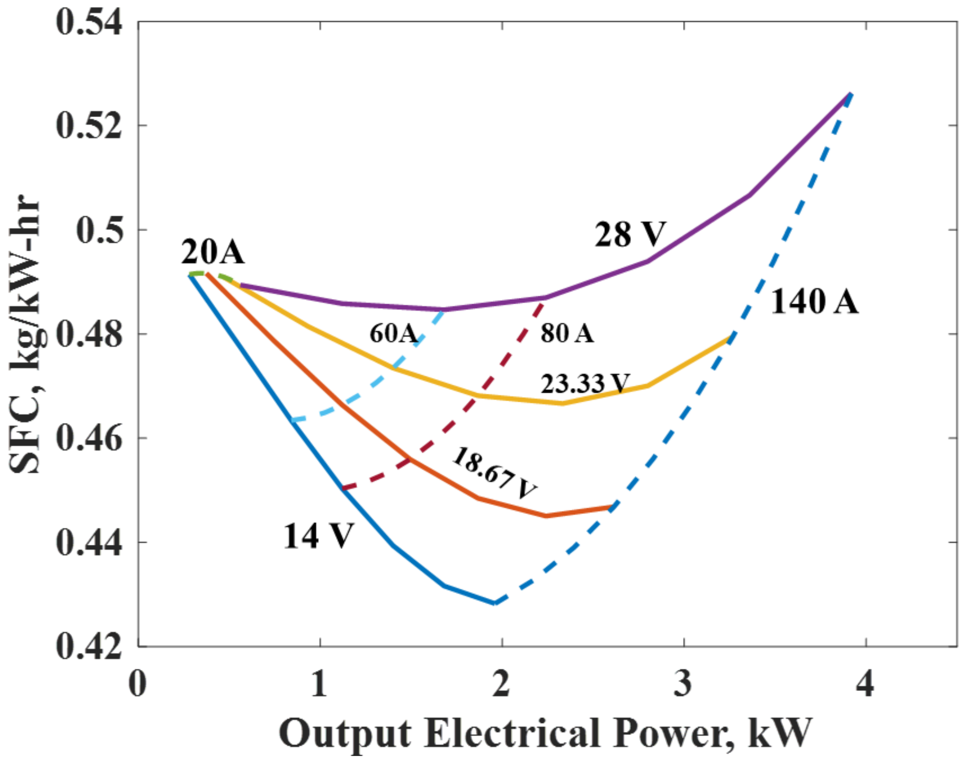

Figure 3.18. Engine-generator specific fuel consumption (kg/kW-hr) versus output electrical power with output voltage and current contours; 7.2 kW generator

The fuel efficiency of the combined engine-generator system is shown in Figure 16, with constant power lines marked. Figure 3.17 plots SFC contours as a function of output current and voltage. Comparing Figure 3.17 with Figures 3.11 and 3.13, it reveals that the SFC of the combined engine-generator system is still influenced more by the engine than the generator. Figure 3.18 plots the SFC as a function of power with constant current and voltage lines marked. Once again, the same conclusions carry over from earlier engine-generator combination. Generator voltage, or equivalently engine speed, is the key factor and should always be changed for any change in power.

3.2. Engine - Generator with One Electric Drive

The goal of the engine-generator with one electric drive tests was to measure the electrical efficiency of the motor at various input voltages, and output torques and rotor speeds.

3.2.1. Test Setup

The schematic and corresponding testbed setup are shown in Figures 3.19 and 3.20, respectively. The engine-generator setup is identical to previous studies (Figure 3.1 and 3.2), but on the load side, the DC load bank is removed and an electric motor with electronic speed controller (ESC) is connected to the rectifier. The motor speed is measured with a Hall-effect sensor mounted on the motor body. Torque was measured using a reactionary torque transducer mounted between the motor and the rigid test stand. Since the motor is the only electrical load connected to the generator, generator output voltage and current is equal to the motor input voltage and current. The motor current was not directly regulated. Instead, motor duty cycle is regulated using a PWM controller connected to the ESC. The duty cycle regulates rotor speed, measured in RPM. The current drawn is a function of the rotor load torque. In order to exercise the full range of RPM and torques available from the motor, high-profile-drag paddles, shown in Figure 3.21, were constructed. The wooden propeller was only used for the lowest torques. Note, the KDE7208XF-110 motor has a maximum continuous current of 50A. As such, testing was conducted with only the 4.4-kW KDE7215XF-135 generator, as it could provide the maximum continuous current over the full voltage range.

3.2.1. Test Procedures

For each test sequence, the engine speed was increased to high idle, then the current load was applied by activating the ESC. The engine speed was then adjusted to the first generator voltage value and held steady. After 1 minute data acquisition was initiated. At the end of the data acquisition period, (another 1 minute), rotor speed was increased to the next condition, and the

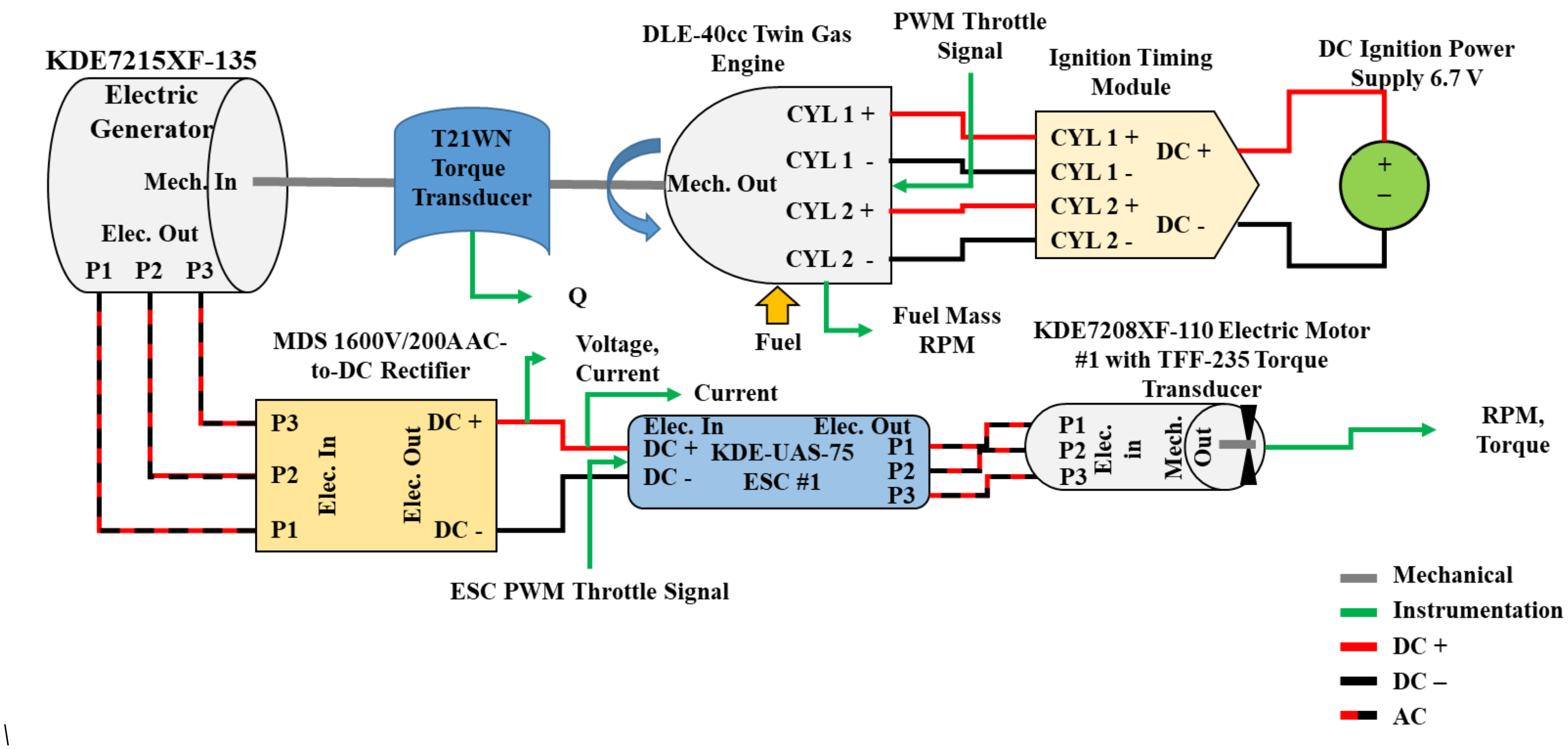

Figure 3.19. Schematic of the engine-generator with a single electric drive

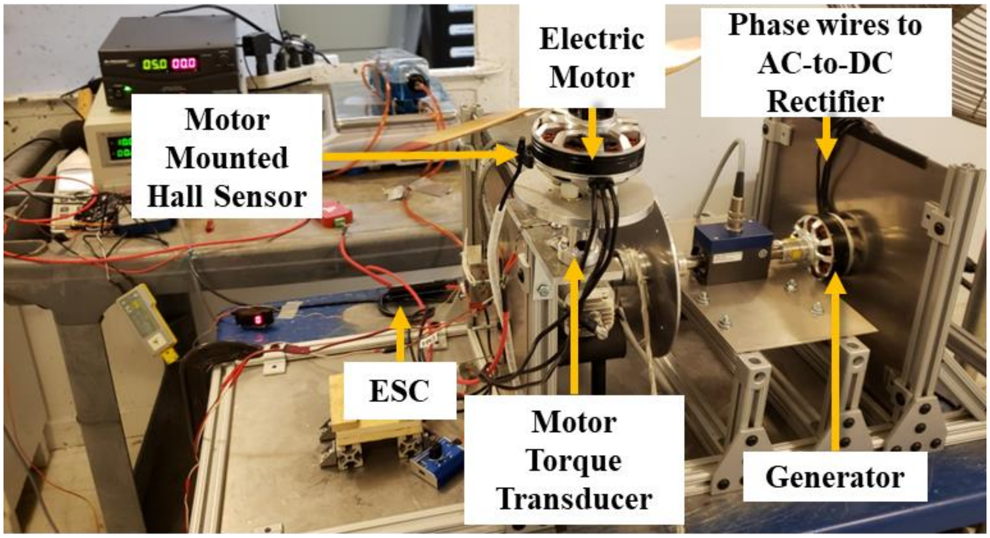

Figure 3.20. Schematic of the engine-generator with single electric motor

Figure 3.21. High-profile-drag rotors and a wooden propeller

generator voltage readjusted to the required value prior to repeating the data acquisition process. At the end of a full rotor RPM sequence, the engine was shut down and refueled. The rotor was replaced with a larger rotor/paddle. Once the engine and motor cooled to room temperature the test sequence was repeated for the next rotor. For each rotor, the control signal was increased from zero to maximum RPM. Ten test points were selected at uniform RPM intervals up to the maximum RPM for a total of 50 rotor torque and RPM combinations. Measurements were taken for three generator voltages, in other words three engine speeds, for a total of 150 test points.

3.2.2. Results

As the behavior of the engine and generator was already studied previously, the behavior of the motor is isolated here. As previously stated, the isolated motor tests were conducted with only the 4.4-kW KDE7215XF-135 generator, as it could provide the maximum continuous current over the full voltage range. The behavior of the combined systems is deferred to the next section when all four motors are powered, and the full range of engine power is exercised.

The electrical efficiencies of the isolated motor and ESC are shown in Figures 3.22 to 3.24, with constant power lines marked. Figures 3.22 to 3.24 plot motor efficiency contours as a function of rotor torque and RPM for three voltages, 25-, 37.5-, and 50-V respectively. It is clear that maximum rotor RPM is a function of generator voltage, and that maximum efficiency of the motor occurs at the maximum rotor RPM. Figures 3.25 to 3.27 plot the same efficiency but now a function of power with constant rotor torque and RPM lines marked. The importance of generator voltage is once again apparent. To reduce power, it is most efficient to reduced generator voltage. For example, from Figures 3.26 and 3.27, operation at 4.2 N-m torque and 3110 RPM is far more efficient at 37.5V (73%) than at 50V (58 %). Similarly, from Figures 3.25 and 3.27, operation at 4.2 N-m torque and 1730 RPM is far more efficient at 25V (65%) than at 50V (30 %).

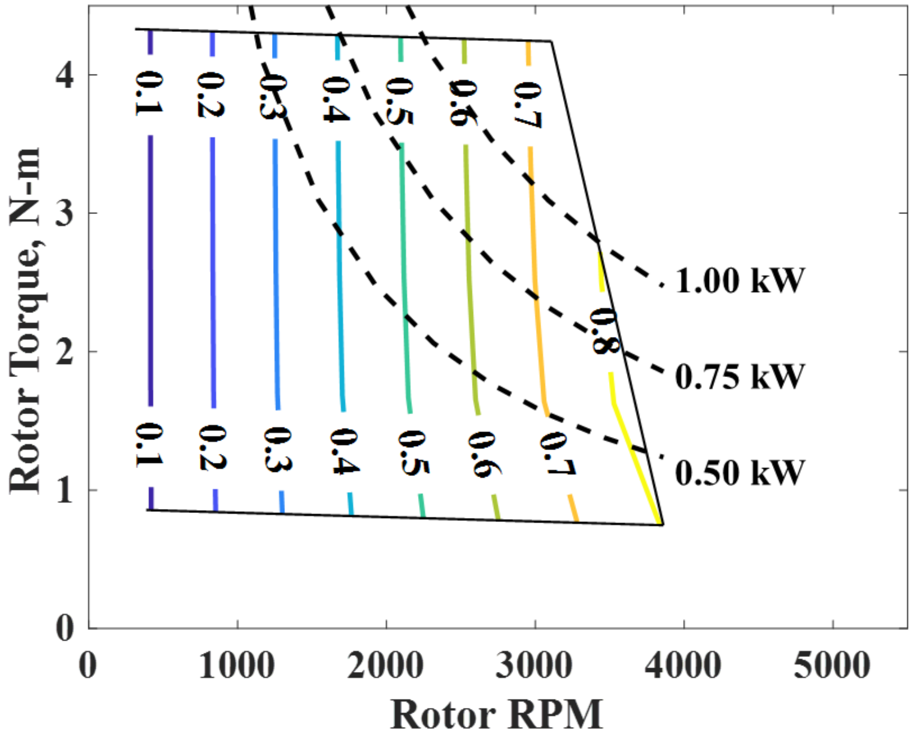

Figure 3.22. Rotor torque versus RPM with electric motor efficiency contours and constant power curves for 25 V

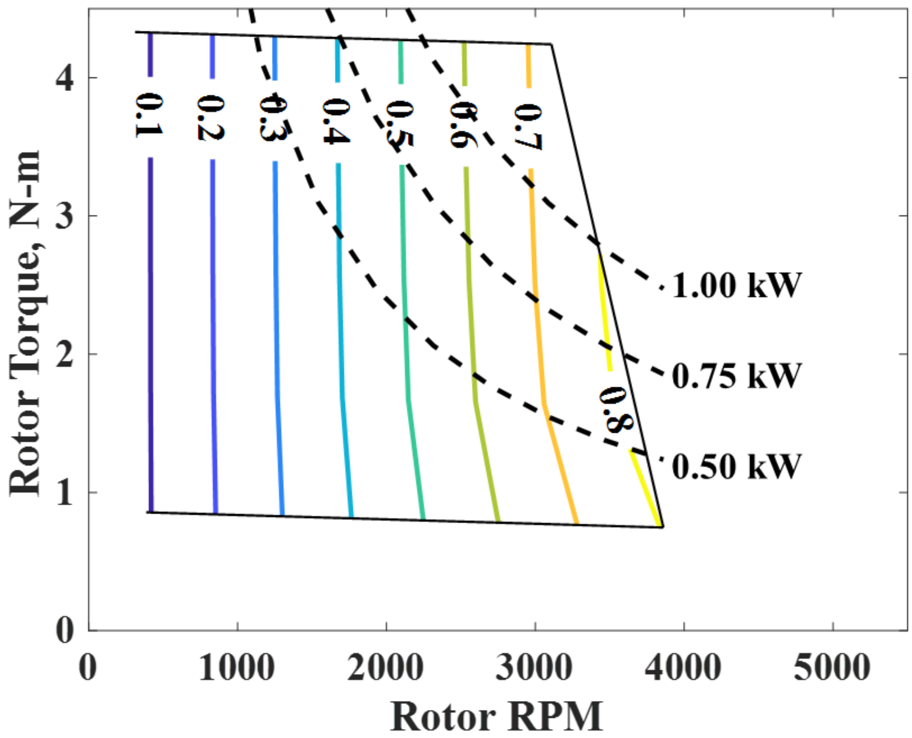

Figure 3.23. Rotor torque versus RPM with electric motor efficiency contours and constant power curves for 37.5 V

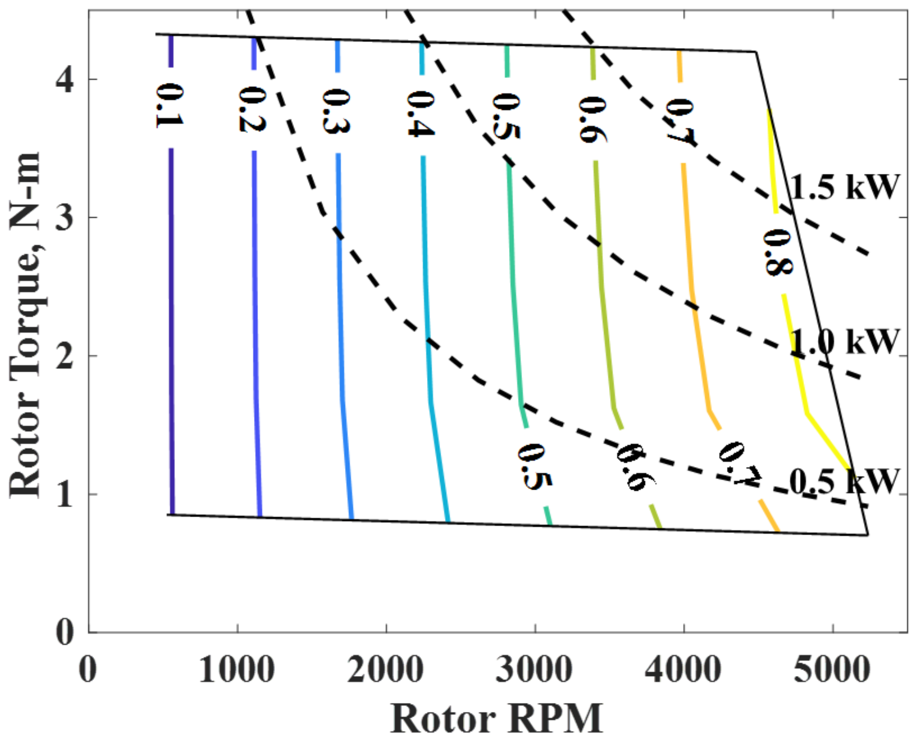

Figure 3.24. Rotor torque versus RPM with electric motor efficiency contours and constant power curves for 50 V

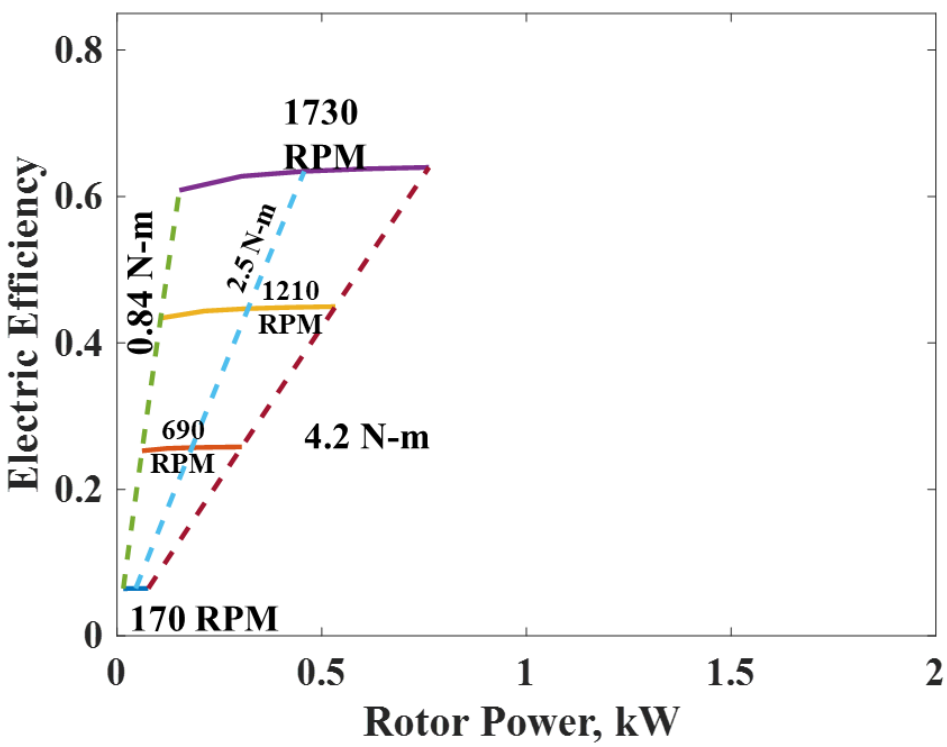

Figure 3.25. Electric motor efficiency versus output rotor power with output RPM and torque contours for 25 V

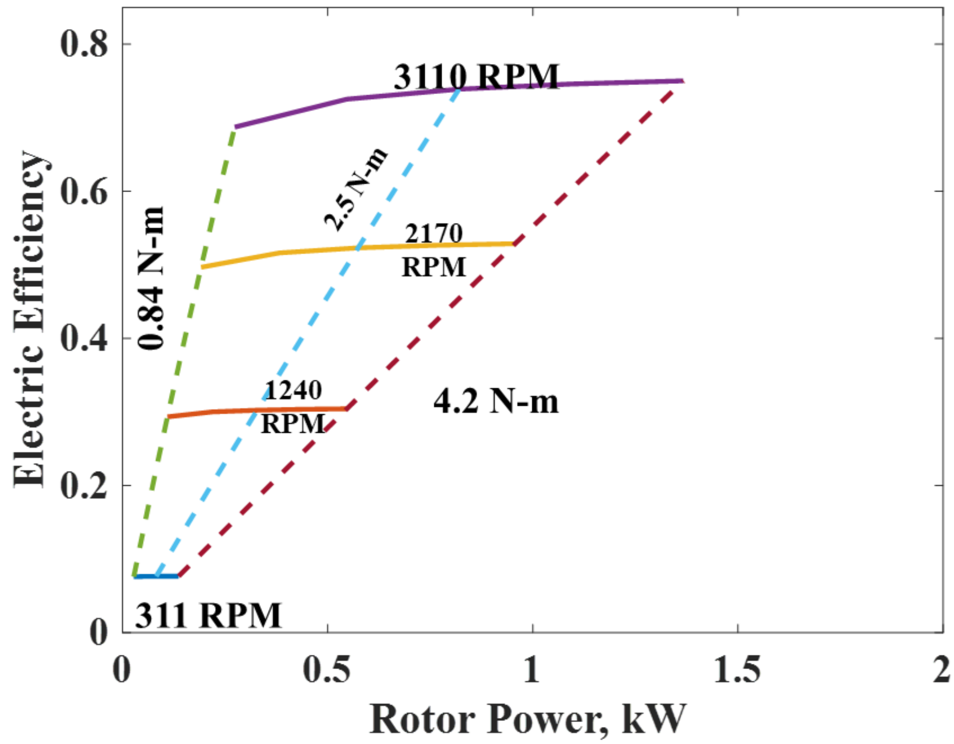

Figure 3.26. Electric motor efficiency versus output rotor power with output RPM and torque contours for 37.5 V

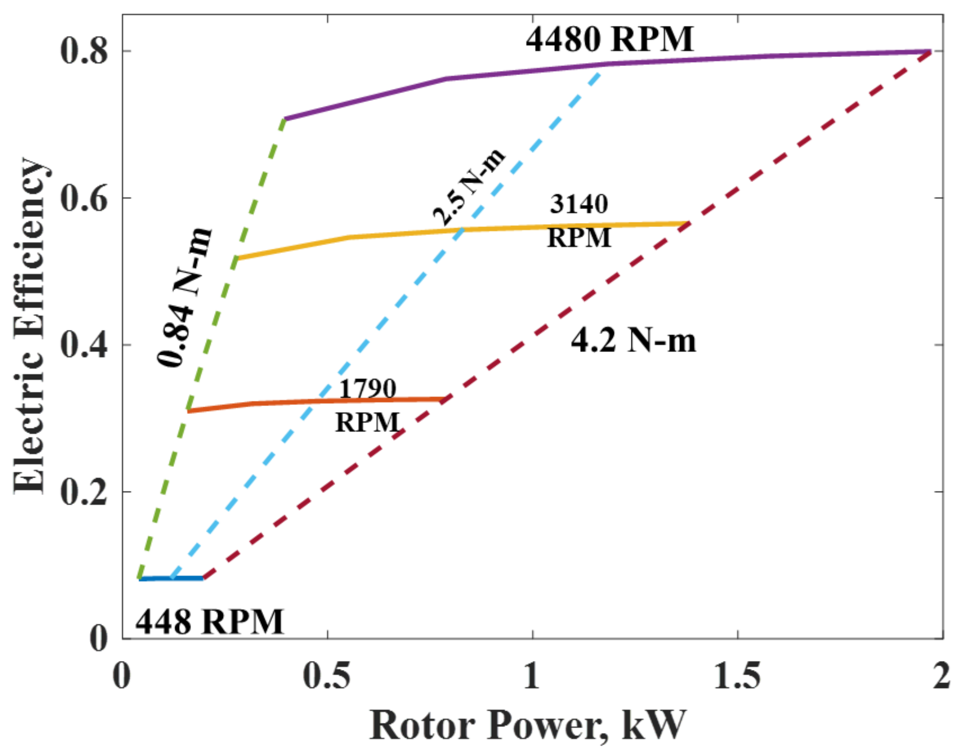

Figure 3.27. Electric motor efficiency versus output rotor power with output RPM and torque contours for 50 V

3.3. Engine-Generator with Four Electric Drives

The engine-generator with four drives represents the full powertrain. The goal is to measure the fuel efficiency of the engine at various output rotor torques and speeds, at three generator voltages as parameters.

3.3.1. Setup

The schematic and corresponding testbed setup are shown in Figures 3.28 and 3.29, respectively. It is similar to the single motor setup (Figures 3.19 and 3.20) but with three additional motors with individual ESCs, all connected to the rectifier in parallel. The motors are connected to identical drag loads (Figure 3.21), and to a single pulse width modulated voltage signal for control inputs. The voltage is the same for all motors, so RPM is expected to be the same. The current drawn is a function of the torque. Only one motor is instrumented for torque and RPM, however, it assumed they are the same for identical voltages and control signals.

3.3.1. Test Procedure

The test procedure was the same as the engine-generator with one motor. Each motor utilized identical rotors and was controlled with an identical PWM signal. Five rotor sets were tested at 10 RPM points for a total of 50 rotor torque and RPM combinations. Measurements were taken for three generator voltages, in other words three engine speeds, for a total of 150 test points.

3.3.2. Results from the 4.4 kW KDE7215XF-135 Generator

The SFC contours as a function of rotor torque and RPM are shown in Figures 3.30 to 3.32, with constant power lines marked. Fuel efficiency is a function of rotor torque, rotor RPM, and the generator voltage (engine speed). Since generator voltage is held constant, Figure 3.30

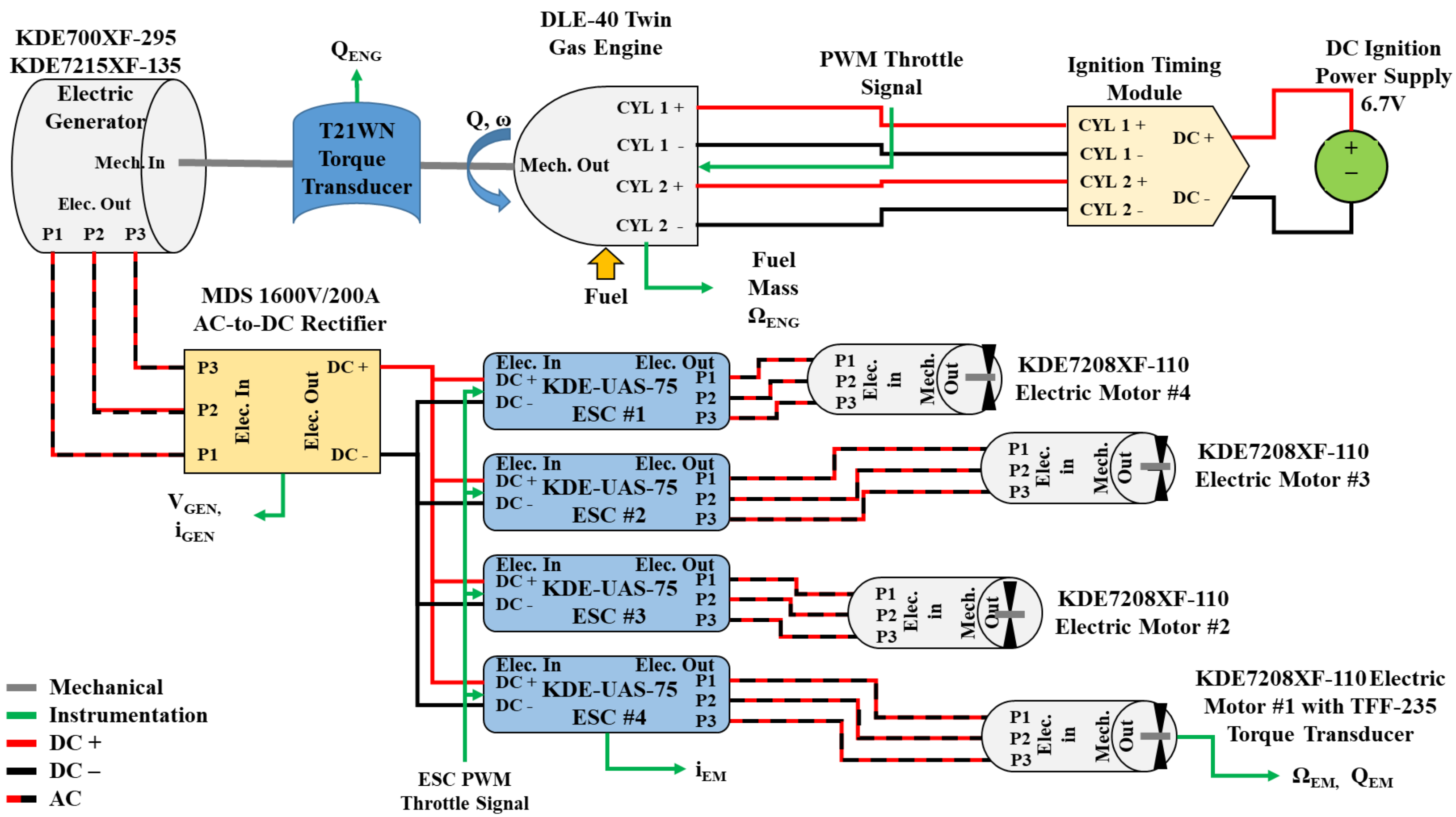

Figure 3.28. Schematic of the engine-generator with four electric drives

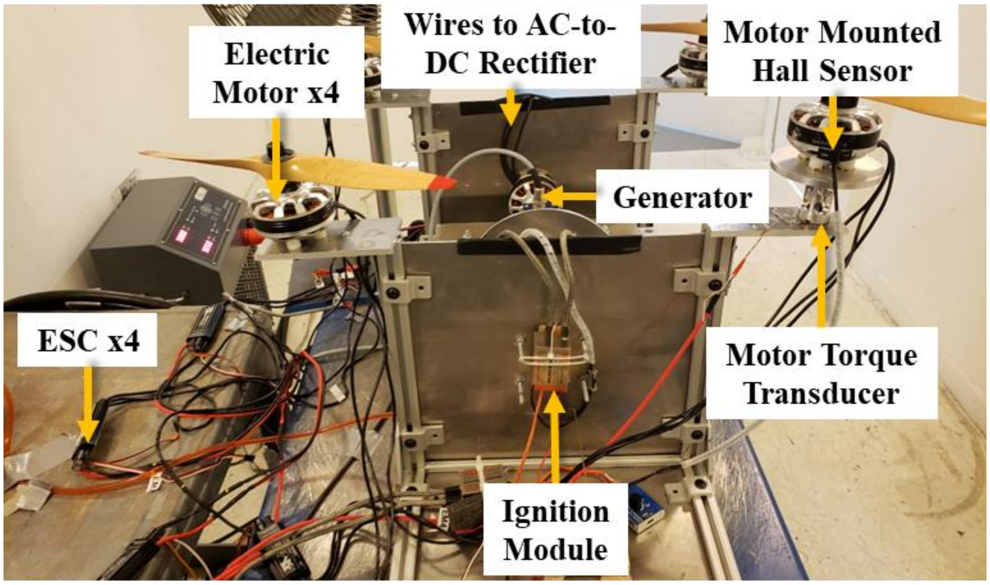

Figure 3.29. Instrumented engine-generator with four electric motors

represents the rotor torques and rotor RPM possible for a vertical cross-section of Figure 3.9. Figures 3.33 to 3.35 plot the fuel efficiency as a function of power with constant rotor torque and rotor RPM lines marked. For any given voltage, there is a constant torque line which provides the most fuel-efficient operation. Two key conclusions are drawn from Figure 3.22. First, to reduce power, it is most efficient to reduce rotor RPM at constant torque. For example, suppose the hover point is 2 kW at 4480 RPM and 4.2 N-m of torque. It is significant to note that the hover condition can only be achieved at 50V. To reduce to a cruise power of 1 kW, (while maintaining a constant voltage of 50V), a fixed-pitch rotor requires a reduction in RPM which results in a corresponding reduction in torque. This torque reduction reduces fuel efficiency.

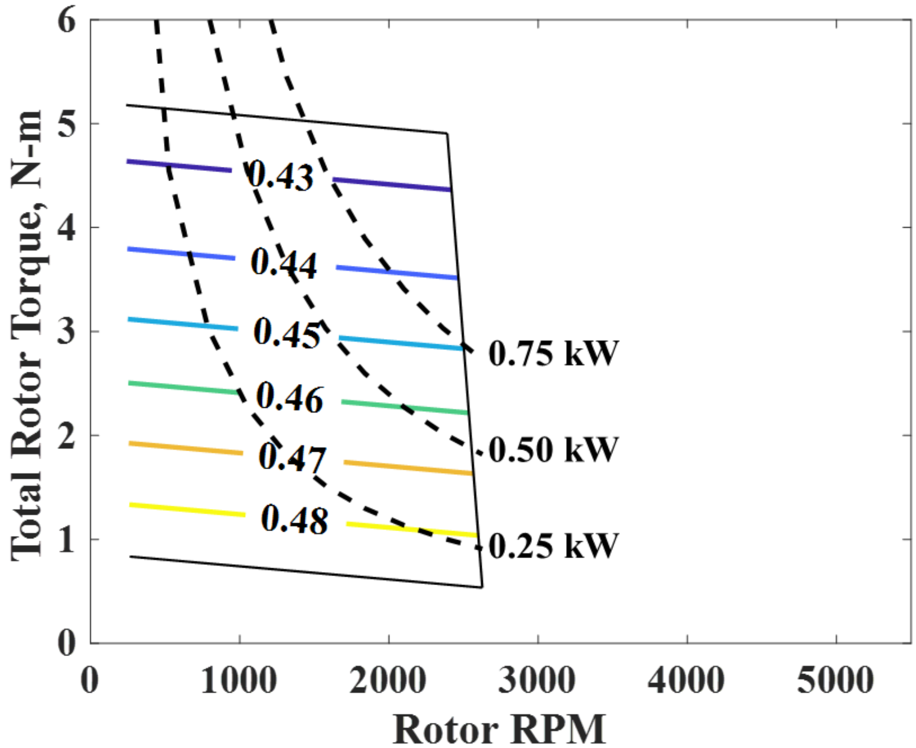

Figure 3.30. Total rotor torque versus RPM with engine-generator specific fuel consumption (kg/kW-hr) contours and constant power curves for 25 V; 4.4 kW generator

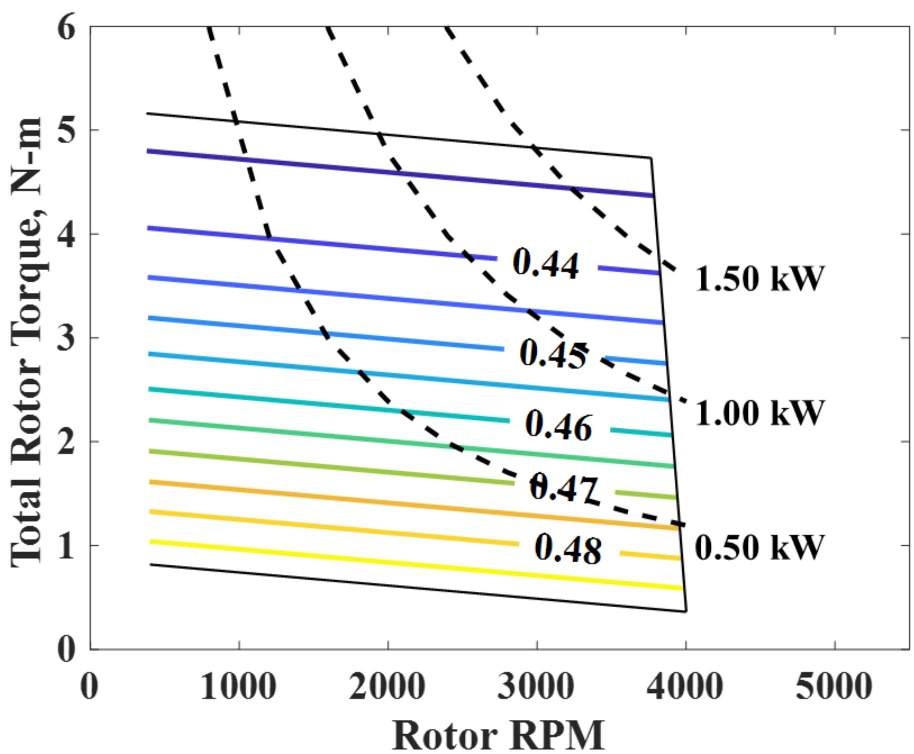

Figure 3.31. Total rotor torque versus RPM with engine-generator specific fuel consumption (kg/kW-hr) contours and constant power curves for 37.5 V; 4.4 kW generator

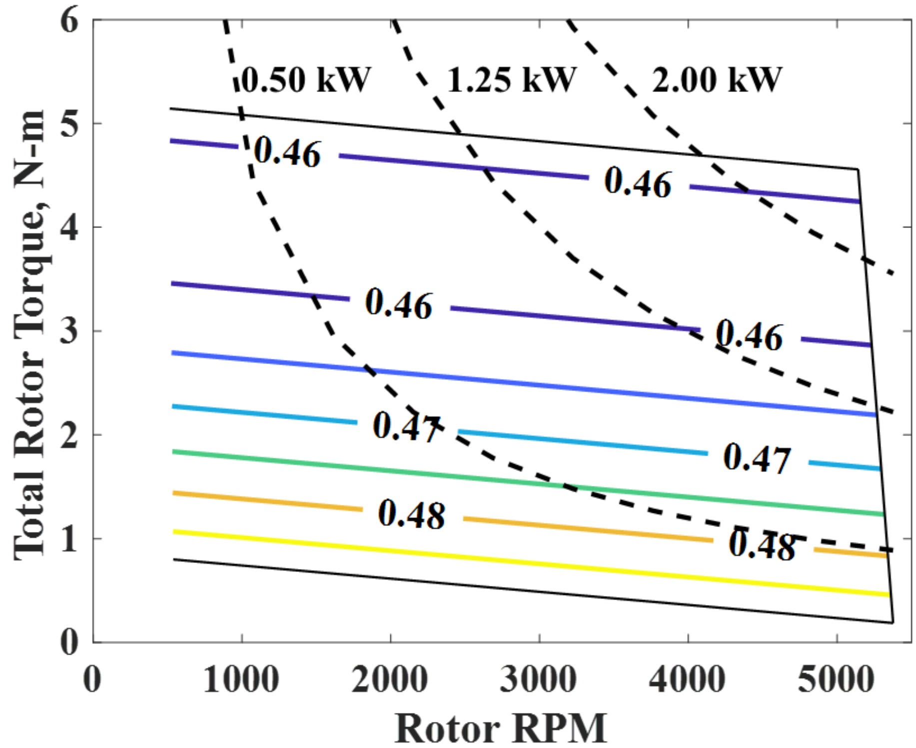

Figure 3.32. Total rotor torque versus RPM with engine-generator specific fuel consumption (kg/kW-hr) contours and constant power curves for 50 V; 4.4 kW generator

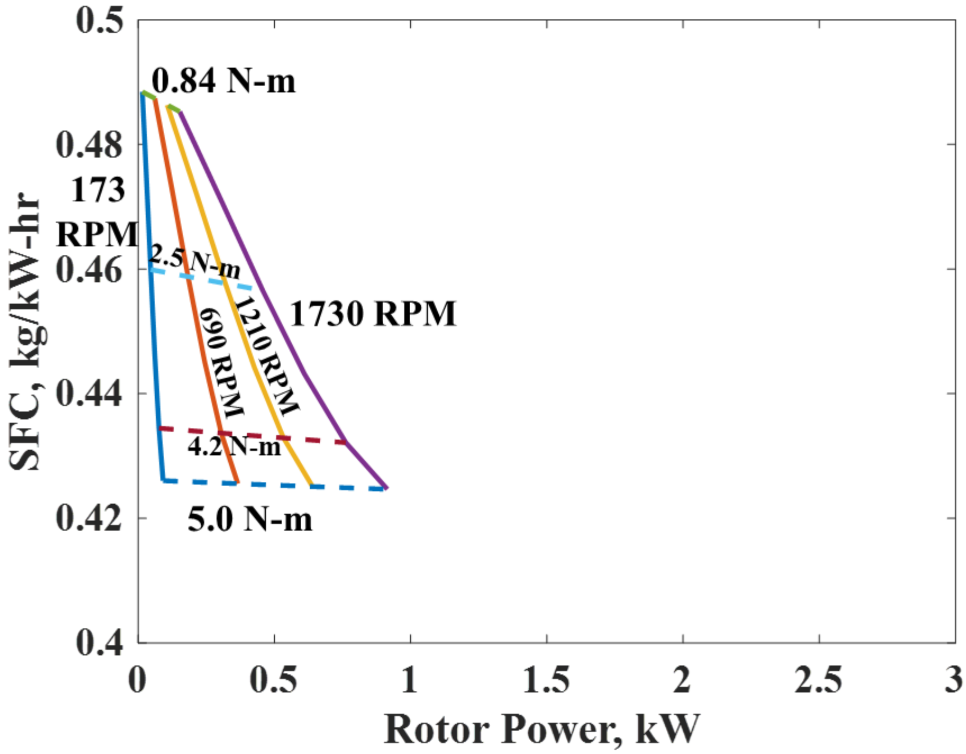

Figure 3.33. Engine-generator specific fuel consumption (kg/kW-hr) versus total output rotor power with output RPM and torque contours for 25 V; 4.4 kW generator

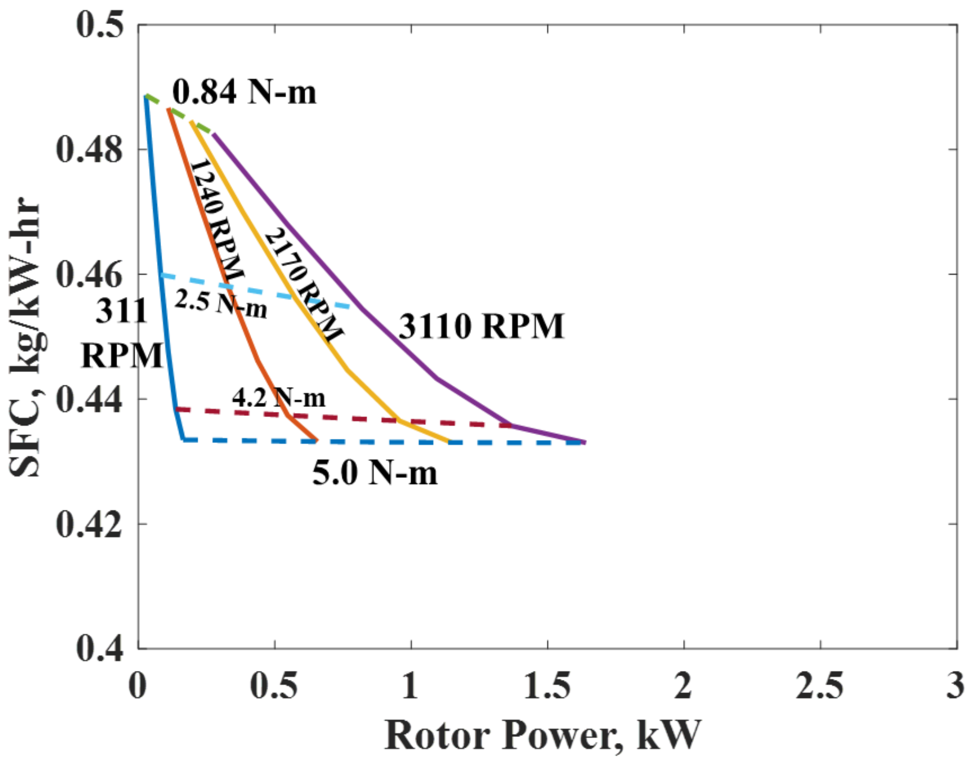

Figure 3.34. Engine-generator specific fuel consumption (kg/kW-hr) versus total output rotor power with output RPM and torque contours for 37.5 V; 4.4 kW generator

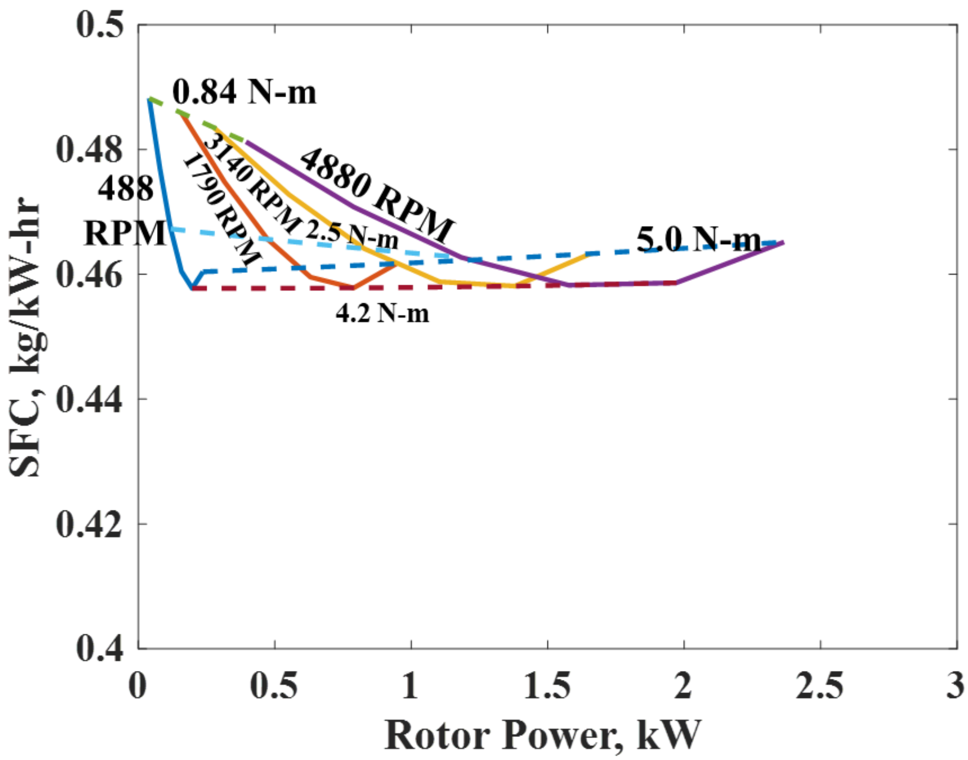

Figure 3.35. Engine-generator specific fuel consumption (kg/kW-hr) versus total output rotor power with output RPM and torque contours for 50 V; 4.4 kW generator

One possible way of countering this reduction in fuel efficiency is to introduce collective pitch control, where the pitch is increased to maintain the 4.2 N-m of torque. Second, it is more efficient to operate at the lowest possible voltage. For example, suppose the rotor is operating at 1730 RPM and 5 N-m. For 50V, the SFC is approximately 0.46 kg/kW-hr. While for 25V the SFC is approximately 0.425 kg/kW-hr, approximately an 8% reduction in fuel consumption. This benefit is a function of torque. For 4.2 N-m torque, the SFC decreased from 0.455 to 0.43 kg/kW-hr. For 0.84 N-m torque the benefit vanishes, the SFC now remains at 0.49 kg/kW-hr for both voltages. Thus, operation at higher torque is always preferred. This mode of operation is different from isolated electric motors where a lower torque is preferred. Thus hybrid-electric powertrains are fundamentally different from all-electric powertrains.

3.3.3. Results from the 7.2 kW KDE700XF-295-G3 Generator

The engine SFC contours as a function of rotor torque and RPM are shown in Figures 3.36 to 3.38, with constant power lines marked. Fuel efficiency is a function of rotor torque, rotor RPM, and the generator voltage (engine speed). Figures 3.39 to 3.41 plot the fuel efficiency as a function of power with constant rotor torque and RPM lines marked. As with the smaller generator, but more apparent now, there is a constant torque line which provides the most fuel-efficient operation for any given voltage. Once again, the same conclusions carry over from earlier discussions, with additional data for clarity. First, to reduce power, it is most efficient to reduce RPM and increase or decrease torque to the constant torque line that provides the minimum SFC. This approach will require collective control of the rotor. Second, it is most efficient to operate at the lowest possible voltage. Generator voltage, in other words engine speed, is the key factor and should always be changed for any change in rotor RPM.

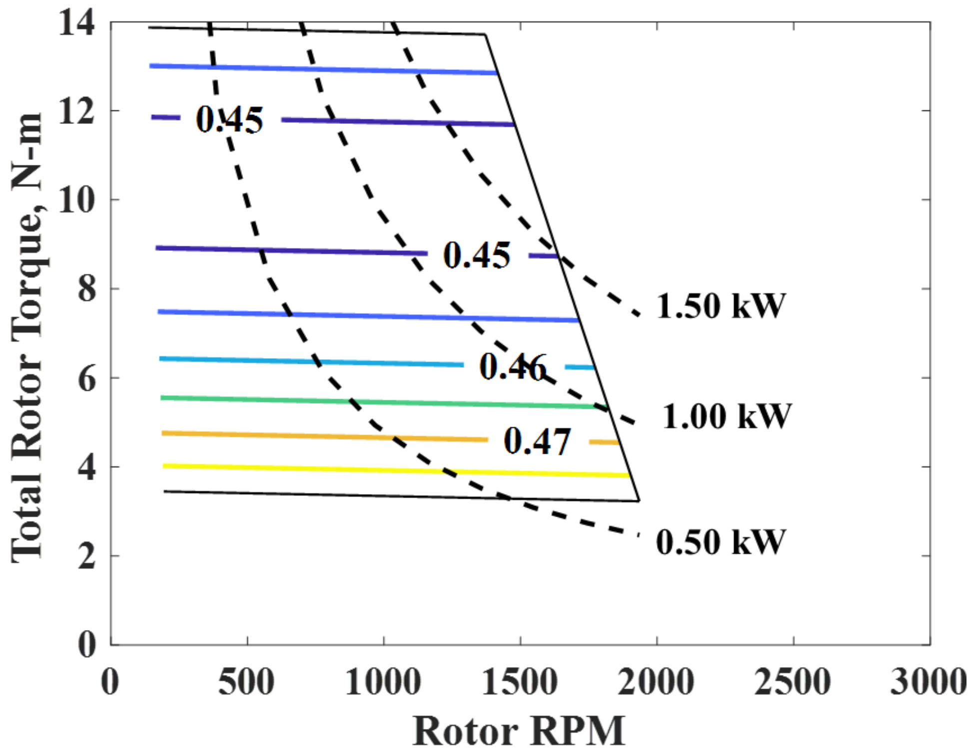

Figure 3.36. Total rotor torque versus RPM with engine-generator specific fuel consumption (kg/kW-hr) contours and constant power curves for 20 V; 7.2 kW generator

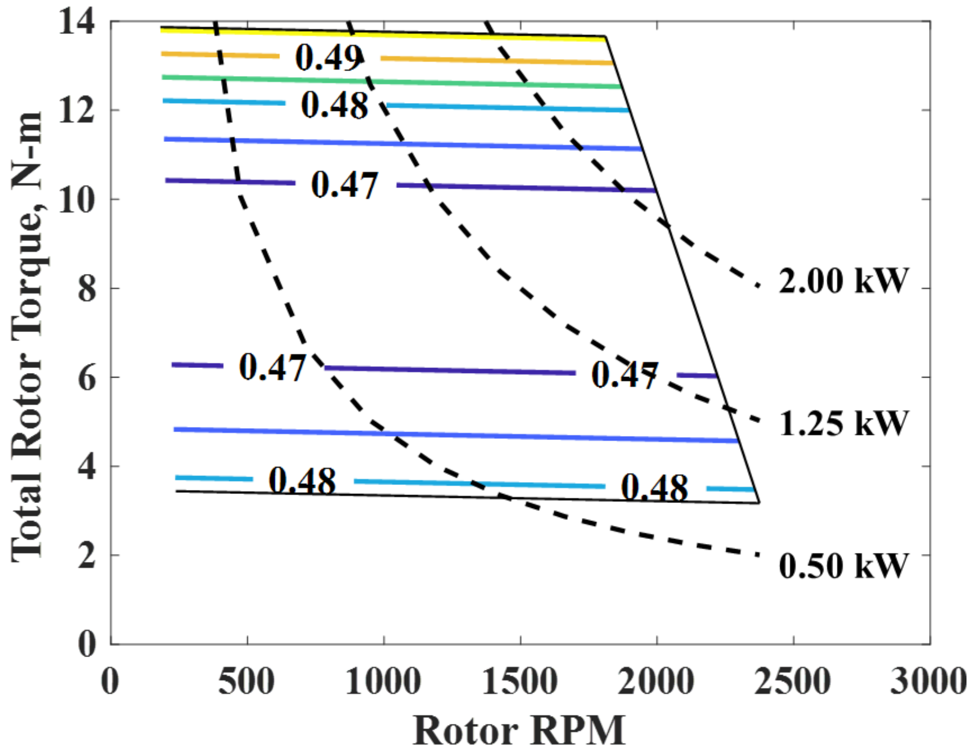

Figure 3.37. Total rotor torque versus RPM with engine-generator specific fuel consumption (kg/kW-hr) contours and constant power curves for 24 V; 7.2 kW generator

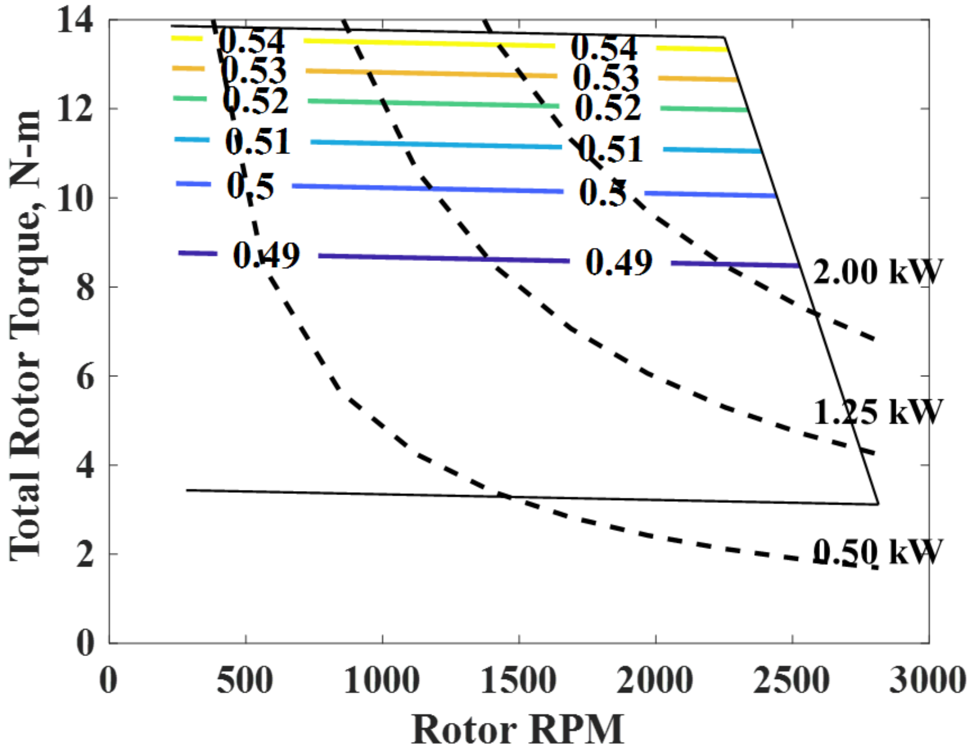

Figure 3.38. Total rotor torque versus RPM with engine-generator specific fuel consumption (kg/kW-hr) contours and constant power curves for 28 V; 7.2 kW generator

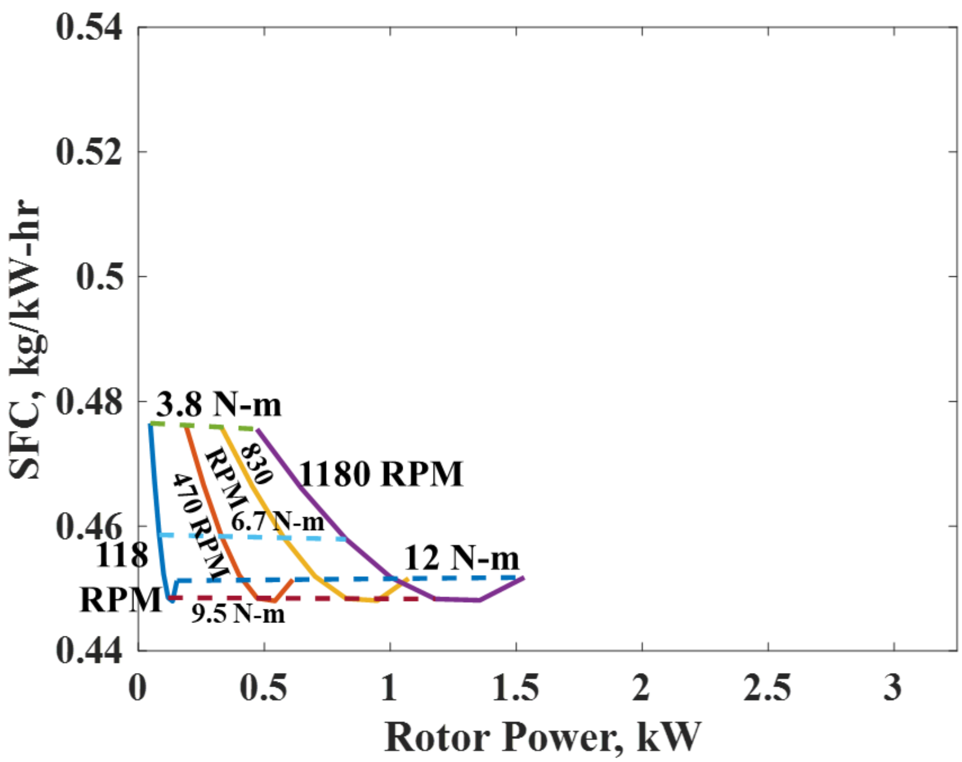

Figure 3.39. Engine-generator specific fuel consumption (kg/kW-hr) versus total output rotor power with output RPM and torque contours for 20 V; 7.2 kW generator

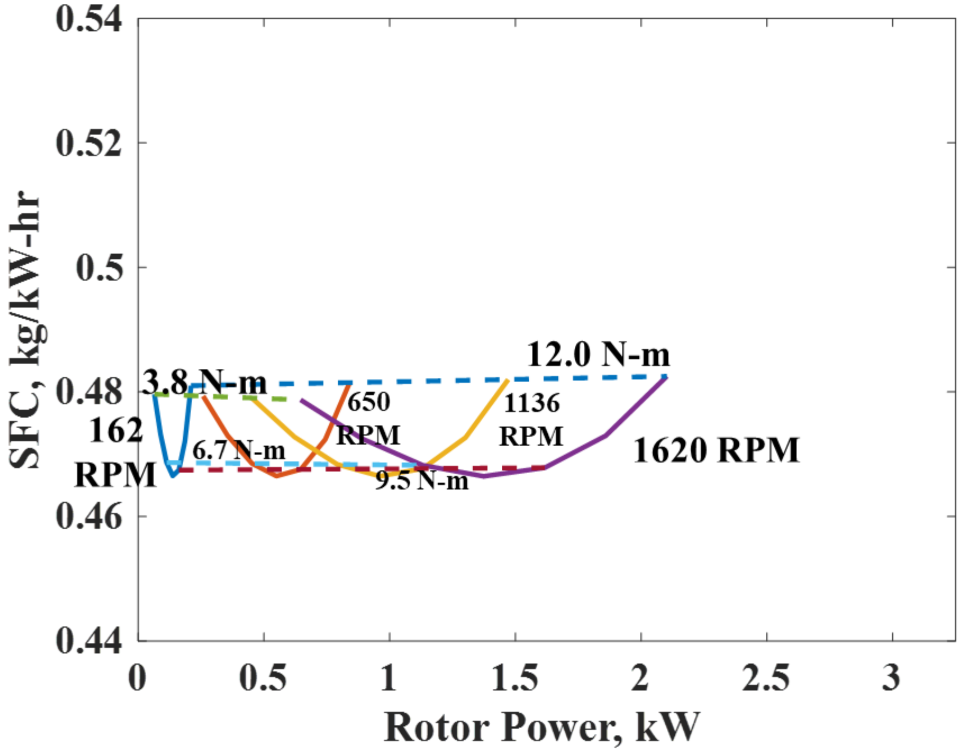

Figure 3.40. Engine-generator specific fuel consumption (kg/kW-hr) versus total output rotor power with output RPM and torque contours for 24 V; 7.2 kW generator

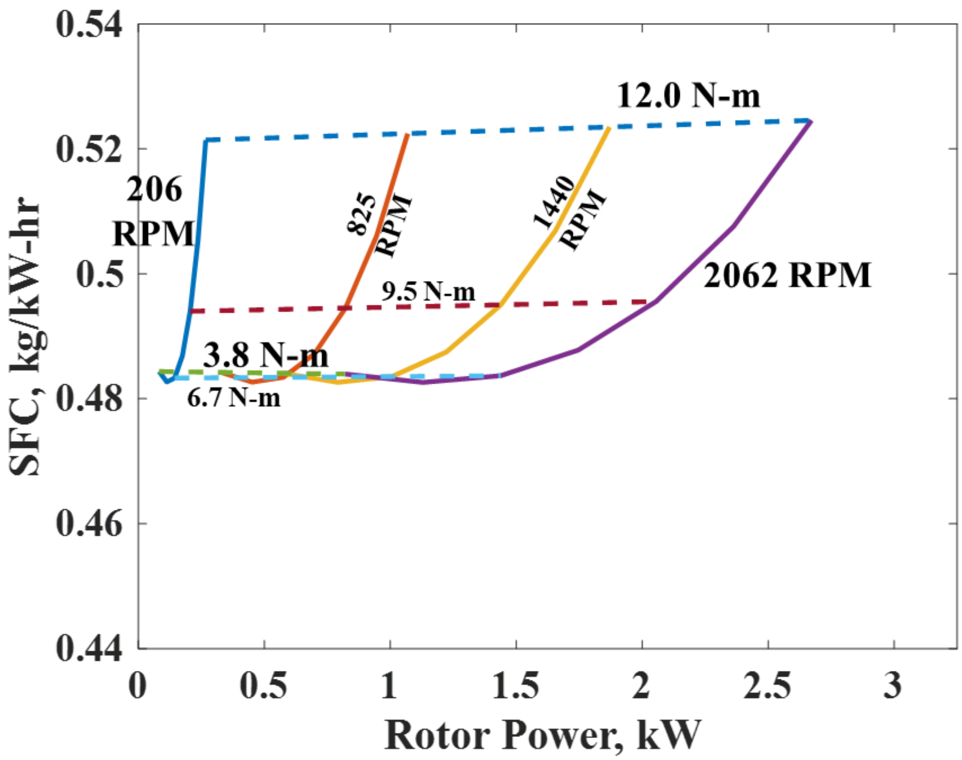

Figure 3.41. Engine-generator specific fuel consumption (kg/kW-hr) versus total output rotor power with output RPM and torque contours for 28 V; 7.2 kW generator

3.4. Chapter Summary and Conclusions

A variable-voltage hybrid-electric powertrain was tested to acquire data and study the fundamental behavior of the system. The study examined the powertrain component by component, as well as in combination with one and four distributed propulsors. Based on this study, the following key conclusions were made:

1. Generator voltage is a key parameter in a hybrid-electric powertrain. The ability to vary this voltage with rotor operating state appears crucial for the optimal specific fuel consumption. Generator voltage is a function of engine speed. Thus, varying engine speed is important, varying rotor speed through the ESC alone is not optimal and can lead to poor overall performance.
2. For any operating state—defined by rotor torque and RPM—the generator voltage should be the minimized as far as possible. The generator voltage limits the maximum rotor RPM, so not all rotor RPM can be achieved at the same generator voltage. Hence, the best generator voltage will vary with rotor RPM as needed during a certain mission segment. This implies for an RPM controlled aircraft, generator voltage is not simply a criterion for design but also for control, if the best specific fuel consumptions are to be achieved.
3. For any generator voltage and rotor RPM, there is a rotor torque that maximizes overall efficiency, i.e., minimizes specific fuel consumption. A method for adjusting the rotor torque, such as collective pitch control is also desired if the best specific fuel consumption is to be achieved.
4. For an integrated powertrain, specific fuel consumption is a function of generator voltage, i.e., engine speed, rotor RPM, and rotor torque—in that order of

importance. By analyzing a reduction in power scenario representing a hover-to-cruise transition, it was found that the most efficient change in power results from a combination of reducing engine RPM and increasing rotor torque, and vice versa.

5. Greater torque and lower RPM are generally desired from rotors of a hybrid-electric aircraft because the overall system is influenced more by the engine-generator than the electric motor. This mode of operation is fundamentally different from an all-electric drive, where lower torque and higher RPM is normally the most beneficial
6. Of all the components for the system—engine, generator, and motors—the generator appears crucial for achieving maximum power at a given rotor RPM. Given an engine and a set of motors, the generator should be selected or designed for the maximum current corresponding to the maximum rotor torque desired at a certain RPM. Improper selection of the generator can result in a rotor starved of torque.

Chapter 4: Two-Stroke Reciprocating Engine Model

This chapter develops models for predicting engine fuel consumption and weight for the design of a hybrid-electric aircraft.

4.1. Introduction

The DLE-40 engine tested earlier is used as a basis for development of the models. Recall the DLE-40 is a 40-cc, two-stroke twin-, opposed-cylinder engine. It is a naturally-aspirated, carbureted engine and uses a gasoline-oil mixture for fuel. The specific fuel consumption describes the fuel efficiency of the engine. The lower the specific fuel consumption the more efficient the engine. The weight model is required as a function of brake power.

4.2. Fuel Consumption Model

The fuel consumption model predicts brake specific fuel consumption ($bsfc$) as a function of engine brake torque and RPM. The user inputs the cycle count, swept cylinder volume, the net calorific value of the fuel and the engine thermal efficiency constants. The engine thermal efficiency constants are to be found from test data. Thus, it is a semi-empirical model.

Internal combustion (IC) engines convert chemical energy into useful work through combustion of a fuel. In reciprocating engines, the power, P (W), produced by the piston, and consequently the torque, Q (N-m), applied by the crankshaft are proportional to the cylinder pressure during the piston cycle. As pressure varies greatly throughout one cycle, an equivalent mean effective pressure, mep (Pa), is defined. The mean effective pressure is the constant pressure which would yield the same work, W (J) done by the piston in one cycle if multiplied with the swept cylinder volume, V_S (m^3), $W = mep V_S$. A typical pressure cycle with the mean effective pressure is shown in Figure 4.1. The swept cylinder volume is shown in Figure 4.2. Let $n_c$be the number of output revolutions per piston cycle (n_c =1 for two-stroke engines). Let Ω_E be the engine angular velocity in rad/s. Then $\Omega_E/(2\pi)$ is the number of output revolutions per second, $\Omega_E/(2\pi n_c)$ is the number of piston cycles per second, and $W\Omega_E/(2\pi n_c)$ is the work done in one second. Hence $P = W\Omega_E/(2\pi n_c)$ and $W = P(2\pi n_c)/\Omega_E$. Since power and torque are related as $P = Q\Omega_E$, we can also define mep as a function of engine torque, per Equation 4.1.

$$mep = \frac{W}{V_S} = \frac{2\pi n_c}{V_S}\frac{P}{\Omega_E} = \frac{2\pi n_c}{V_S}Q \tag{4.1}$$

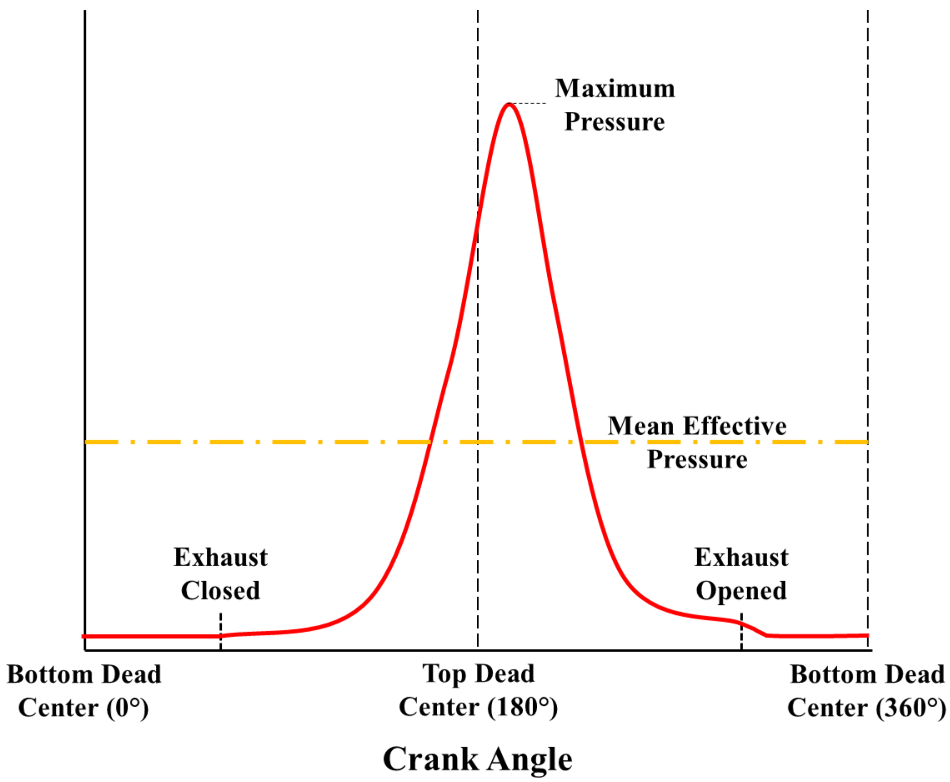

Figure 4.1. Typical pressure cycle of a naturally-aspirated, carbureted, two-stroke piston

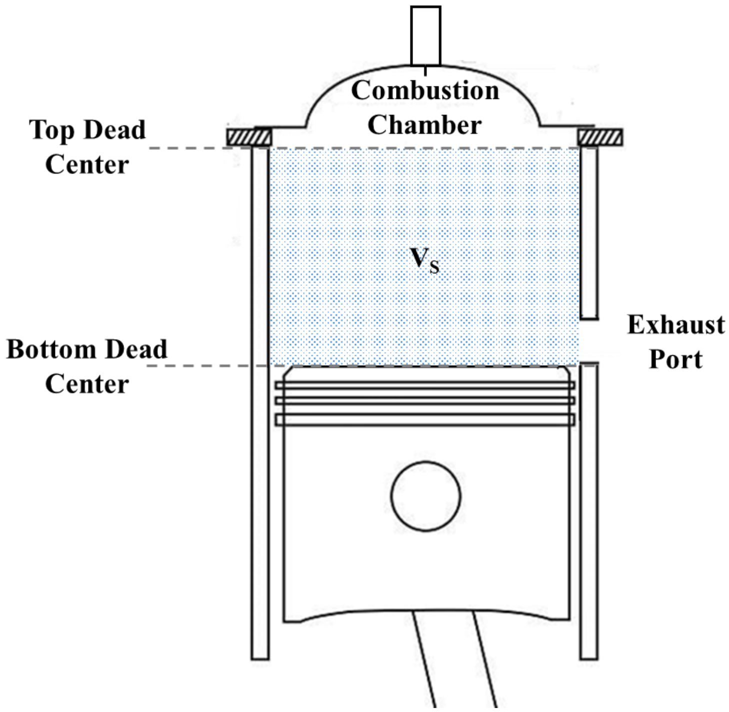

Figure 4.2. Cylinder Geometry

Four types of power are typically defined when modeling an IC engine: 1. Fuel Power, P_{Fuel}; 2. Indicated Power, P_{IN}; 3. Brake power, P_B; and 4. Friction Power, P_F. Fuel Power is the rate of heat energy produced by combustion. It is the product of the fuel mass flow rate, $\dot{m}_{Fuel}$ (kg/s), and the net calorific value of the fuel, NCV (J/kg), Equation 4.2. It is assumed that the water produced from combustion is in vapor form, hence the NCV is the lower heating value of the fuel. The NCV is determined by subtracting the heat of vaporization of the water from the heat of combustion for the fuel. Indicated power is the portion of the fuel power that is converted to work. Thus, it is the fuel power multiplied by an indicated thermodynamic efficiency, η_T, Equation 4.3.

$$P_{Fuel} = \dot{m}_{Fuel} NCV \tag{4.2}$$

$$P_{IN} = \eta_T P_{Fuel} \tag{4.3}$$

Brake power is defined as the net output power of the engine, Equation 4.4. Friction power, P_F, is the power required to overcome the friction between the piston and the cylinder. In general, there are also the piston pumping power, P_P (zero for two-stroke engines), air charging power, P_C

(zero for naturally aspirated engines i.e no inlet charging), accessory power, P_{AX} (zero for the engine alone), and power recovered from an exhaust turbine, P_T (zero for no turbine) [18]. This reduces Equation 4.4 to $P_B = P_{IN} - P_F$ for the present engine. Brake power can also be written in terms of a brake thermal efficiency, η_B, Equation 4. 5.

$$P_B = P_{IN} - (P_F + P_P + P_C + P_{AX} - P_T) \qquad (4.4)$$

$$P_B = \eta_B P_{Fuel} \qquad (4.5)$$

Thus, in general there are two important efficiencies, Equations 4.6 and 4.7, describing the amount of the fuel energy is converted into usable work and useful work respectively.

$$\eta_T = \frac{P_{IN}}{P_{Fuel}} = \frac{P_{IN}}{\dot{m}_{Fuel} NCV} \qquad (4.6)$$

$$\eta_B = \frac{P_B}{P_{Fuel}} = \frac{Q\Omega_E}{\dot{m}_{Fuel} NCV} \qquad (4.7)$$

Indicated power, brake power, and friction power can also be used to define the corresponding indicated mean effective pressure ($imep$), brake mean effective pressure ($bmep$), and friction mean effective pressure ($fmep$). Thus, in Equation 4.1, mep is in fact $bmep$ if P, Q, and $V_S$are the brake engine power, brake engine torque, and total engine swept cylinder volume. To develop the state Equations for the engine, brake thermal efficiency is rewritten as a function of the indicated thermal efficiency and mean effective pressures. From Equation 4.7 and 4.8, the fuel mass flow rate (kg/s) is defined, Equation 4.9

$$\eta_B = \frac{P_B}{P_{Fuel}} = \frac{P_B \eta_T}{P_{IN}} = \frac{P_B \eta_T}{P_B + P_F} = \frac{\eta_T}{(1+\frac{P_F}{P_B})} = \frac{\eta_T}{(1+\frac{fmep}{bmep})} \qquad (4.8)$$

$$\dot{m}_{Fuel} = \frac{Q\Omega_E}{\eta_T NCV}\left(1 + \frac{fmep}{bmep}\right) \qquad (4.9)$$

The friction mean effective pressure is difficult to model mathematically and this is where empirical data enters the model. References 18-21 suggest it can be described by a first or second order expansion of the engine angular velocity, Equation 4.10. The coefficients are not readily available and must be found from test data or perhaps a higher fidelity simulation.

$$\dot{m}_{Fuel} = \frac{Q\Omega_E}{\eta_T NCV}\left(1 + \frac{fmep}{bmep}\right) \tag{4.9}$$

$$fmep = A_0 + A_1\Omega_E + A_2\Omega_E^2 \tag{4.10}$$

Substituting $fmep$ from above and $bmep$ from Equation 4.1, the fuel mass flow rate becomes:

$$\dot{m}_{Fuel} = \frac{Q\Omega_E}{\eta_T NCV}\left(1 + \frac{A_0+A_1\Omega_E+A_2\Omega_E^2}{\frac{2\pi Q n_C}{V_S}}\right) \tag{4.11}$$

The indicated thermal efficiency, η_T, is another parameter which is difficult to predict and where empirical data enters the model. Reference 21 suggests it can be described as a mean efficiency divided by a torque and angular velocity variation functions, Equation 4.12. Equation 4.12 can then be substituted into Equation 4.11 to result in Equation 4.13

$$\eta_T = \frac{\eta_{T0}}{1+fg} \tag{4.12}$$

$$\dot{m}_{Fuel} = \frac{Q\Omega_E}{\eta_{T0} NCV}\left(1 + \frac{A_0+A_1\Omega_E+A_2\Omega_E^2}{\frac{2\pi Q n_C}{V_S}}\right)(1+fg) \tag{4.13}$$

The function f is best described by a 2nd order polynomial of torque, per Equation 4.14. The function g is best described by a 4th order polynomial of angular velocity, per Equation 4.15. These are the phenomenological components of the model.

$$f = b_0 + +b_2 Q + b_3 Q^2 \tag{4.14}$$

$$g = c_0 + c_1\Omega_E + c_2{\Omega_E}^2 + c_3{\Omega_E}^3 + c_4{\Omega_E}^4 \tag{4.15}$$

As a result, variations with respect to torque and engine speed can be approximated with the 4th order form of fg, Equation 4.16.

$$fg = B_0 + B_1\Omega_E + B_2Q + B_3{\Omega_E}^2 + B_4\Omega_EQ + B_5Q^2 + B_6{\Omega_E}^3 + B_7{\Omega_E}^2Q + B_8\Omega_EQ^2 + B_9{\Omega_E}^4 + B_{10}{\Omega_E}^3Q + B_{11}{\Omega_E}^2Q^2 \quad (4.16)$$

For a constant RPM, indicated thermal efficiency is low at idle (near-zero) to low torques as the output power is approximately zero. The indicated thermal efficiency peaks at cruise torques and then decreases when approaching maximum torque due to increased fuel-air ratios and combustion durations. For a constant torque, low RPM increases the cycle time, which can increase heat losses, decreasing indicated thermal efficiency. At a high RPM, the indicated thermal efficiency can again decrease due to the shorter combustion period resulting in unburnt fuel. Scavenging efficiency, a measure of fresh air drawn into the cylinder, also decreases at higher RPM, resulting in less clean air for combustion further decreasing the indicated thermal efficiency.

For torques between idle and cruise torque, there is an RPM range in which the indicated thermal efficiency is approximately constant with respect to RPM. In this range, fg approaches zero and Equation 4.13 can be reduced to four unknown constants: A_0, A_1, A_2 and $\eta_{T,0}$. These constants in Equation 4.13 can then be found with measured fuel consumption in the aforementioned torque and RPM range. The remaining unknowns, B_0 to B_{11}, can be solved with experimental data from the full operational torque and RPM range.

The brake specific fuel consumption, $bsfc$ (kg/W·s), is given by Equation 4.17. This model only predicts the steady-state, $bsfc$, a transient model will require transient fuel flow data to calibrate the thermal efficiencies.

$$bsfc = \frac{\dot{m}_{Fuel}}{P_B} \quad (4.17)$$

4.3. Calibration of Constants and Validation

The goal of the fuel consumption model is to predict the fuel efficiency of the engine at various engine torques and speeds. The fuel efficiency of the engine was measured as brake specific fuel consumption in kg/kW-hr. The engine model contains 19 constants. The number of output revolutions per piston cycle and cylinder swept volume are specified by the manufacturer (alternatively they could be measured for a specific engine). The net calorific value of the fuel is also known. For torques less than 50% maximum continuous torque and engine speeds between 5,500 and 7,500 RPM, $1 + fg \approx 1$. A_0, A_1, A_2, and $\eta_{T,0}$ were calculated from empirical data in that range using Equation 4.13. The predicted fuel efficiency contours of the engine as a function of engine torque and RPM are shown in Figure 4.3. Clearly, it does not adequately model fuel efficiency trends. Therefore, $B_{0\text{-}11}$ were then calculated from the full empirical data set using Equations 4.13 and 4.16.

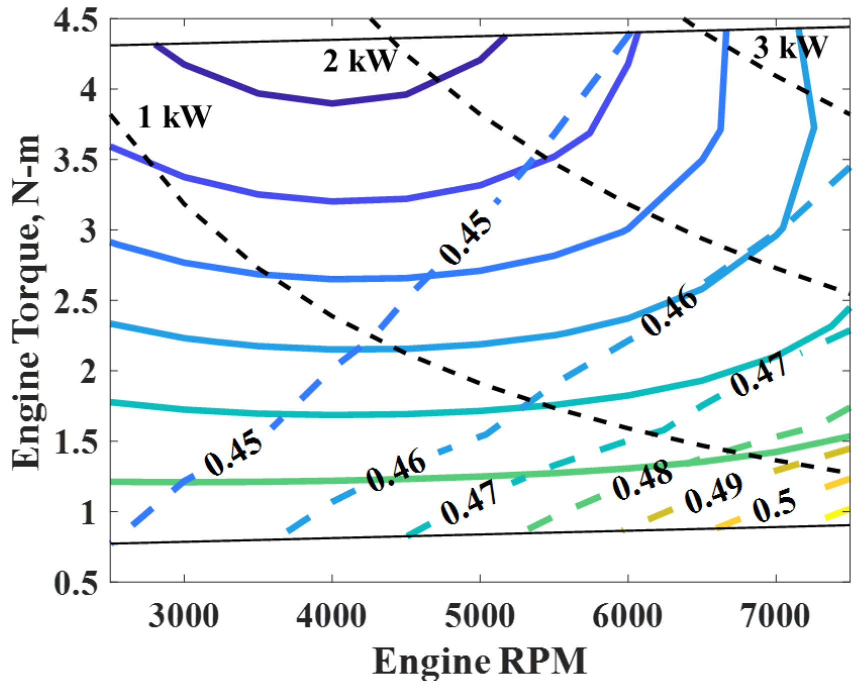

Figure 4.3. Engine torque versus RPM with predicted (dotted) and measured (solid) specific fuel consumption contours (kg/kW-hr) and constant power curves with only four constants: A_0, A_1, A_2 and $\eta_{T,0}$

The predicted fuel efficiency contours of the engine with all constants are shown in Figure 4.4. The predicted $bsfc$ contours (dotted) are overlaid on the experimental $bsfc$ contours (solid). Now the trends are adequately captured. For a specified power, predicted $bsfc$ is lower (i.e., engine is more fuel efficient) at higher torques and lower RPM. Figure 4.5 plots the same fuel efficiency as a function of power. The predicted fuel efficiency with constant torque (dotted) and RPM lines (dash-dot) are overlaid on the experimental, with constant torque (dashed) and RPM lines (solid). The trends and magnitudes remain consistent between the experimental and predicted $bsfc$. The largest predicted $bsfc$ errors (~2 %) are at the lower torque boundary and the upper RPM boundary.

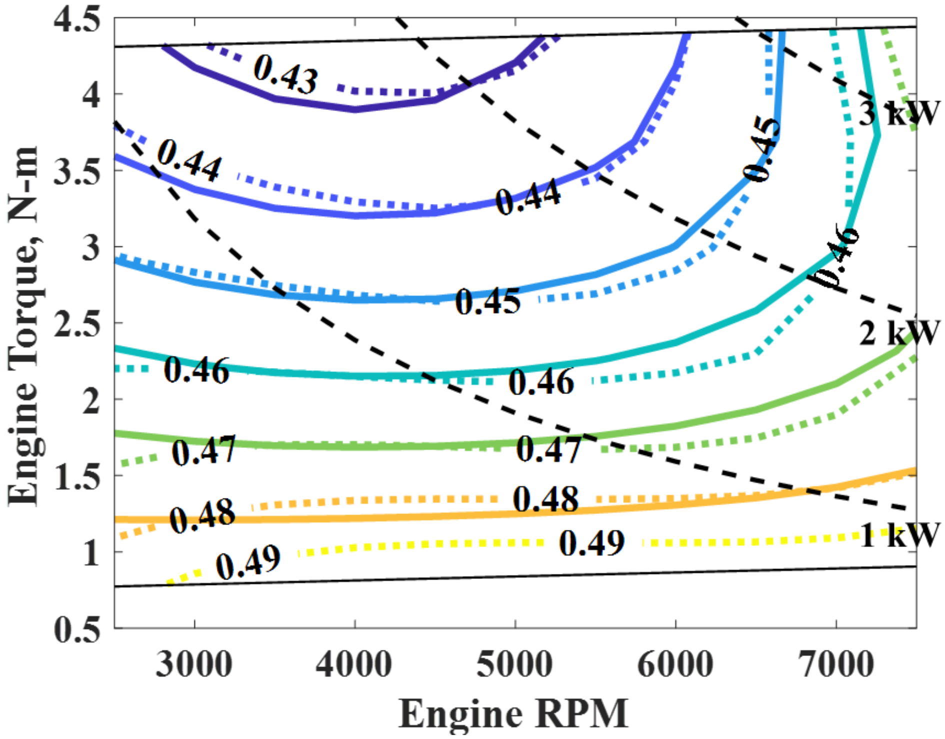

Figure 4.4. Engine torque versus RPM with predicted (dotted) and measured (solid) specific fuel consumption contours (kg/kW-hr) and constant power curves

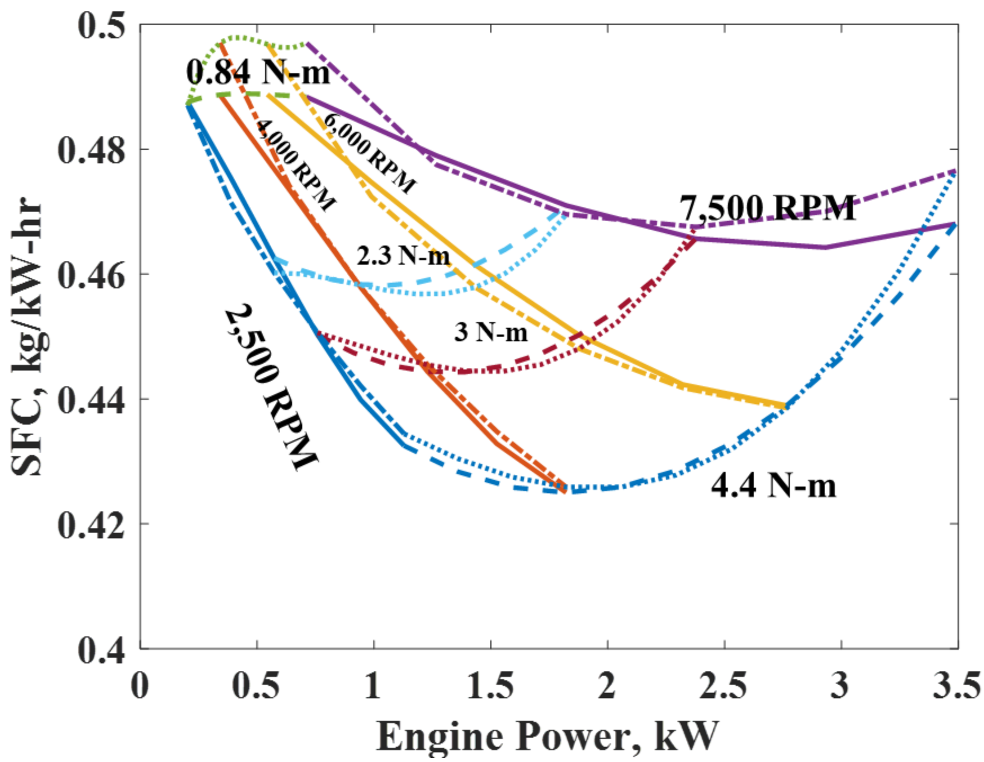

Figure 4.5. Engine specific fuel consumption versus power with predicted (dotted, dash-dot) and measured (solid, dashed) constant RPM and torque contours

4.4. Weight Model

A weight model is needed for conceptual design that varies with power. Reciprocating engines can have two- or four-stroke piston cycles that utilize gasoline-, diesel-, or kerosene-based fuels. As such a topological engine weight model is difficult given the significant differences in design features based on fuel and stroke number. One of the most significant designed features is the engine core material. Engines below 30 kW power almost exclusively use aluminum cores compared to the iron/steel cores used at higher powers. A curve fit of 72 commercial engines from 2 kW to 280 kW is given in Equation 4.18. Equation 4.18 accounts for the core material difference for engines below 30 kW. The average error is 30%. Figure 4.6 shows the engine weight, W in kg, as a function of maximum continuous power, P in kW, with dashed lines indicating 20% error.

$$\begin{cases} W = 0.2860\ P^{1.3015}, P \leq 30\ kW \\ W = 1.1012\ P^{0.9785}, P > 30\ kW \end{cases} \tag{4.18}$$

4.5. Chapter Summary and Conclusions

In this chapter, a fuel consumption model and weight model were developed for a reciprocating engine. It was found unsteady gas dynamics and transient thermodynamic effects are required to model the engine in detail. These effects can be captured by a simple physic-based model of bsfc contours if the thermal efficiency is calibrated with experimental data. After calibration the predicted bsfc error was largest (~2%) at the engine lower torque boundary and the upper RPM boundary. A weight versus power trend was found with 72 commercial engines, with an average error of 20%. It was found that when reciprocating engines are examined as a whole (i.e., 2-stroke, 4-stroke, diesel, gasoline), the engine core material can significantly affect the weight trends.

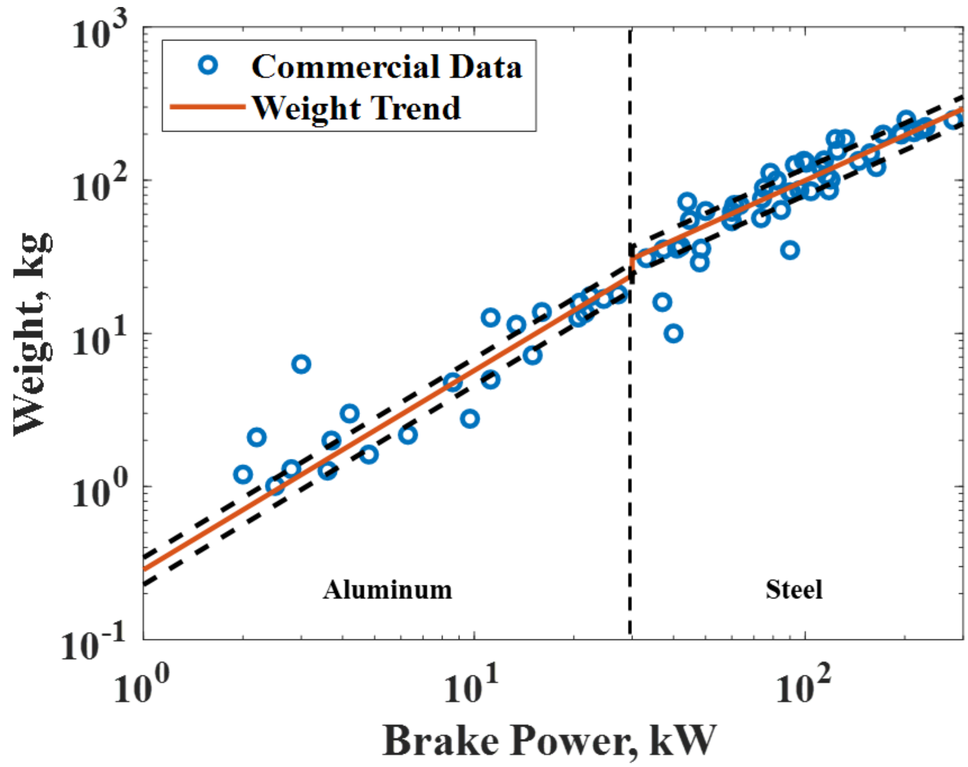

Figure 4.6. Engine weight verses brake power with predicted weight trends and 20% error boundaries for 72 engines

Chapter 5: AC Permanent Magnet Motor and Generator Model

This chapter develops models for predicting motor/generator performance and weight for the design of a hybrid-electric aircraft.

5.1. Introduction

Alternating-current, permanent-magnet, synchronous (AC PMS) motors and generators are typically used for electric aircraft as they have the highest specific power due to the low weight of the permanent magnet rotor. A PMS motor operates by exciting the poles of the stator armature in a rotating pattern with an alternating current, typically from a DC-fed inverter, producing a rotating magnetic field. The permanent magnet rotor interacts and aligns (or locks) with the rotating magnetic field causing the rotor to move. Once the rotor locks with the rotation of the stator magnetic field, the motor is said to be synchronized. To keep the motor rotating, current in the stator windings must reverse polarity every time a rotor magnet (pole) passes by this is called commutation. The frequency of this reversal is the frequency of the AC electrical field. AC PMS motors can be grouped based on the back electromotive force (EMF) induced in the stator windings. The two main types of EMF are trapezoidal and sinusoidal. Trapezoidal motors have a concentrated stator winding that creates a trapezoid-shaped back-EMF. While sinusoidal motors have a distributed stator winding that creates a smooth sinusoidal-shaped back-EMF. Trapezoidal motor outputs appear identical to a classical DC motor with brushes to revers polarity mechanically, hence these are also called “brushless” DC motors.

In this research, we will focus on a configuration where the rotor rotates around an interior stator commonly referred to as outrunner motors. The performance analysis is applicable to all configurations of the brushless DC motors. The detailed weight model is built for the outrunner configuration.

5.2. Three-Phase AC PMS Performance Model

AC PMS motors are typically powered with a DC supply. The DC voltage is fed into a six-step inverter to generate a three-phase AC source. The inverter, commonly referred to as an electronic speed controller (ESC), uses metal–oxide–semiconductor field-effect transistor (MOSFET) bridges to generate the 3-phase trapezoidal waveforms. In addition, it modulates voltage duty cycle to regulate motor speed. The ESC and the motor circuit diagram is shown in Figure 5.1. The MOSFET switches Q1, Q3, and Q5 to regulate the positive phase of the stator while switches Q2, Q4, and Q6 regulate the negative phase. Each switch is coupled to a freewheeling diode, D1-D6, to dissipate energy stored in the inductive windings when the phase is switched off. This is a basic textbook model, see for example Ref. [22].

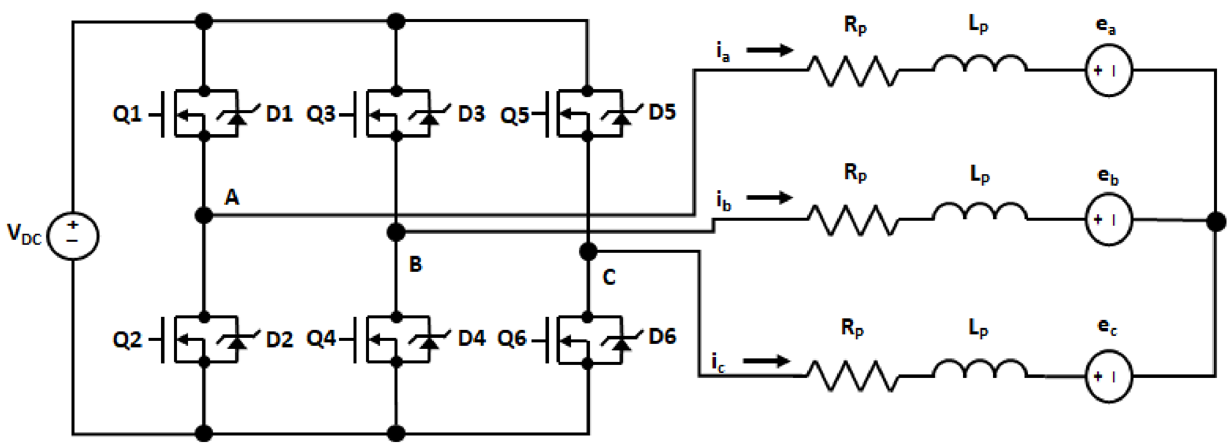

Figure 5.1. DC-fed motor with six-step inverter

The individual phase shown in Figure 5.2, is described by Equation 5.1.

$$V_n = R_p i_n + L_p \frac{di_n}{dt} + e_n \tag{5.1}$$

Where n is the phase (a, b, and c for a three-phase motor), V_n (V) is the phase voltage, and i_n (A) is the phase current. The phase resistance, R_p (Ohm), is function of the wire diameter and the total length of wire used in the phase winding. The phase inductance, L_p (H), is sum of the self- and mutual-inductance cause by the airgap flux, slot-leakage flux, and end-winding flux. The phase back-EMF, e_n (V), is the voltage induced in the stator winding due to its relative motion with the rotating magnets.

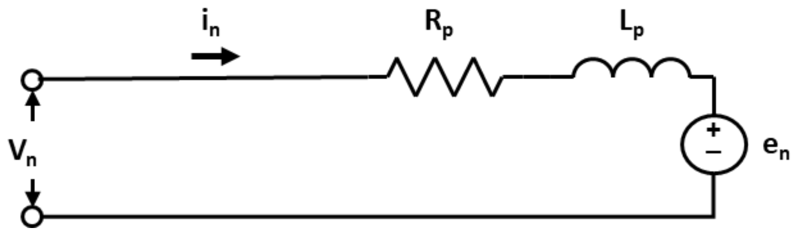

Figure 5.2. Circuit Diagram for an individual phase of a DC-fed motor

If the phases are connected in a Wye formation, then assuming the phase properties are identical, the phase-to-phase voltages are the difference of the individual phases, as described by Equations 5.2 -5.4

$$V_{ab} = R_p(i_a - i_b) + L_p \frac{d(i_a - i_b)}{dt} + e_a - e_b \tag{5.2}$$

$$V_{bc} = R_p(i_b - i_c) + L_p \frac{d(i_b - i_c)}{dt} + e_b - e_c \tag{5.3}$$

$$V_{ca} = R_p(i_c - i_a) + L_p \frac{d(i_c - i_a)}{dt} + e_c - e_a \tag{5.4}$$

The back-EMF is described by the Equations 5.5. to 5.7 for a three-phase motor.

$$e_a = k_{e,p} \Omega_m F_{(\theta_e)} \tag{5.5}$$

$$e_b = k_{e,p} \Omega_m F_{\left(\theta_e - \frac{2\pi}{3}\right)} \tag{5.6}$$

$$e_c = k_{e,p} \Omega_m F_{\left(\theta_e - \frac{4\pi}{3}\right)} \tag{5.7}$$

Where $k_{e,p}$ (rad/V-s) is the per phase back-EMF constant, Ω_m(rad/s), is the motor angular velocity, and $F_{(\theta_e)}$ is the waveform function. The phase back-EMF waveforms are offset by 120°-electrical for a three-phase motor. The trapezoidal waveform function is described in Equation 5.8.

$$F_{(\theta_e)} = \begin{cases} 1 & 0 \leq \theta_e < \frac{2\pi}{3} \\ 1 - \frac{6}{\pi}\left(\theta_e - \frac{2\pi}{3}\right) & \frac{2\pi}{3} \leq \theta_e < \pi \\ -1 & \pi \leq \theta_e < \frac{5\pi}{3} \\ -1 + \frac{6}{\pi}\left(\theta_e - \frac{5\pi}{3}\right) & \frac{5\pi}{3} \leq \theta_e < 2\pi \end{cases} \tag{5.8}$$

The mechanical behavior of an electric motor is described by Equation 5.9.

$$\begin{cases} Q_e = k_f \Omega_m + J\frac{d\Omega_m}{dt} + Q_L \\ Q_e = \sum_{n=a}^{c} k_{t,p} i_n \end{cases} \tag{5.9}$$

Where Q_e (N-m) is the electromagnetic torque, k_f (N-m-s/rad) is the friction coefficient, J (kg/m^2) is the rotor/load inertia, and Q_L (N-m) is the load torque (i.e., output torque). The electromagnetic torque is the sum of the individual phase currents times the per phase torque constant, k_t (N-m/A).

In order to solve for the currents in Equations 5.2 to 5.4, three voltages are required. However, at the neutral node of the Wye circuit, the sum of the phase currents is zero due to Kirchhoff's current law. Therefore, the voltage Equations can be reduced to two Equations by substituting $i_c = -i_a - i_b$ into Equation 5.2 and 5.3 resulting in Equation 5.10 and 5.11.

$$V_{ab} = R_p(i_a - i_b) + L_p\frac{d(i_a - i_b)}{dt} + e_a - e_b \tag{5.10}$$

$$V_{bc} = R_p(i_a + 2i_b) + L_p\frac{d(i_a + 2i_b)}{dt} + e_b - e_c \tag{5.11}$$

For the purposes of this model, it is assumed that the motor properties (R_p, L_p, J, k_f, and $k_{t,p}$, $k_{e,p}$), Q_L, and the DC bus voltage are known. The voltages and back-EMFs are resolved in the inverter module while the motor module solves the phase currents, while Ω_m, and the mechanical angle, θ_m, are functions of time. The electrical angle is related to the mechanical angle by $\theta_e = \frac{poles}{2}\theta_m$. Equations 5.5 to 5.11 are used to obtain the state-space Equations 5.12 to 5.16.

$$\frac{di_a}{dt} + \frac{R_p}{L_p} i_a = \frac{2}{3L_p}(V_{ab} - e_a + e_b) + \frac{1}{3L_p}(V_{bc} - e_b + e_c) \tag{5.12}$$

$$\frac{di_b}{dt} + \frac{R_p}{L_p} i_b = \frac{-1}{3L_p}(V_{ab} - e_a + e_b) + \frac{1}{3L_p}(V_{bc} - e_b + e_c) \tag{5.13}$$

$$i_c = -i_a - i_b \tag{5.14}$$

$$\frac{d\Omega_m}{dt} + \frac{k_f}{J}\Omega_m = \frac{1}{J}\left(\sum_{n=a}^{c} k_{t,p} i_n F_{(\theta_e)_n} - Q_L\right) \tag{5.15}$$

$$\mathrm{m}\frac{d\theta_m}{dt} = \Omega_m \tag{5.16}$$

In order to solve Equations 5.12 to 5.16 for current, the quantities $(V_{ab} - e_a + e_b)$ and $(V_{bc} - e_b + e_c)$ must be known for each point in time. These quantities are a function of phase commutation and control logic switching which also vary with time.

5.2.1. Phase Commutation

In this model, a six-step inverter with MOSFET switches is used to provide the current commutation, Figure 5.1. In a six-step inverter, switching occurs every 1/6th of an AC waveform period to switch polarities for continued motor rotation. The inverter switches two phases ON and one phase OFF. The phase commutation occurs every 60 °-electrical. Table 5.1 and Figure 5.3 show the phase commutation sequences and circuit diagrams.

Assuming the motor is in operation with the switch **Q5** and **Q4** closed. At 0° electrical, switch **Q1** closes and switch **Q5** opens. This applies voltage to the **phase a** armature and cuts voltage to the **phase c** armature. Switch **Q4** remains closed from the previous sequence, so voltage remains applied to the **phase b** armature. Current flows from the DC bus through **Q1** into **phase a** and from the neutral point through **phase b**. Therefore i_a is positive and i_b is negative.

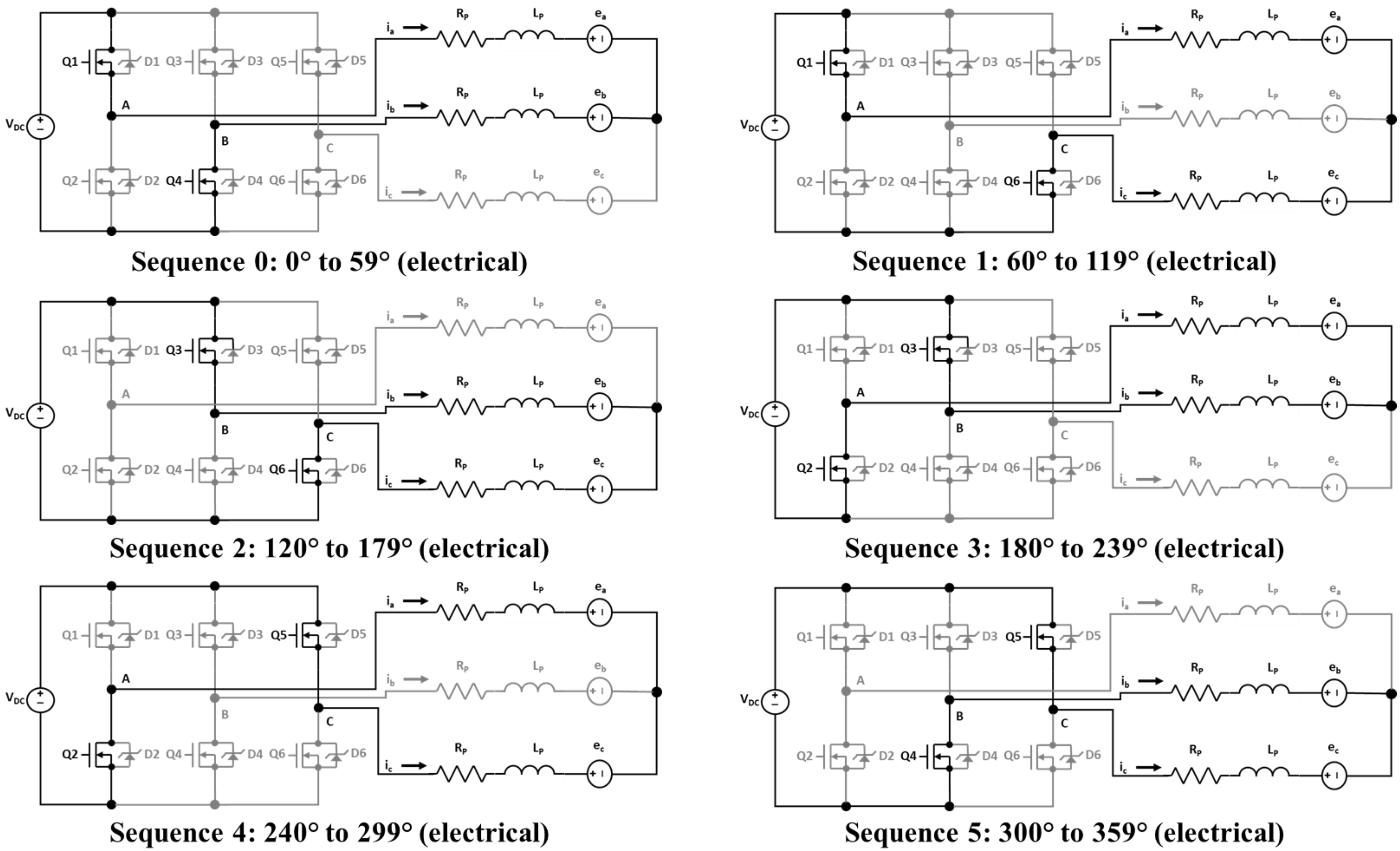

Sequence 0: 0° to 59° (electrical)

Sequence 1: 60° to 119° (electrical)

Sequence 2: 120° to 179° (electrical)

Sequence 3: 180° to 239° (electrical)

Sequence 4: 240° to 299° (electrical)

Sequence 5: 300° to 359° (electrical)

Figure 5.3. Circuit configurations for the phase commutation sequences

Table 5.1. Phase commutation sequence

Seq. #	Switching Interval, θ_e	Switches Closed		Phase Current		
				a	**b**	**c**
0	0° – 59°	Q1	Q4	+	-	Off
1	60° – 119°	Q1	Q6	+	Off	-
2	120° – 179°	Q3	Q6	Off	+	-
3	180° – 239°	Q3	Q2	-	+	Off
4	240° – 299°	Q5	Q2	-	Off	+
5	300° – 359°	Q5	Q4	Off	-	+

At 60° electrical, switch **Q6** closes and switch **Q4** opens. This applies voltage to the **phase c** armature and cuts voltage to the **phase b** armature. Switch **Q1** remains closed from the previous sequence, so voltage remains applied to the **phase a** armature. Current flows from the DC bus through **Q1** to the neutral point through **phase a** and from the neutral point through **phase c**. Therefore i_a is positive and i_c is negative.

At 120° electrical, switch **Q3** closes and switch **Q1** opens. This applies voltage to the phase B armature and de-energizes the **phase a** armature. Switch **Q6** remains closed from the previous sequence, so the **phase c** armature remains energized. Current flows from the DC bus through **Q3** into **phase b** and from the neutral point through **phase c**. Therefore i_b is positive and i_c is negative.

At 180° electrical, switch **Q2** closes and switch **Q6** opens. This applies voltage to the **phase a** armature and cuts voltage to the **phase c** armature. Switch **Q3** remains closed from the previous sequence, so voltage remains applied to the **phase b** armature. Current flows from the DC bus through **Q3** into **phase b** and from the neutral point through **phase a**. Therefore i_b is positive and i_a is negative.

At 240° electrical, switch **Q5** closes and switch **Q3** opens. This applies voltage to the **phase c** armature and cuts voltage to the **phase b** armature. Switch **Q2** remains closed from the previous sequence, so voltage remains applied to the **phase a** armature. Current flows from the DC bus through **Q5** into **phase c** and from the neutral point through **phase a**. Therefore i_c is positive and i_a is negative.

At 300° electrical, switch **Q4** closes and switch **Q2** opens. This applies voltage to the **phase b** armature and cuts voltage to the **phase a** armature. Switch **Q5** remains closed from the previous sequence, so voltage remains applied to the **phase c** armature. Current flows from the DC bus through **Q5** into **phase c** and from the neutral point through **phase b**. Therefore i_c is positive and i_b is negative [22].

Ideally, when the switches open and close during each phase commutation the currents would instantly rise and decay which would result in a ripple-free torque shown in Figure 5.4. However, the inductive windings of the phase armature store energy which must be dissipated when the phase is switched off. When a switch is closed, a resultant current flows through a freewheeling diode to dissipate energy of the inductive windings. This creates non-instantaneous current transients which results in current and torque ripples, as shown in Figure 5.5. Figure 5.6 shows the current paths for commutation for each sequence. The black current path is the current loop for the energized phases while the red current path is the current path for OFF phase with the freewheeling diode. Therefore, each phase commutation action has two available states:

1. The current of OFF phase is zero.
2. The current of the OFF phase is not zero.

When the freewheeling diode switches from a forward-conducting-bias to a reverse-bias in order to stop current flow, the diode has stored charge that must first be discharge before the diode blocks the reverse current. This is called reverse recovery. As a result, the OFF-phase current will briefly switch polarity prior to settling at zero. As a result, the freewheeling currents are bound using $i_n \geq 0$ for currents in which the reverse current is positive and $i_n \leq 0$ for currents in which the reverse current is negative to prevent the OFF phase from settling to a non-zero current.

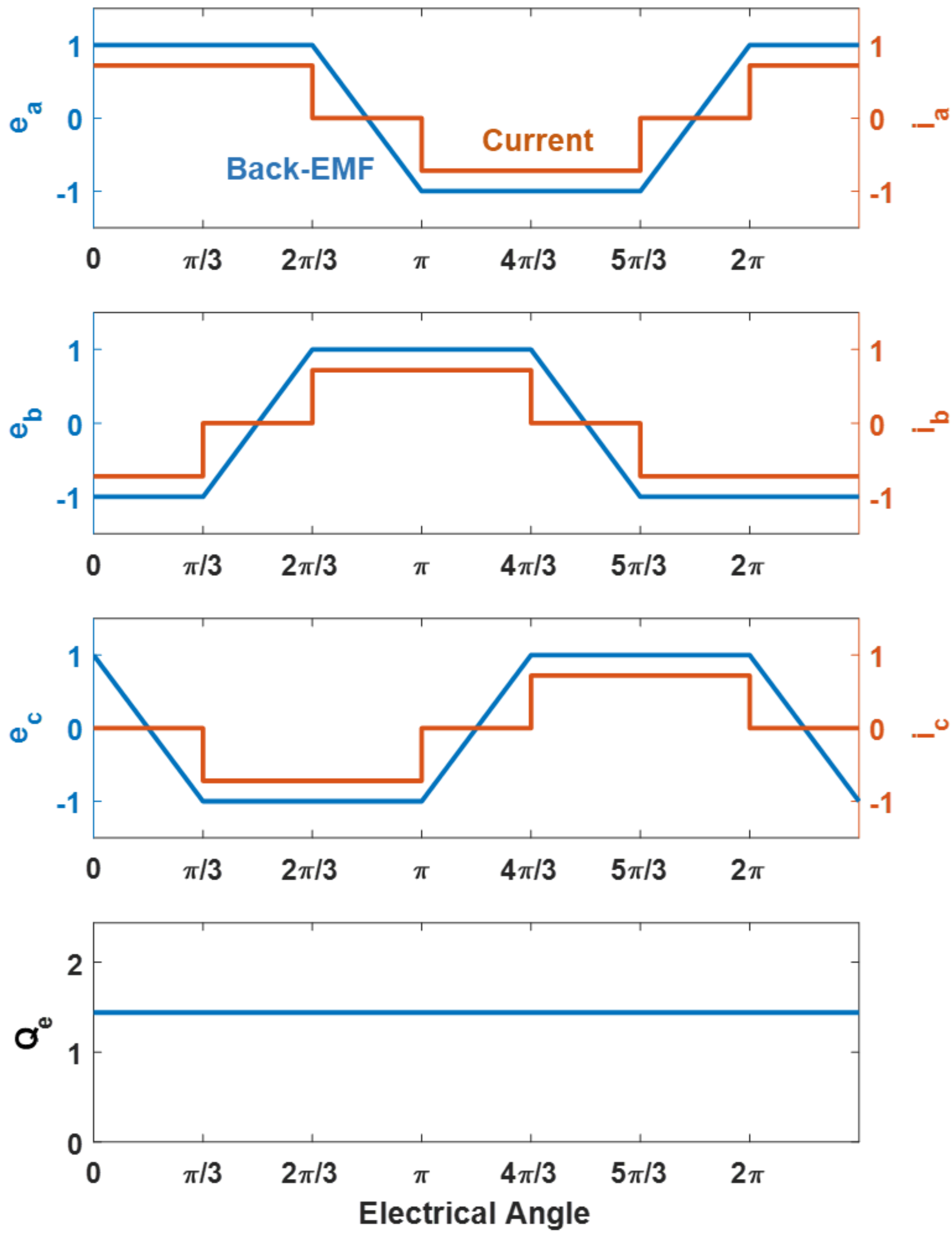

Figure 5.4. Back-EMF, phase current, and electromagnetic torque for an ideal (instantaneous) phase commutation

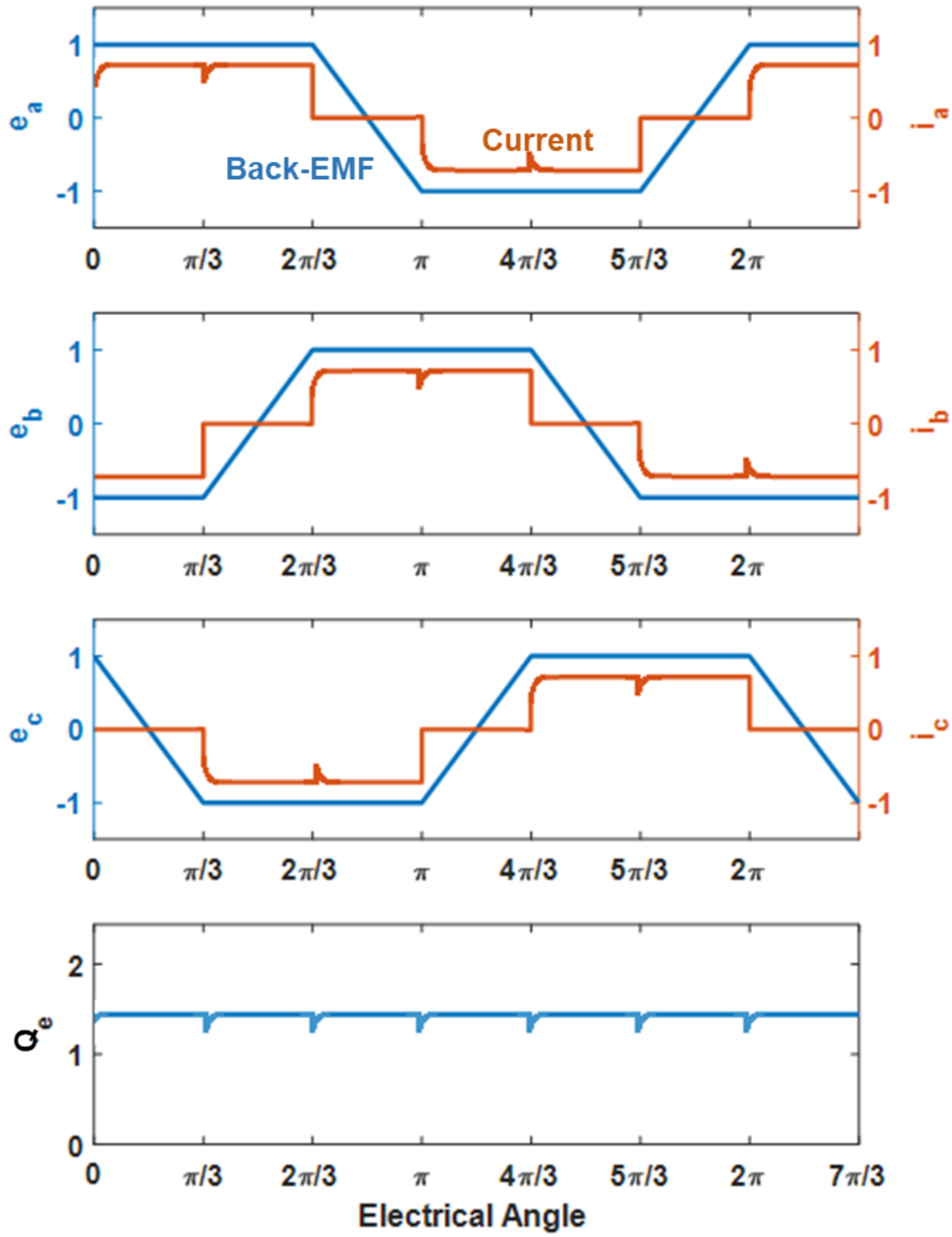

Figure 5.5. Back-EMF, phase current, and electromagnetic torque for a non-ideal (non-instantaneous) phase commutation

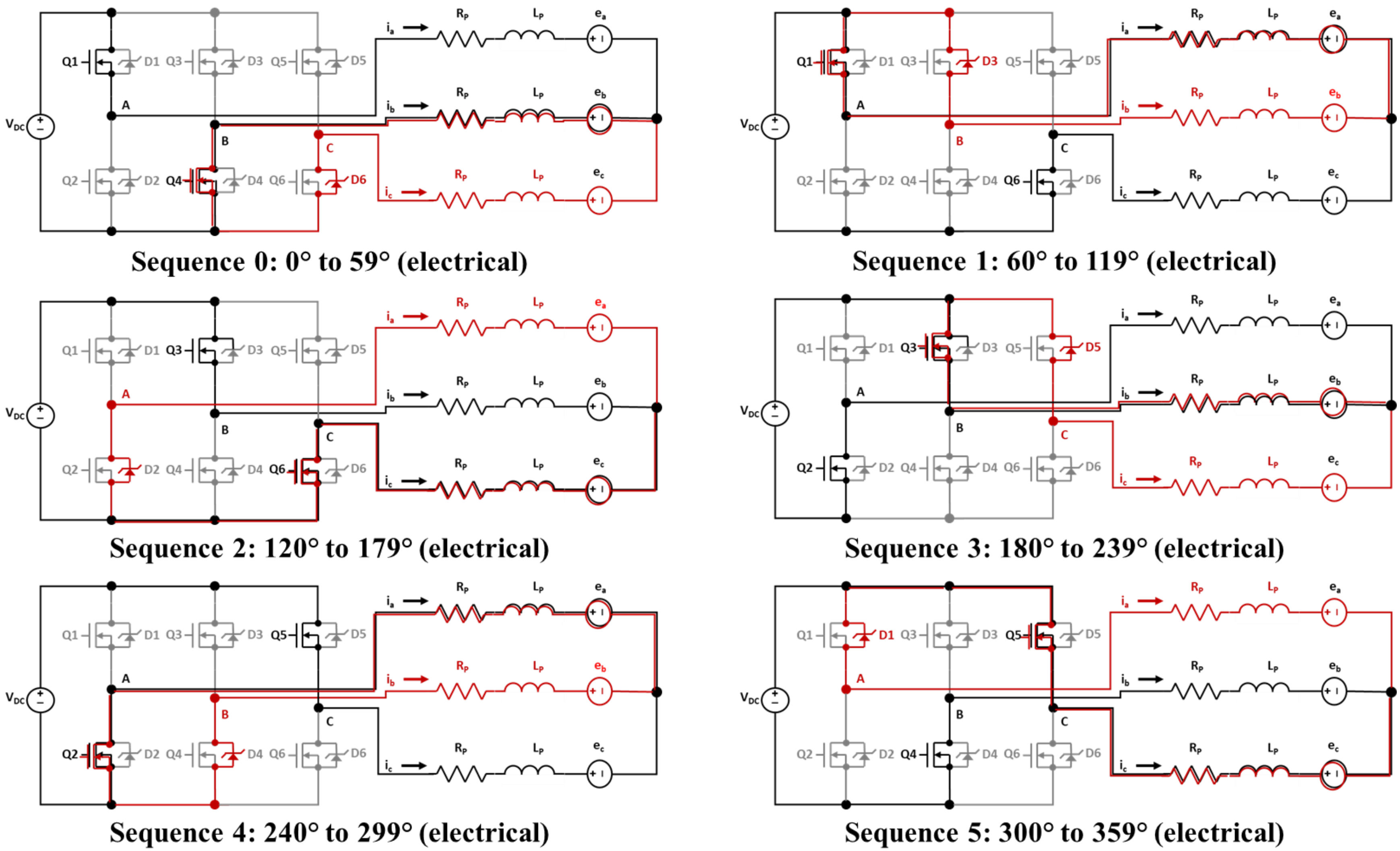

Figure 5.6. Circuit configurations for the phase commutation with a freewheeling diode

The circuit diagrams from Figure 5.6 can be redrawn as a two generic circuits with phases 1, 2, and 3 as shown in Figure 5.7 and Figure 5.8. Here Phase 1 is the positive phase, phase 2 is the negative phase, and phase three is OFF-phase of the phase sequences shown in Table 5.1. Here Z is the impedance of the circuit. The phase back-EMFs have been included as voltage sources along with the DC supply voltage, V_{DC}. The MOSFETs are assumed to be semi-ideal, as such are assumed to have a constant voltage drop, V_{MOS}, when current flows through them. Virtual voltage sources are included to represent the freewheeling diode. When the diode current is nonzero, it is assumed that V_{D3} is zero. When the diode current is zero, it is assumed that V_{D3} is nonzero. The voltages, V_{12}, V_{23}, and V_{31}, are solved for each state using Kirchhoff's current and voltage laws. The voltage, V_{12}, V_{23}, and V_{31}, can then be replaced with V_{ab}, V_{bc}, and V_{ca} in accordance with the phase commutation states detailed in Table 5.1 for each sequence.

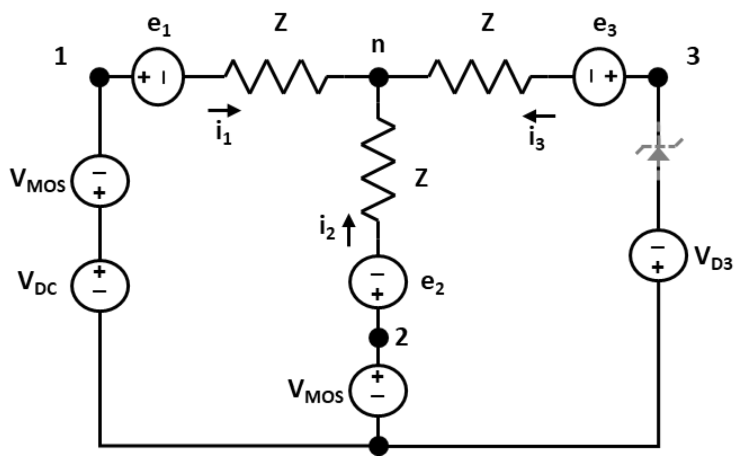

Figure 5.7. Generic freewheeling circuits for phase commutation for sequences 0, 2, and 4

For the circuit Figure 5.7, the voltages, V_{12}, V_{23}, and V_{31}, are found by summing the voltage drops and additions from point to point, Equation 5.17 to 5.19

$$V_{12} = e_1 - e_2 + Z(i_1 - i_2) \tag{5.17}$$

$$V_{23} = e_2 - e_3 + Z(i_2 - i_3) \tag{5.18}$$

$$V_{31} = e_3 - e_1 + Z(i_3 - i_1) \tag{5.19}$$

According to Kirchhoff's current law, the principle of conversation of electric charge implies that the sum of current flowing into a node equals the sum of currents flowing out of the node. Therefore, at node n $i_1 + i_2 + i_3 = 0$. According to Kirchhoff's voltage law, the principle of conservation of energy implies that the sum of voltages around any closed network is zero. The circuit has three such closed voltage networks, Equations 5.20 to 5.22.

$$V_{12} - V_{DC} + 2V_{MOS} = 0 \tag{5.20}$$

$$V_{23} - V_{D3} - V_{MOS} = 0 \tag{5.21}$$

$$V_{31} + V_{D3} + V_{DC} - V_{MOS} = 0 \tag{5.22}$$

For state 1, where $i_3 \neq 0$, $V_{D3} = 0$ is substituted in the voltage equations, Equation 5.20 to 5.22, to result in Equations 5.23 to 5.25

$$V_{12} = V_{DC} - 2V_{MOS} \tag{5.23}$$

$$V_{23} = V_{MOS} \tag{5.24}$$

$$V_{31} = -V_{DC} + V_{MOS} \tag{5.25}$$

In the end, we are interested in the sum of the phase-to-phase voltage and the phase back-EMFs, shown in Equation 5.26 to 5.28. So, the final step is to replace 1, 2, and 3 with the appropriate phase a, b, or c in accordance with Table 5.1 for sequences 0, 2, and 4. For example in sequence 2, phase a is the OFF phase, phase b is the positive phase, phase c is the negative phase. Therefore, for sequence 2, $V_{12} = V_{bc}$, $V_{23} = V_{ca}$, and $V_{31} = V_{ab}$.

$$V_{12} - e_1 + e_2 = V_{DC} - 2V_{MOS} - e_1 + e_2 \tag{5.26}$$

$$V_{23} - e_2 + e_3 = V_{MOS} - e_2 + e_3 \tag{5.27}$$

$$V_{31} - e_3 + e_1 = -V_{DC} + V_{MOS} - e_3 + e_1 \tag{5.28}$$

For the state 2, where $i_3 = 0$, Kirchhoff's current law at node n, results in $i_1 = -i_2$. This and Equation 5.17 are substituted into Equation 5.20 and then solved for current resulting in Equation 5.29.

$$i_1 = \frac{V_{DC} - 2V_{MOS} - e_1 + e_2}{2Z} \tag{5.29}$$

V_{23}, and V_{31} are then found by substituting Equation 5.29 into Equations 5.18 and 5.19 to form Equation 5.30 and 5.31.

$$V_{23} = \frac{-V_{DC} + 2V_{MOS} + e_2 + e_1}{2} - e_3 \tag{5.30}$$

$$V_{31} = \frac{-V_{DC} + 2V_{MOS} - e_1 - e_2}{2} + e_3 \tag{5.31}$$

As previously stated, we are interested in the phase-to-phase voltage and the phase-to-phase back-EMF in order to solve the governing equations, shown in Equation 5.32 to 5.34. The final step is to replace 1, 2, and 3 with the appropriate phase a, b, or c in accordance with Table 5.1 for sequences 0, 2, and 4.

$$V_{12} - e_1 + e_2 = V_{DC} - 2V_{MOS} - e_1 + e_2 \tag{5.32}$$

$$V_{23} - e_2 + e_3 = \frac{-V_{DC} + 2V_{MOS} + e_1 - e_2}{2} \tag{5.33}$$

$$V_{31} - e_3 + e_1 = \frac{-V_{DC} + 2V_{MOS} + e_1 - e_2}{2} \tag{5.34}$$

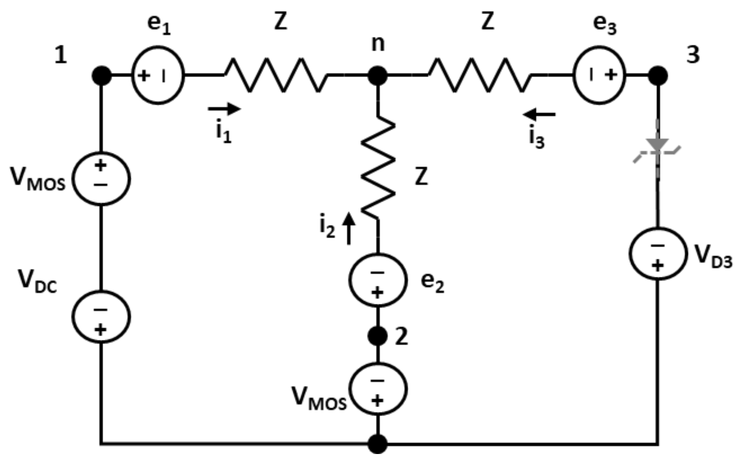

Figure 5.8. Generic freewheeling circuits for phase commutation for sequences 1, 3, and 5

Next, we repeat the same process for the circuit in Figure 5.8. The voltages, V_{12}, V_{23}, and V_{31}, found by summing the voltage drops/additions from point to point are still Equation 5.17 to 5.19. Here phase 1 is the negative phase, phase 2 is the positive phase, and phase three is OFF-phase of the phase sequences shown in Table 5.1. The circuit has three closed voltage networks, Equations 5.35-5.37:

$$V_{12} + V_{DC} - 2V_{MOS} = 0 \tag{5.35}$$

$$V_{23} - V_{D3} + V_{MOS} = 0 \tag{5.36}$$

$$V_{31} + V_{D3} - V_{DC} + V_{MOS} = 0 \tag{5.37}$$

For state 1, where $i_3 \neq 0$, $V_{D3} = 0$ is substituted in the voltage equations, Equations 5.35-5.37, to result in Equations 5.38-5.40.

$$V_{12} = -V_{DC} + 2V_{MOS} \tag{5.38}$$

$$V_{23} = -V_{MOS} \tag{5.39}$$

$$V_{31} = V_{DC} - V_{MOS} \tag{5.40}$$

As with the previous circuit, we are interested in the phase-to-phase voltage and the phase-to-phase back-EMF, shown in Equations 5.41-5.43. The final step is to replace 1, 2, and 3 with the appropriate phase a, b, or c in accordance with Table 5.1 for sequences 1, 3, and 5.

$$V_{12} - e_1 + e_2 = -V_{DC} + 2V_{MOS} - e_1 + e_2 \tag{5.41}$$

$$V_{23} - e_2 + e_3 = -V_{MOS} - e_2 + e_3 \tag{5.42}$$

$$V_{31} - e_3 + e_1 = V_{DC} - V_{MOS} - e_3 + e_1 \tag{5.43}$$

For state 2, where $i_3 = 0$, Kirchhoff's current law at node n, results in $i_1 = -i_2$. This and Equation 5.17 is substituted into Equation 5.35 and then solved for current resulting in Equation 5.44. V_{23}, and V_{31} are then found by substituting Equation 5.44 into Equations 5.18 and 5.19 to form Equations 5.45 and 5.46

$$i_1 = \frac{-V_{DC}+2V_{MOS}-e_1+e_2}{2Z} \tag{5.44}$$

$$V_{23} = \frac{V_{DC}-2V_{MOS}+e_1+e_2}{2} - e_3 \tag{5.45}$$

$$V_{31} = \frac{V_{DC}-2V_{MOS}-e_1-e_2}{2} + e_3 \tag{5.46}$$

As previously stated, we are interested in the phase-to-phase voltage and the phase-to-phase back-EMF in order to solve the governing equations, shown in Equations 5.47 to 5.49. The final step is to replace 1, 2, and 3 with the appropriate phase a, b, or c in accordance with Table 5.1 for sequences 1, 3, and 5.

$$V_{12} - e_1 + e_2 = -V_{DC} + 2V_{MOS} - e_1 + e_2 \tag{5.47}$$

$$V_{23} - e_2 + e_3 = \frac{V_{DC}-2V_{MOS}+e_1-e_2}{2} \tag{5.48}$$

$$V_{31} - e_3 + e_1 = \frac{V_{DC}-2V_{MOS}+e_1-e_2}{2} \tag{5.49}$$

Table 5.2 shows the calculated voltages required to solve Equations 5.12 and 5.13 as a function of electrical angle. The inverter module then calls the appropriate voltage as a function of

Table 5.2. Inverter output for phase commutation (Energized phase on, no chopping)

Seq #	**Phase Current**	**V_{ab}-e_a+e_b**	**V_{bc}-e_b+e_c**
0	$i_c \neq 0$	$V_{DC} - 2V_{MOS} - e_a + e_b$	$V_{MOS} - e_b + e_c$
	$i_c = 0$	$V_{DC} - 2V_{MOS} - e_a + e_b$	$½(-V_{DC} + 2V_{MOS} + e_a - e_b)$
1	$i_b \neq 0$	$-V_{MOS} - e_a + e_b$	$V_{DC} - V_{MOS} - e_b + e_c$
	$i_b = 0$	$½(V_{DC} - 2V_{MOS} - e_a + e_c)$	$½(V_{DC} - 2V_{MOS} - e_a + e_c)$
2	$i_a \neq 0$	$-V_{DC} + 2V_{MOS} - e_a + e_b$	$V_{DC} - 2V_{MOS} - e_b + e_c$
	$i_a = 0$	$½(-V_{DC} + 2V_{MOS} + e_b - e_c)$	$V_{DC} - 2V_{MOS} - e_b + e_c$
3	$i_c \neq 0$	$-V_{DC} + 2V_{MOS} - e_a + e_b$	$-V_{MOS} - e_b + e_c$
	$i_c = 0$	$-V_{DC} + 2V_{MOS} - e_a + e_b$	$½(V_{DC} - 2V_{MOS} + e_a - e_b)$
4	$i_b \neq 0$	$V_{MOS} - e_a + e_b$	$-V_{DC} + V_{MOS} - e_b + e_c$
	$i_b = 0$	$½(-V_{DC} + 2V_{MOS} - e_a + e_c)$	$½(-V_{DC} + 2V_{MOS} - e_a + e_c)$
5	$i_a \neq 0$	$V_{DC} - V_{MOS} - e_a + e_b$	$-V_{DC} + 2V_{MOS} + e_a - e_b$
	$i_a = 0$	$½(V_{DC} - 2V_{MOS} + e_b - e_c)$	$-V_{DC} + 2V_{MOS} - e_b + e_c$

the electrical angle to solve the governing equations.

5.2.2. Control Logic Switching

With Table 5.2 and the governing Equations, 5.12 to 5.16, we can predict motor RPM and current as a function of specific DC bus voltage and the load torque. For a specified DC bus voltage, the motor RPM can be reduced (or controlled) by what is called the pulse-width modulation (PWM) of the phase voltages. PWM reduces the average voltage across the phases (V_{ab}, V_{bc}, V_{ca}) by switching the MOSFETs OFF and ON at a higher frequency than the phase commutation frequency. This switching is called chopping. To implement PWM control, two additional model inputs are required: PWM frequency and PWM duty cycle. PWM frequency is the number of control cycles per second. PWM duty cycle is the amount of time the signal is in an ON state as a percentage of the total time of it takes to complete one control cycle. For the results of this research, we used a control frequency of 20 kHz with a time proportioning PWM signal.

As previously stated, the switching of the MOSFETs OFF and ON as a result of the control logic is called chopping (i.e., the voltage is chopped into discrete proportions). There are two types of chopping used in motor controls: hard and soft chopping. Hard chopping is when the upper and lower switches are switched by the same control signal. Soft chopping is when only one switch is driven by the control signal and the other switch remains on. While soft chopping requires more complexity in the control system, it results in less current, and therefore less torque ripple. For the purposes of this research, we will utilize only soft chopping as low current ripples and less torque ripples are desired in aviation. Similar to the phase commutation switching, energy stored in the inductive windings must be dissipated during chopping. When a switch is closed, current flows through a freewheeling diode to dissipate energy of the inductive windings. This current does not decay instantaneously. Therefore, each soft chopping switching action has four available states:

1. The current of the OFF-phase is not zero and the current of the chopped ON-phases are not zero.
2. The current of the OFF-phase is zero and the current of the chopped ON-phases are not zero.
3. The current of the OFF-phase is not zero and the current of the chopped ON-phases are not zero.
4. The current of the OFF-phase is zero and the current of the chopped ON-phases are not zero.

As with the phase commutations, the phase-to-phase voltages and back-EMF must be solved for each state in order to solve the governing Equations. Figure 5.9 shows the circuit diagrams for the freewheeling diodes for each sequence. The black and red current paths are the current loops for the freewheeling diodes. The circuit diagrams from Figure 5.9 can be redrawn as a two generic circuits with phases 1, 2, and 3 as shown in Figure 5.10 and Figure 5.11. Phase 1 is the positive phase, phase 2 is the negative phase, and phase three is the OFF-phase in the phase sequence shown in Table 5.1. Here Z is the impedance of the circuit. The phase back-EMFs have been included as voltage sources along with the DC supply voltage, V_{DC}. The MOSFETs are assumed to be semi-ideal, as such are assumed to have a constant voltage drop, V_{MOS}, when current flows through them. Virtual voltage sources are included to represent the freewheeling diode. When the diode current is nonzero, it is assumed that V_{D3} is zero. When the diode current is zero, it is assumed that V_{D3} is nonzero. The voltages, V_{12}, V_{23}, and V_{31}, are solved for each state using

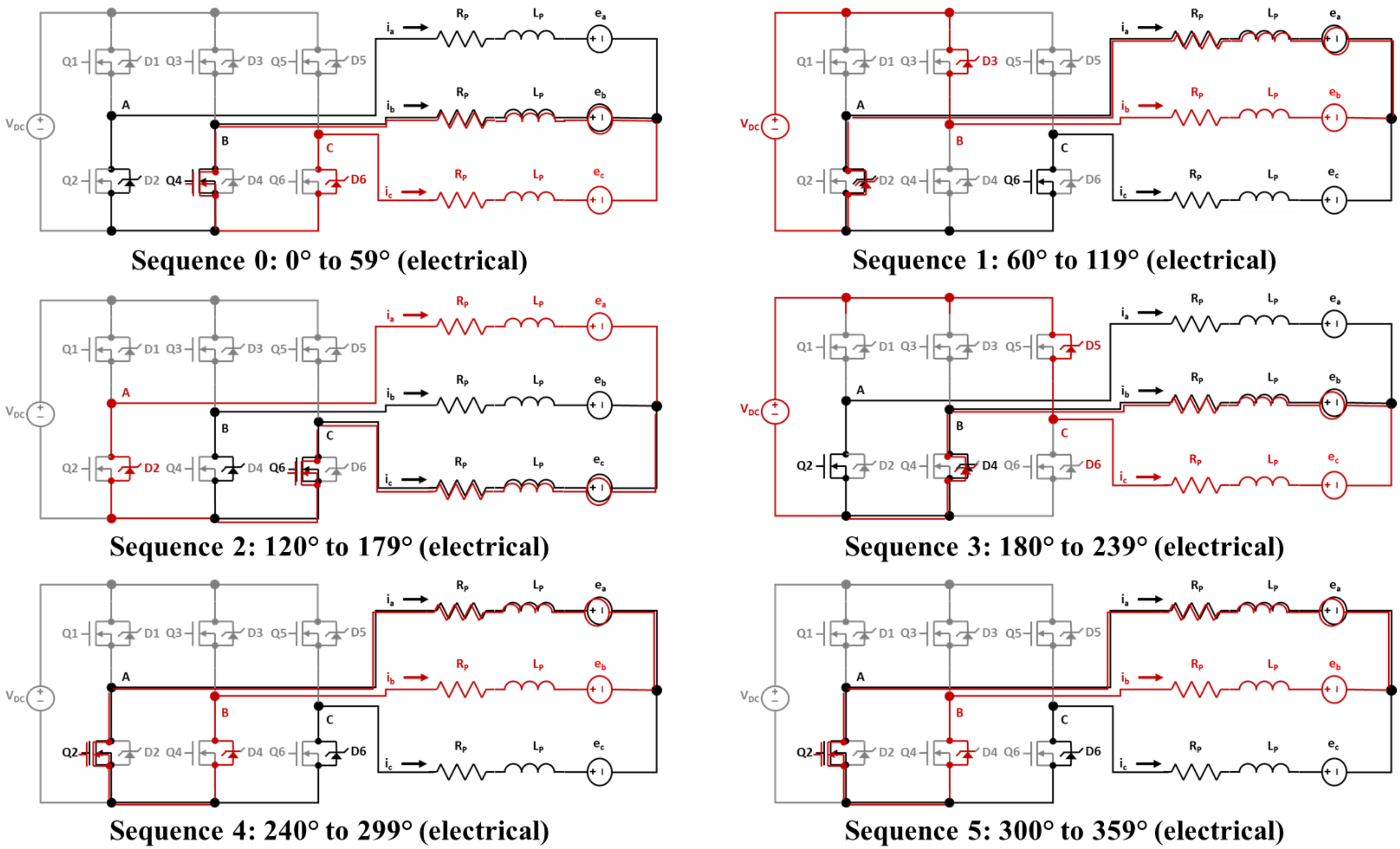

Figure 5.9. Circuit configurations for soft chopping with a freewheeling diode

Kirchhoff's current and voltage laws. The voltage, V_{12}, V_{23}, and V_{31}, can then be replaced with V_{ab}, V_{bc}, and V_{ca} in accordance with the phase states detailed in Table 5.1 for each sequence.

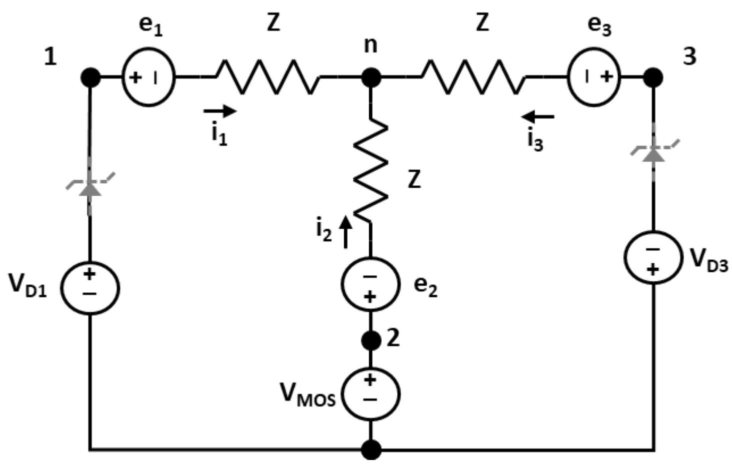

Figure 5.10. Generic freewheeling circuits for soft chopping for sequences 0, 2, and 4

For circuit in Figure 5.10, the voltages, V_{12}, V_{23}, and V_{31}, found by summing the voltage drops/additions from point to point are still Equation 5.17 to 5.19. According to Kirchhoff's current law, the principle of conversation of electric charge implies that the sum of current flowing into a node equals the sum of currents flowing out of the node. Therefore, at node n $i_1 + i_2 + i_3 = 0$. According to Kirchhoff's voltage law, the principle of conservation of energy implies that the sum

of voltages around any closed network is zero. This circuit has three such closed voltage networks, Equations 5.50 to 5.52:

$$V_{12} - V_{D1} + V_{MOS} = 0 \tag{5.50}$$

$$V_{23} - V_{D3} - V_{MOS} = 0 \tag{5.51}$$

$$V_{31} + V_{D3} + V_{D1} = 0 \tag{5.52}$$

For state 1, where $i_1 \neq 0$ and $i_3 \neq 0$, $V_{D1} = 0$ and $V_{D3} = 0$ is substituted in the voltage equations, Equations 5.50 to 5.52, to result in Equations 5.53 to 5.55.

$$V_{12} = -V_{MOS} \tag{5.53}$$

$$V_{23} = V_{MOS} \tag{5.54}$$

$$V_{31} = 0 \tag{5.55}$$

As before, we are interested in the phase-to-phase voltage and the phase-to-phase back-EMF in order to solve the governing Equations, shown in Equations 5.56 to 5.58. So, the final step is to replace 1, 2, and 3 with the appropriate phase a, b, or c in accordance with Table 5.1 for sequences 0, 2, and 4. For example in sequence 2, phase a is the OFF phase, phase b is the positive phase, phase c is the negative phase. Therefore, during sequence 2, $V_{12} = V_{bc}$, $V_{23} = V_{ca}$, and $V_{31} = V_{ab}$.

$$V_{12} - e_1 + e_2 = -V_{MOS} - e_1 + e_2 \tag{5.56}$$

$$V_{23} - e_2 + e_3 = V_{MOS} - e_2 + e_3 \tag{5.57}$$

$$V_{31} - e_3 + e_1 = -e_3 + e_1 \tag{5.58}$$

For state 2, where $i_1 \neq 0$ and $i_3 = 0$, Kirchhoff's current law at node n, results in $i_1 = -i_2$. This, Equation 5.19, and $V_{D1} = 0$ are substituted into Equation 5.50 and then solved for current resulting in Equation 5.59.

$$i_1 = \frac{-V_{MOS} - e_1 + e_2}{2Z} \tag{5.59}$$

V_{23}, and V_{31} are then found by substituting Equation 5.59 into Equations 5.60 and 5.61 to form Equation 83 and 84.

$$V_{23} = \frac{V_{MOS} + e_1 + e_2}{2} - e_3 \tag{5.60}$$

$$V_{31} = \frac{V_{MOS} - e_1 - e_2}{2} + e_3 \tag{5.61}$$

As with the phase commutation circuits, we are interested in the phase-to-phase voltage and the phase-to-phase back-EMF in order to solve the governing Equations in order, shown in Equations 5.62 to 5.64. The final step is to replace 1, 2, and 3 with the appropriate phase a, b, or c in accordance with Table 5.1 for sequences 0, 2, and 4

$$V_{12} - e_1 + e_2 = -V_{MOS} - e_1 + e_2 \tag{5.62}$$

$$V_{23} - e_2 + e_3 = \frac{V_{MOS}+e_1-e_2}{2} \tag{5.63}$$

$$V_{31} - e_3 + e_1 = \frac{V_{MOS}+e_1-e_2}{2} \tag{5.64}$$

For state 3, where $i_3 \neq 0$ and $i_1 = 0$, Kirchhoff's current law at node n, results in $i_3 = -i_2$. This, Equation 5.18, and $V_{D3} = 0$ are substituted into Equation 5.51 and then solved for current resulting in Equation 5.65.

$$i_3 = \frac{-V_{MOS}-e_3+e_2}{2Z} \tag{5.65}$$

V_{12}, and V_{31} are then found by substituting Equation 5.65 into Equations 5.17 and 5.19 resulting in Equations 5.66 and 5.67

$$V_{12} = \frac{-V_{MOS}-e_3-e_2}{2} + e_1 \tag{5.66}$$

$$V_{31} = \frac{-V_{MOS}+e_3+e_2}{2} - e_1 \tag{5.67}$$

As previously stated, we are interested in the phase-to-phase voltage and the phase-to-phase back-EMF in order to solve the governing Equations, shown in Equations 5.68 to 5.70. The final step is to replace 1, 2, and 3 with the appropriate phase a, b, or c in accordance with Table 5.1 for sequences 0, 2, and 4.

$$V_{12} - e_1 + e_2 = \frac{-V_{MOS}-e_3+e_2}{2} \tag{5.68}$$

$$V_{23} - e_2 + e_3 = V_{MOS} - e_2 + e_3 \tag{5.69}$$

$$V_{31} - e_3 + e_1 = \frac{-V_{MOS}-e_3+e_2}{2} \tag{5.70}$$

For state 4, where $i_3 = 0$ and $i_1 = 0$, Kirchhoff's current law at node n, results in $i_2 = 0$. The currents are substituted into Equations 5.17 to 5.19 to solved for the phase voltage, Equations 5.71 to 5.73.

$$V_{12} = e_1 - e_2 \tag{5.71}$$

$$V_{23} = e_2 - e_3 \tag{5.72}$$

$$V_{31} = e_3 - e_1 \tag{5.73}$$

As previously stated, we are interested in the phase-to-phase voltage and the phase-to-phase back-EMF in order to solve the governing Equations, shown in Equations 5.74 to 5.76. The final step is to replace 1, 2, and 3 with the appropriate phase a, b, or c in accordance with Table 5.1 for sequences 0, 2, and 4.

$$V_{12} - e_1 + e_2 = 0 \tag{5.74}$$

$$V_{23} - e_2 + e_3 = 0 \tag{5.75}$$

$$V_{31} - e_3 + e_1 = 0 \tag{5.76}$$

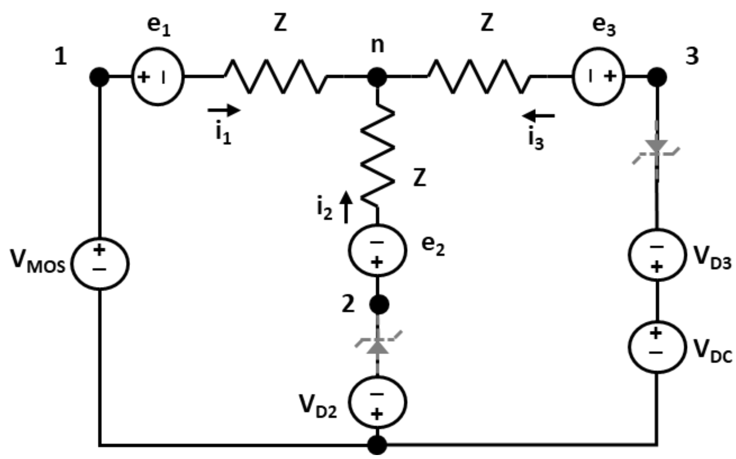

Figure 5.11. Generic freewheeling circuits for soft chopping for sequences 1, 3, and 5

For the circuit in Figure 5.11, the voltages, V_{12}, V_{23}, and V_{31},, are found by summing the voltage drops/additions from point to point, which results again in Equation 5.17 to 5.19. According to Kirchhoff's current law, the principle of conversation of electric charge implies that the sum of current flowing into a node equals the sum of currents flowing out of the node. Therefore, at node n, $i_1 + i_2 + i_3 = 0$. According to Kirchhoff's voltage law, the sum of voltages around any closed network is zero. The circuit has three such closed voltage networks, Equations 5.77 to 5.79.

$$V_{12} - V_{D2} - V_{MOS} = 0 \tag{5.77}$$

$$V_{23} - V_{D3} + V_{D2} + V_{DC} = 0 \tag{5.78}$$

$$V_{31} + V_{D3} - V_{DC} + V_{MOS} = 0 \tag{5.79}$$

For state 1, where $i_2 \neq 0$ and $i_3 \neq 0$, $V_{D2} = 0$ and $V_{D3} = 0$ is substituted in the voltage Equations, Equations 5.77 to 5.79, to result in Equations 5.80 to 5.82.

$$V_{12} = V_{MOS} \tag{5.80}$$

$$V_{23} = -V_{DC} \tag{5.81}$$

$$V_{31} = V_{DC} - V_{MOS} \tag{5.82}$$

As previously stated, we are interested in the phase-to-phase voltage and the phase-to-phase back-EMF in order to solve the governing Equations, shown in Equations 5.83 to 5.85. The final step is to replace 1, 2, and 3 with the appropriate phase a, b, or c in accordance with Table 5.1 for sequences 1, 3, and 5.

$$V_{12} - e_1 + e_2 = V_{MOS} - e_1 + e_2 \tag{5.83}$$

$$V_{23} - e_2 + e_3 = -V_{DC} - e_2 + e_3 \tag{5.84}$$

$$V_{31} - e_3 + e_1 = V_{DC} - V_{MOS} - e_3 + e_1 \tag{5.85}$$

For state 2, where $i_2 \neq 0$ and $i_3 = 0$, Kirchhoff's current law at node n, results in $i_1 = -i_2$. This, Equation 5.17, and $V_{D2} = 0$ are substituted into Equation 5.77 and then solved for current resulting in Equation 5.86.

$$i_2 = \frac{-V_{MOS} + e_1 - e_2}{2Z} \tag{5.86}$$

V_{23}, and V_{31} are then found by substituting Equation 5.86 into Equations 5.18 and 5.19 to form Equations 5.87 and 5.88.

$$V_{23} = \frac{-V_{MOS} + e_1 + e_2}{2} - e_3 \tag{5.87}$$

$$V_{31} = \frac{-V_{MOS} - e_1 - e_2}{2} + e_3 \tag{5.88}$$

As previously stated, we are interested in the phase-to-phase voltage and the phase-to-phase back-EMF in order to solve the governing Equations, shown in Equations 5.89 to 5.91. The final step is to replace 1, 2, and 3 with the appropriate phase a, b, or c in accordance with Table 5.1 for sequences 1, 3, and 5.

$$V_{12} - e_1 + e_2 = V_{MOS} - e_1 + e_2 \tag{5.89}$$

$$V_{23} - e_2 + e_3 = \frac{-V_{MOS}+e_1-e_2}{2} \tag{5.90}$$

$$V_{31} - e_3 + e_1 = \frac{-V_{MOS}+e_1-e_2}{2} \tag{5.91}$$

For state 3, where $i_2 = 0$ and $i_3 \neq 0$, Kirchhoff's current law at node n, results in $i_1 = -i_3$. This, Equation 5.19, and $V_{D3} = 0$ are substituted into Equation 5.79 and then solved for current resulting in Equation 5.92.

$$i_3 = \frac{V_{DC}-V_{MOS}+e_1-e_3}{2Z} \tag{5.92}$$

V_{12}, and V_{23} are then found by substituting Equation 5.92 into Equations 5.17 and 5.19 to form Equations 5.93 and 5.94.

$$V_{12} = \frac{e_3+e_1-V_{DC}+V_{MOS}}{2} + e_2 \tag{5.93}$$

$$V_{23} = \frac{-e_3-e_1-V_{DC}+V_{MOS}}{2} - e_2 \tag{5.94}$$

As previously stated, we are interested in the phase-to-phase voltage and the phase-to-phase back-EMF in order to solve the governing Equations, shown in Equations 5.95 to 5.97. The final step is to replace 1, 2, and 3 with the appropriate phase a, b, or c in accordance with Table 5.1 for sequences 1, 3, and 5.

$$V_{12} - e_1 + e_2 = \frac{e_3-e_1-V_{DC}+V_{MOS}}{2} \tag{5.95}$$

$$V_{23} - e_2 + e_3 = \frac{e_3-e_1-V_{DC}+V_{MOS}}{2} \tag{5.96}$$

$$V_{31} - e_3 + e_1 = V_{DC} - V_{MOS} - e_3 + e_1 \tag{5.97}$$

For state 4, where $i_2 = 0$ and $i_3 = 0$, Kirchhoff's current law at node n, results in $i_2 = 0$. The currents are substituted into Equations 5.17 to 5.19 then solved for the phase voltage which results in Equations 5.71 to 5.73. As previously stated, we are interested in the phase-to-phase voltage and the phase-to-phase back-EMF in order to solve the governing Equations, shown in Equations 5.74 to 5.76. The final step is to replace 1, 2, and 3 with the appropriate phase a, b, or c in accordance with Table 5.1 for sequences 1, 3, and 5. Table 5.3 shows the calculated voltages required to solve Equations 5.12 and 5.13 as a function of electrical angle.

Table 5.3. Inverter output for control commutation (Energized phase off, soft chopping)

Seq #	Phase Current	$V_{ab} - e_a + e_b$	$V_{bc} - e_b + e_c$
0	$i_a \neq 0, i_c \neq 0$	$-V_{MOS} - e_a + e_b$	$V_{MOS} - e_b + e_c$
	$i_a \neq 0, i_c = 0$	$-V_{MOS} - e_a + e_b$	$½ (V_{MOS} + e_a - e_b)$
	$i_a = 0, i_c \neq 0$	$½ (-V_{MOS} + e_b - e_c)$	$V_{MOS} - e_b + e_c$
	$i_a = 0, i_c = 0$	0	0
1	$i_a \neq 0, i_b \neq 0$	$-V_{DC} - e_a + e_b$	$V_{DC} - V_{MOS} - e_b + e_c$
	$i_a \neq 0, i_b = 0$	$½ (-V_{MOS} - e_a + e_c)$	$½ (-V_{MOS} - e_a + e_c)$
	$i_a = 0, i_b \neq 0$	$½ (-V_{DC} + V_{MOS} + e_b - e_c)$	$V_{DC} - V_{MOS} - e_b + e_c$
	$i_a = 0, i_b = 0$	0	0
2	$i_b \neq 0, i_a \neq 0$	$- e_a + e_b$	$- V_{MOS} - e_b + e_c$
	$i_b \neq 0, i_a = 0$	$½ (V_{MOS} + e_b - e_c)$	$- V_{MOS} - e_b + e_c$
	$i_b = 0, i_a \neq 0$	$½ (-V_{MOS} - e_a + e_c)$	$½ (-V_{MOS} - e_a + e_c)$
	$i_b = 0, i_a = 0$	0	0
3	$i_b \neq 0, i_c \neq 0$	$V_{MOS} - e_a + e_b$	$-V_{DC} - e_b + e_c$
	$i_b \neq 0, i_c = 0$	$V_{MOS} - e_a + e_b$	$½ (-V_{MOS} + e_a - e_b)$
	$i_b = 0, i_c \neq 0$	$½ (-V_{DC} + V_{MOS} - e_a + e_c)$	$½ (-V_{DC} + V_{MOS} - e_a + e_c)$
	$i_b = 0, i_c = 0$	0	0
4	$i_c \neq 0, i_b \neq 0$	$V_{MOS} - e_a + e_b$	$- e_b + e_c$
	$i_c \neq 0, i_b = 0$	$½ (V_{MOS} - e_a + e_c)$	$½ (V_{MOS} - e_a + e_c)$
	$i_c = 0, i_b \neq 0$	$V_{MOS} - e_a + e_b$	$½ (-V_{MOS} + e_a - e_b)$
	$i_c = 0, i_b = 0$	0	0
5	$i_c \neq 0, i_a \neq 0$	$V_{DC} - V_{MOS} - e_a + e_b$	$V_{MOS} - e_b + e_c$
	$i_c \neq 0, i_a = 0$	$½ (-V_{MOS} + e_b - e_c)$	$V_{MOS} - e_b + e_c$
	$i_c = 0, i_a \neq 0$	$V_{DC} - V_{MOS} - e_a + e_b$	$½ (-V_{DC} + V_{MOS} + e_a - e_b)$
	$i_c = 0, i_a = 0$	0	0

The voltages and back EMF voltages ($V_{ab} - e_a + e_b$ and $V_{bc} - e_b + e_c$) required to solve Equations 5.12 to 5.16 were calculated and are detailed in Tables 5.2 and Tables 5.3. Inverter Tables were programmed as functions of electrical angle and current states for each switching action. Equations 5.12 to 5.16 are then solved using a Euler backwards (1-point) scheme to resolve transient currents and RPMS for a specified motor voltage and load profile. Examples of the transient model results are located in section 5.4.

5.3. Equivalent DC Motor Performance Model

Three-phase power analysis of AC PMS motors although simple can be numerically expensive due to the short time steps required to resolve the high frequency switching. For faster computation, an equivalent DC model can be implemented. An equivalent DC model is shown in Figure 5.12. Here the motor is reduced to one phase and switch where the phase properties are equivalent to the combined properties of the energize phases. This reduces the number of calculations and variables at each timestep. The required DC voltage, V, is equal to the sum of the back-EMF voltage and voltage losses from voltage balance of the circuit, Equation 5.98.

$$\begin{cases} V = V_{ESC} + Ri + L\frac{di}{dt} + e \\ e = k_e \Omega_M, \end{cases} \tag{5.98}$$

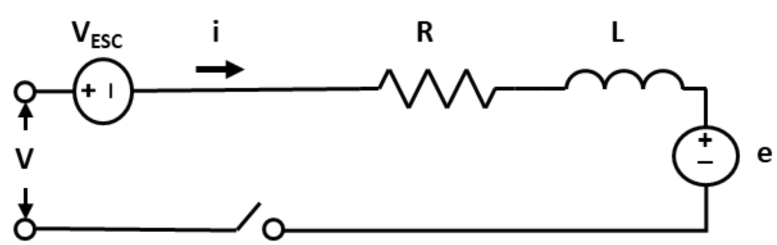

Figure 5.12. DC motor electric circuit

Here i (A) is the current and V_{ESC} (V) is the voltage loss across the ESC. The phase-to-phase resistance, R (ohm), is a function of the wire diameter and the total length of wire used in the winding. Phase-to-phase inductance, L (H), is sum of the self- and mutual-inductance cause by the airgap flux, slot-leakage flux, and end-winding flux. The back-EMF, e (V), is the voltage induced in the stator winding due to its relative motion with the rotating magnets. k_e (rad/V-s) is the phase-to-phase back-EMF coefficient of the motor, and Ω_M (rad/s) is the angular velocity of the motor. Phase-to-phase values are twice the phase value, so $R = 2R_P$, $L = 2L_P$, $k_e = 2k_{e,p}$, $k_t = 2k_{t,p}$.

The mechanical behavior of an electric motor is described by Equation 5.99, where net output load torque, Q_L (N-m), is the electromagnetic torque, Q_e (N-m) minus losses.

$$\begin{cases} Q_L = Q_e - k_f \Omega_M - J \frac{d\Omega_m}{dt} \\ Q_e = k_t i \end{cases} \tag{5.99}$$

Here k_f is a friction coefficient, J is the load (rotor and shaft) inertia, Q_L (N-m) is the load torque (i.e output torque). The electromagnetic torque, Q_e, is a function of the phase-to-phase torque coefficient, k_t (N-m/A), and current, i (A). The net efficiency of the motor is defined by Equation 5.100.

$$\eta_m = \frac{Q_L \Omega_M}{Vi} \tag{5.100}$$

5.4. Comparison of the Three-Phase AC PMS Model and the Equivalent DC Motor Performance Models

To compare the three-phase AC PMS and equivalent DC motor model outputs, Equations 5.12 to 5.16 and Equations 5.9 to 5.99 are solved numerically using a backwards Euler method. A DC brushless motor with detailed properties given in Table 5.4, the Maxon EC6 motor, is simulated and compared in three scenarios. Even though it is a tiny motor, the Maxon EC6 motor was selected because of the completeness of the available manufacturer data. It is simulated in three scenarios, and in all three, the DC model accurately captured the current, RPM, and torque trends of the 3-phase motor as well as the current and RPM ripples for the PWM control logic commutation. However, as expected it did not capture the ripples in current, RPM, and torque from the phase commutation.

Table 5.4. Maxon EC6 motor properties from manufacturer

Motor Property	
Number of poles, poles	2
Nominal Voltage, V	6
No load speed, RPM	45,100
No load current, A	0.0531
Nominal torque, mN-m	0.251
Nominal current, A	0.265
Stall torque, mN-m	0.542
Stall current, A	0.48
Resistance (phase-to-phase), Ω	12.5
Inductance (phase-to-phase), mH	0.0911
Torque Constant, mN-m/A	1.13
Rotor inertia, kgm^2	5E-10
Friction constant, N-m-s	1.274 E-8

In the first scenario, the motor is started under no-load conditions with 100% PWM duty cycle, and at 0.05 seconds a load of 0.251 mN-m (maximum continuous torque) is applied to the motor. The currents of the 3-phase and DC models are shown in Figures 5.13 and 5.14 respectively. The RPM of the 3-phase and DC models are shown in Figures 5.15 and 5.16 respectively. Upon start up the motor current surges to 0.48 A to overcome the stall torque and then reduces to 0.054 A at the no-load RPM of 45k. Upon loading, the current increases to 0.252 A as the RPM decreases to 24k. The torques generated by the motor are shown in Figures 5.17 and 5.18 for the two models, both of which accurately capture the stall torque of 0.54 mN-m.

In the second scenario, the motor is started under no-load conditions with 65% PWM duty cycle, at 0.05 seconds a load of 0.251 mN-m (maximum continuous torque) is applied to the motor.

The currents of the 3-phase and DC models are shown in Figures 5.19 and 5.20 respectively. The RPM of the 3-phase model and DC models are shown in Figures 5.21 and 5.22 respectively. Upon start up the motor current surges to 0.47 A to overcome the stall torque and then reduces to 0.09 A at the no-load RPM of 41k. Upon loading, the current increases to 0.39 A as the RPM decreases to 9k.

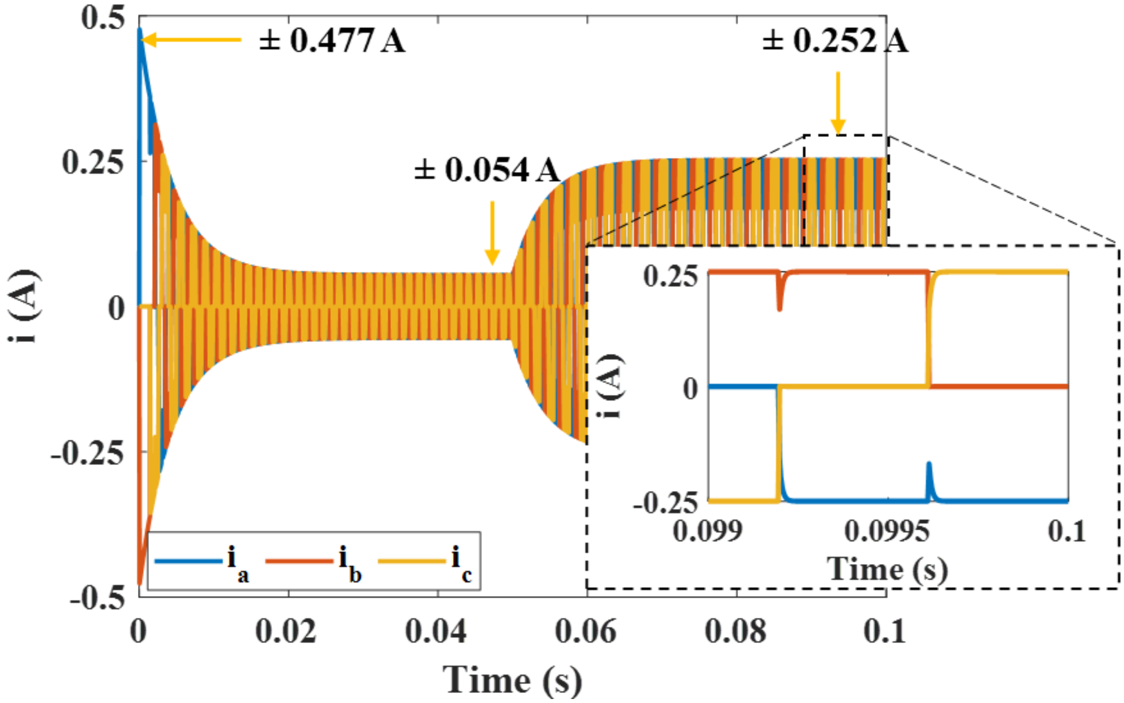

Figure 5.13. Current versus time at 100% duty cycle for the 3-phase model

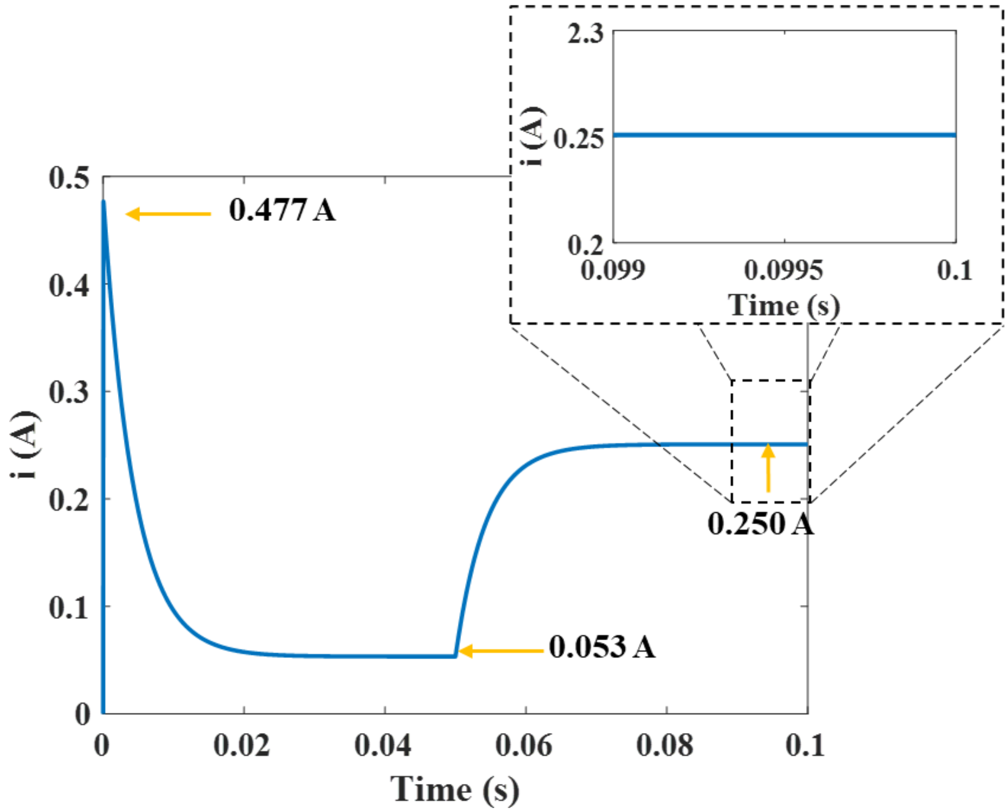

Figure 5.14. Current versus time at 100% duty cycle for the DC model

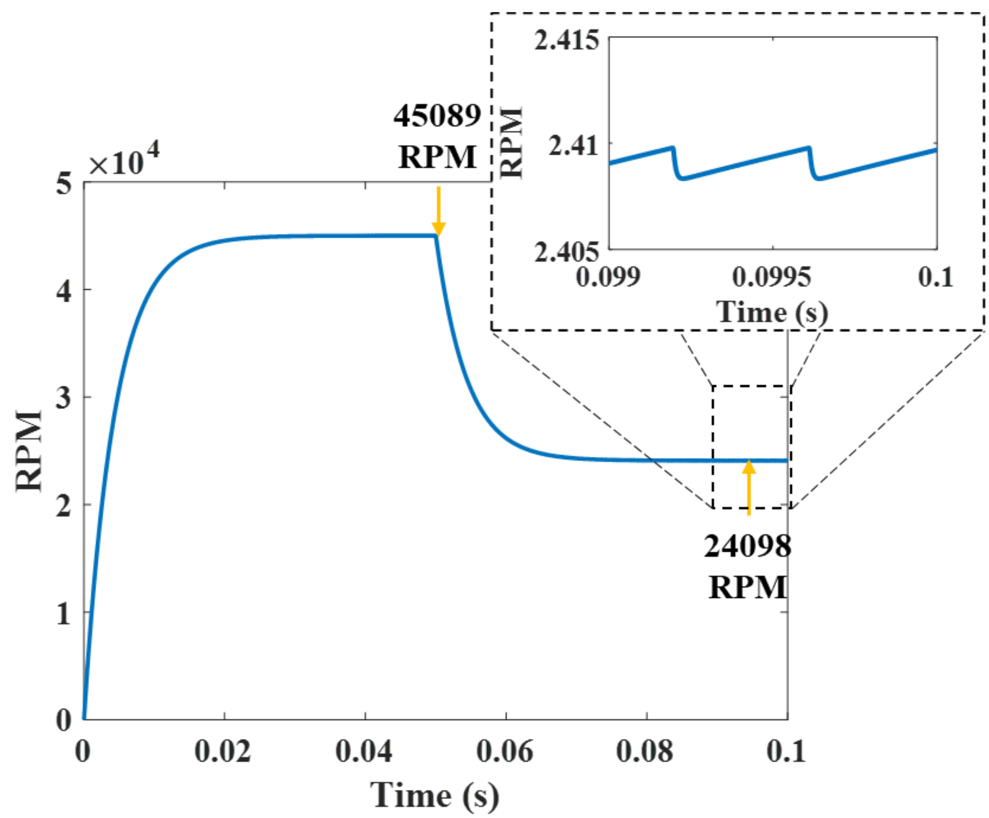

Figure 5.15. RPM versus time at 100% duty cycle for the 3-phase model

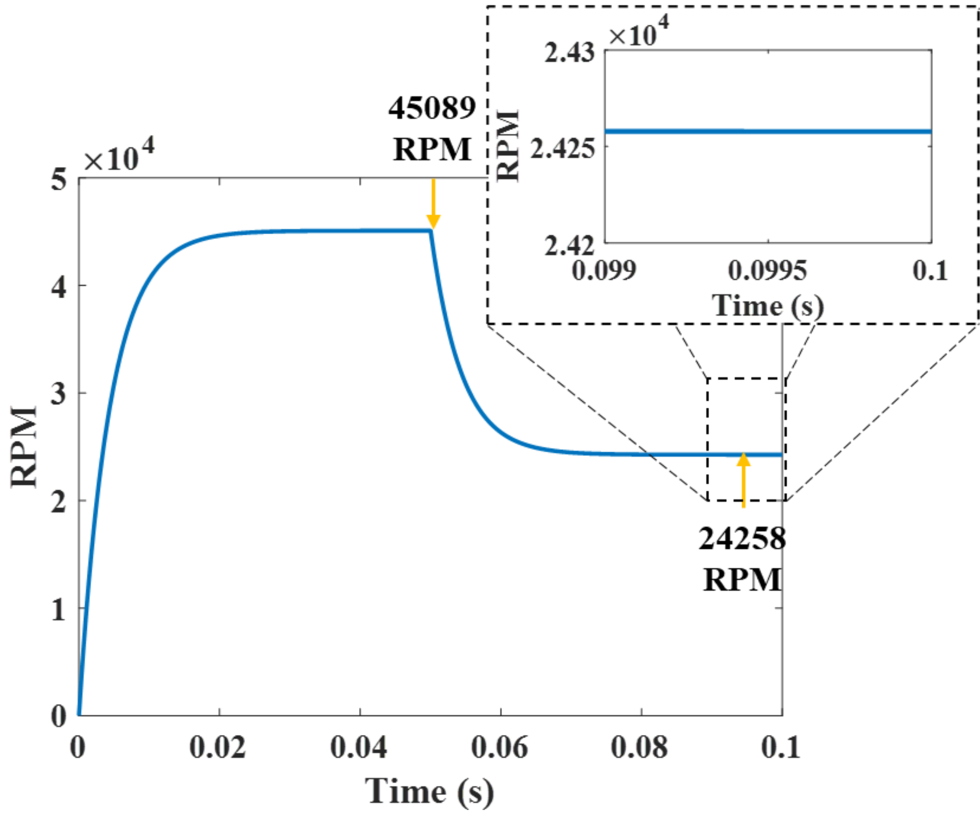

Figure 5.16. RPM versus time at 100% duty cycle for the DC model

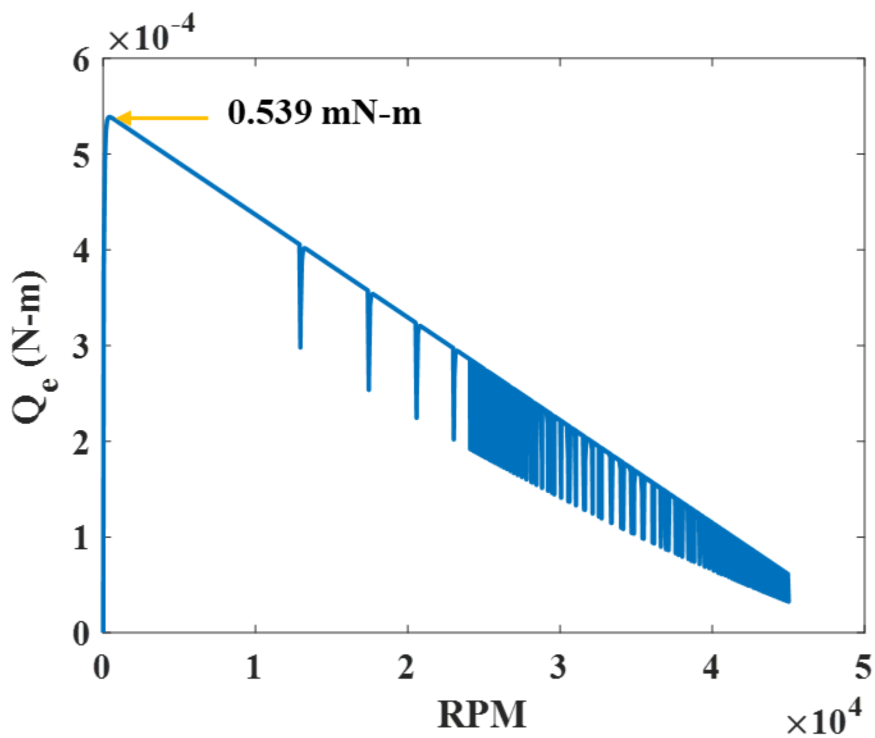

Figure 5.17 Electromagnetic torque versus RPM at 100% duty cycle for the 3-phase model

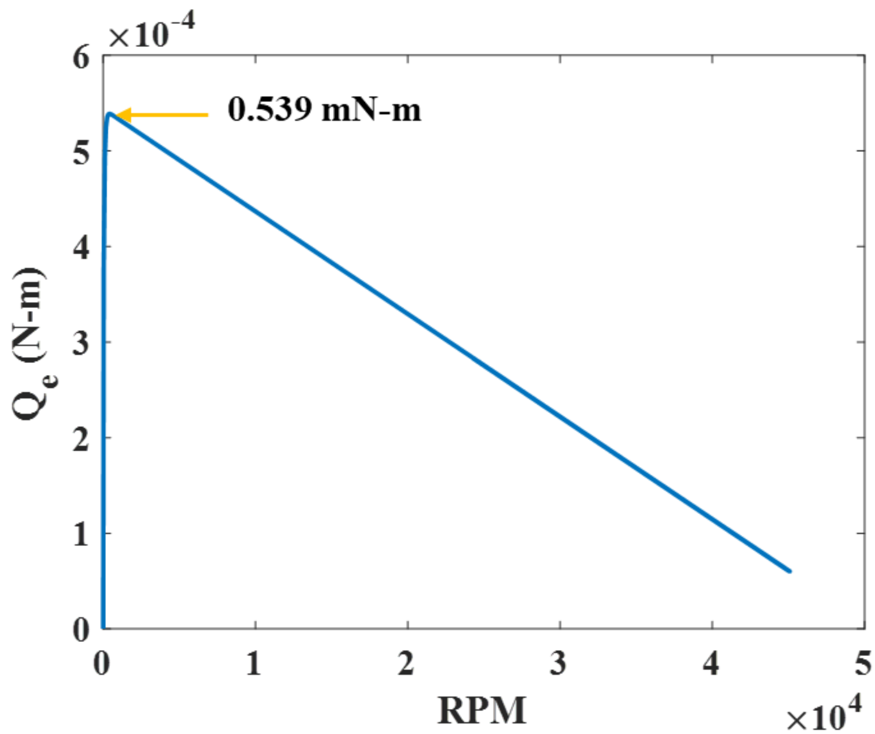

Figure 5.18. Electromagnetic torque versus RPM at 100% duty cycle for the DC model

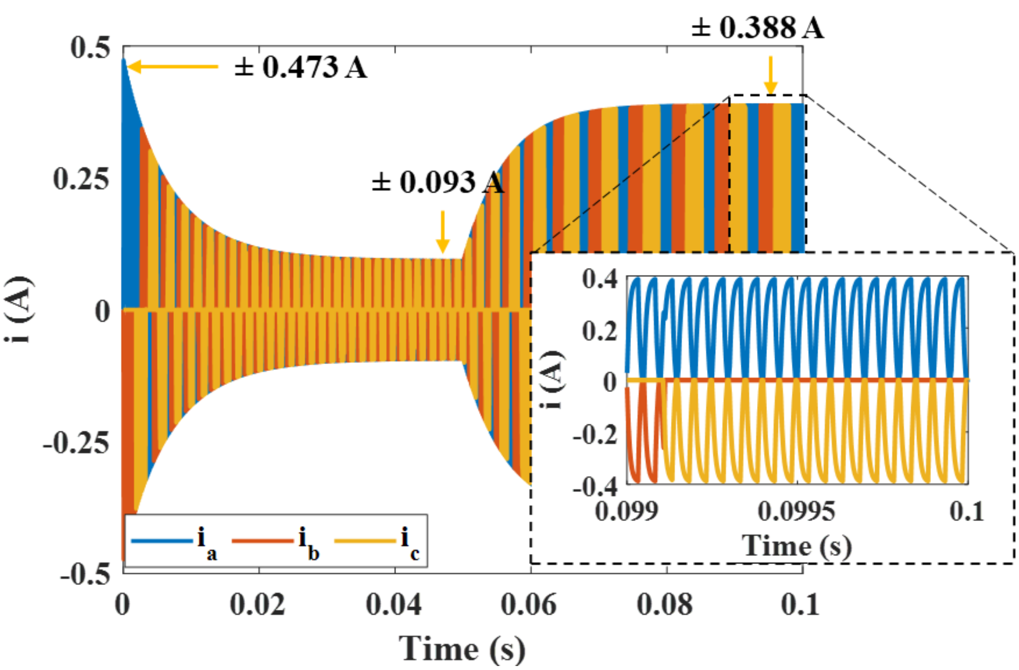

Figure 5.19. Current versus time at 65% duty cycle for the 3-phase model

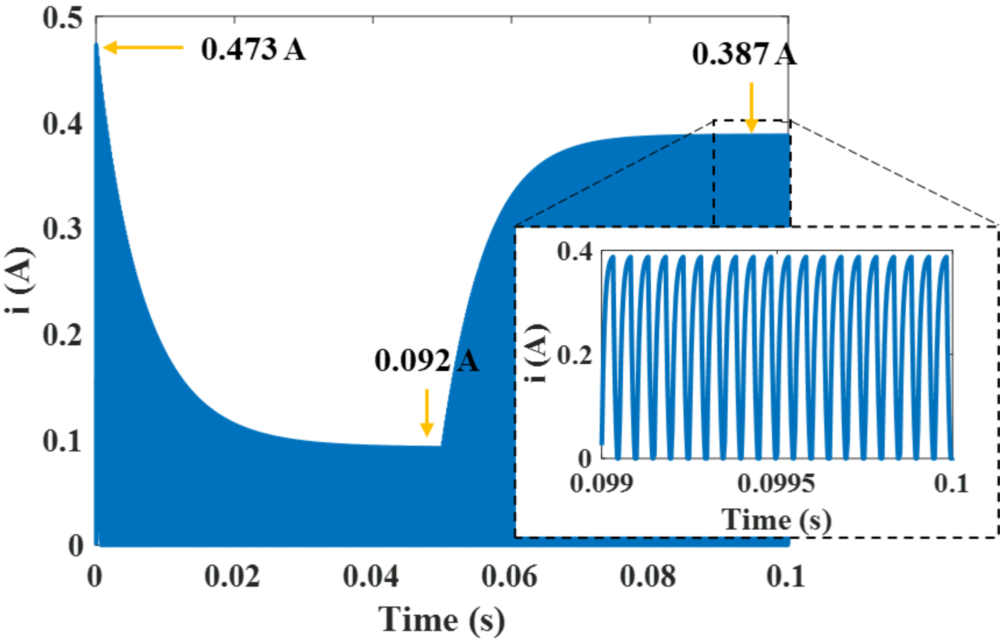

Figure 5.20. Current versus time at 65% duty cycle for the DC model

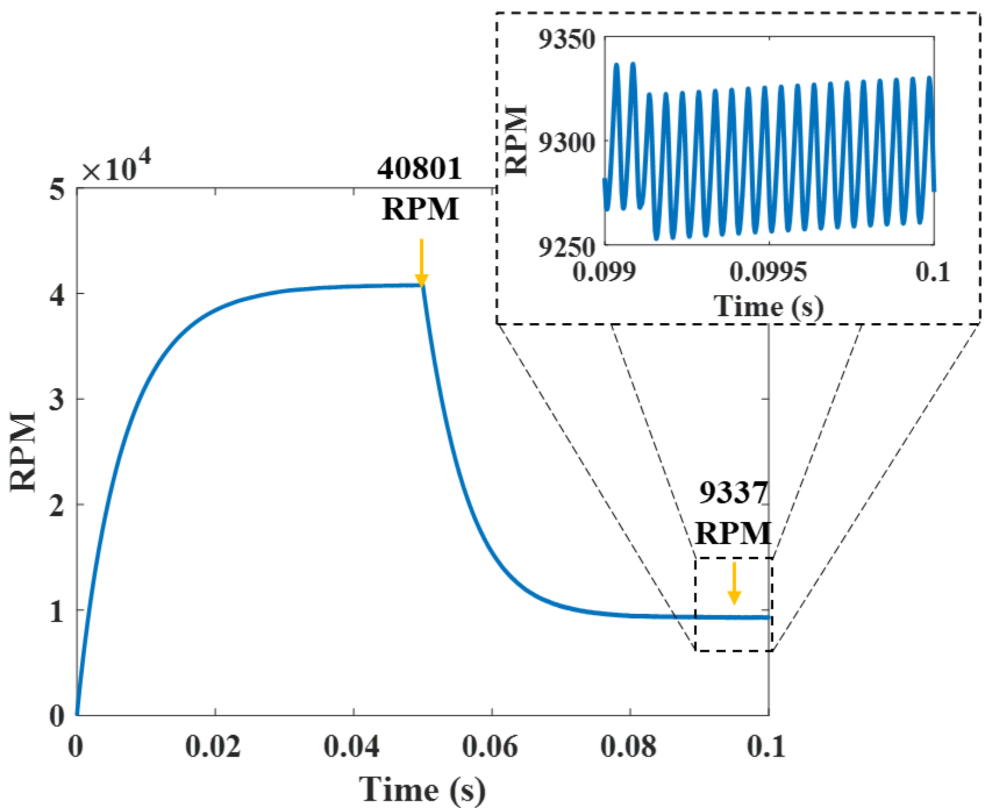

Figure 5.21. RPM versus time at 65% duty cycle for the 3-phase model

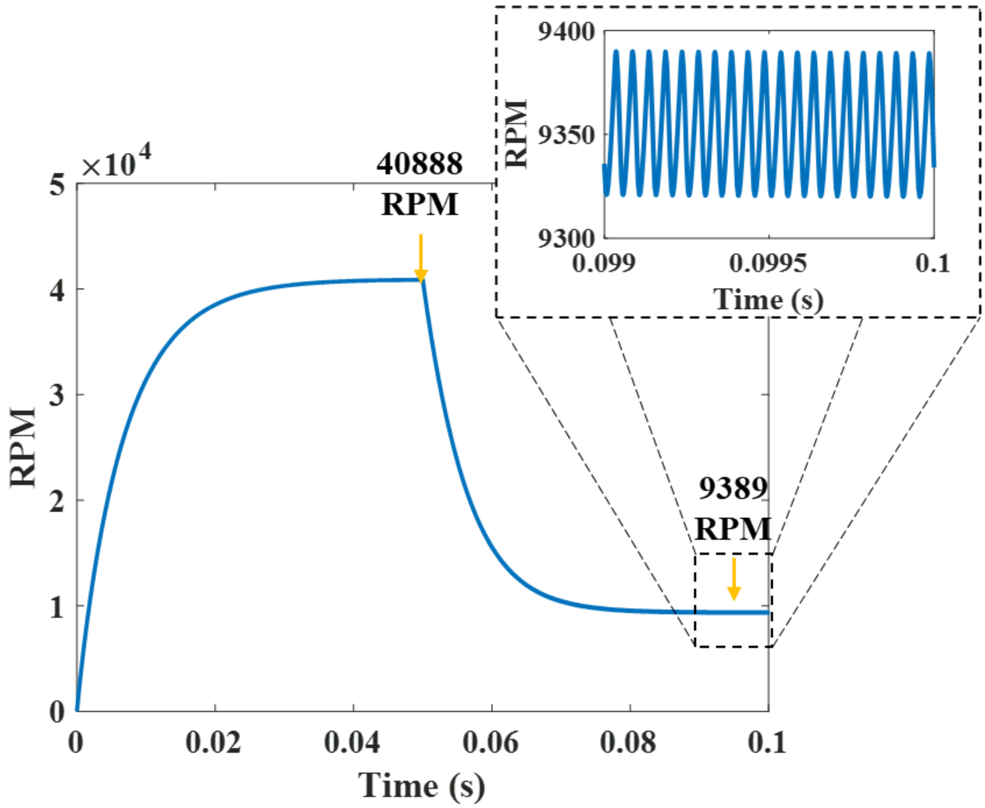

Figure 5.22. RPM versus time at 65% duty cycle for the DC model

In the third scenario, the motor is started under no-load conditions with 30% PWM duty cycle, and at 0.05 seconds a load of 0.125 mN-m is applies to the motor. The current of the 3-phase and DC models are shown in Figures 5.23 and 5.24 respectively. While the RPM of the 3-phase and DC models are shown in Figures 5.25 and 5.26 respectively. Upon start up the motor current surges to 0.42 A to overcome the stall torque and then reduces to 0.17A t the no-load RPM of 30k, with a current of 0.17A. Upon loading the current increases to 0.38 A as the RPM decreases to 5k.

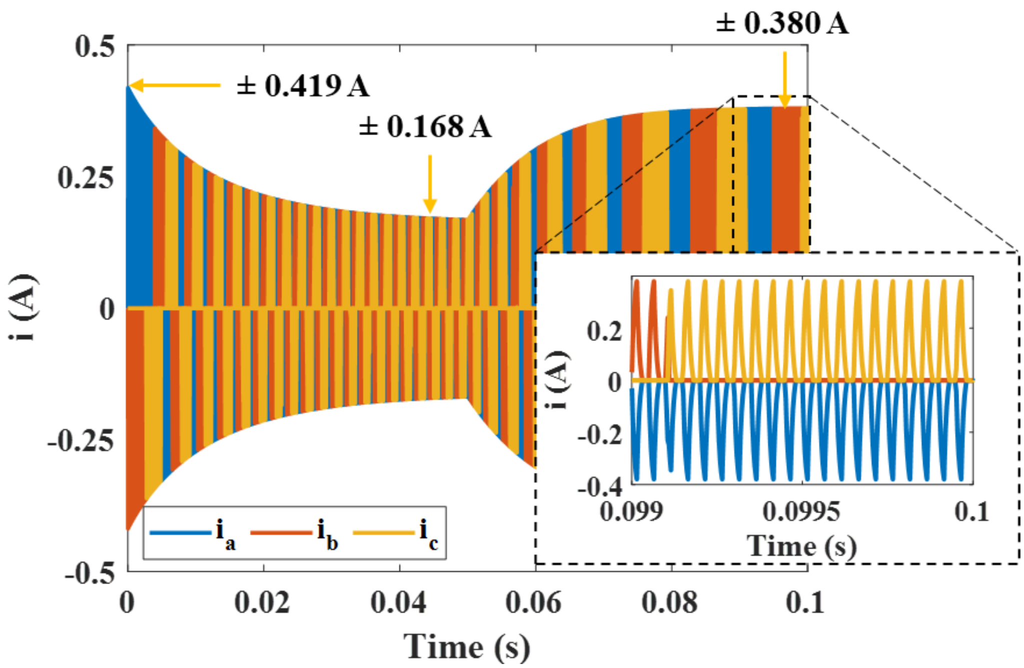

Figure 5.23. Current versus time at 30% duty cycle for the 3-phase model

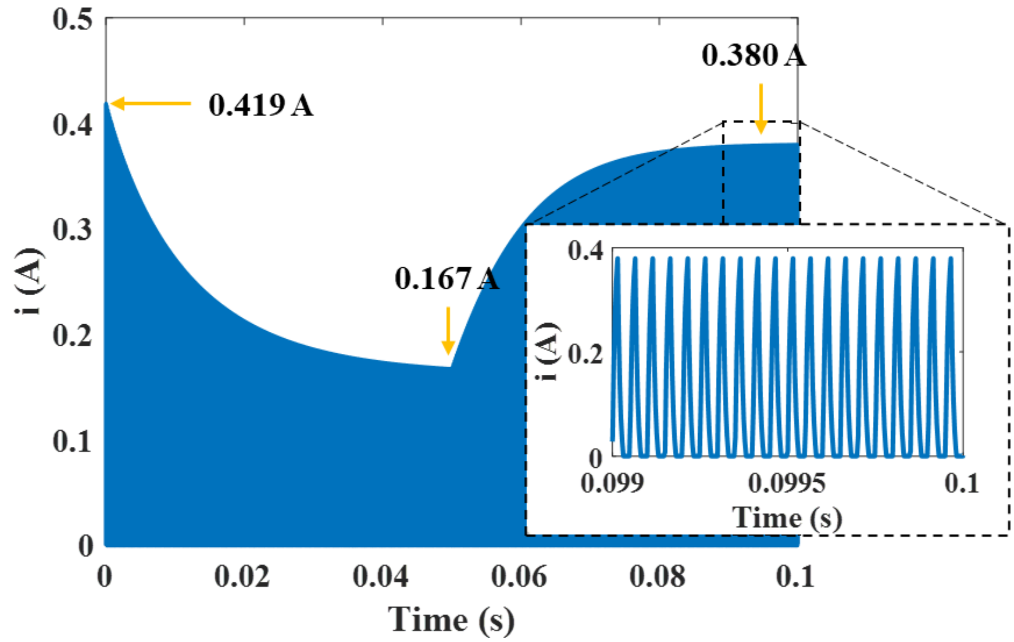

Figure 5.24. Current versus time at 30% duty cycle for the DC model

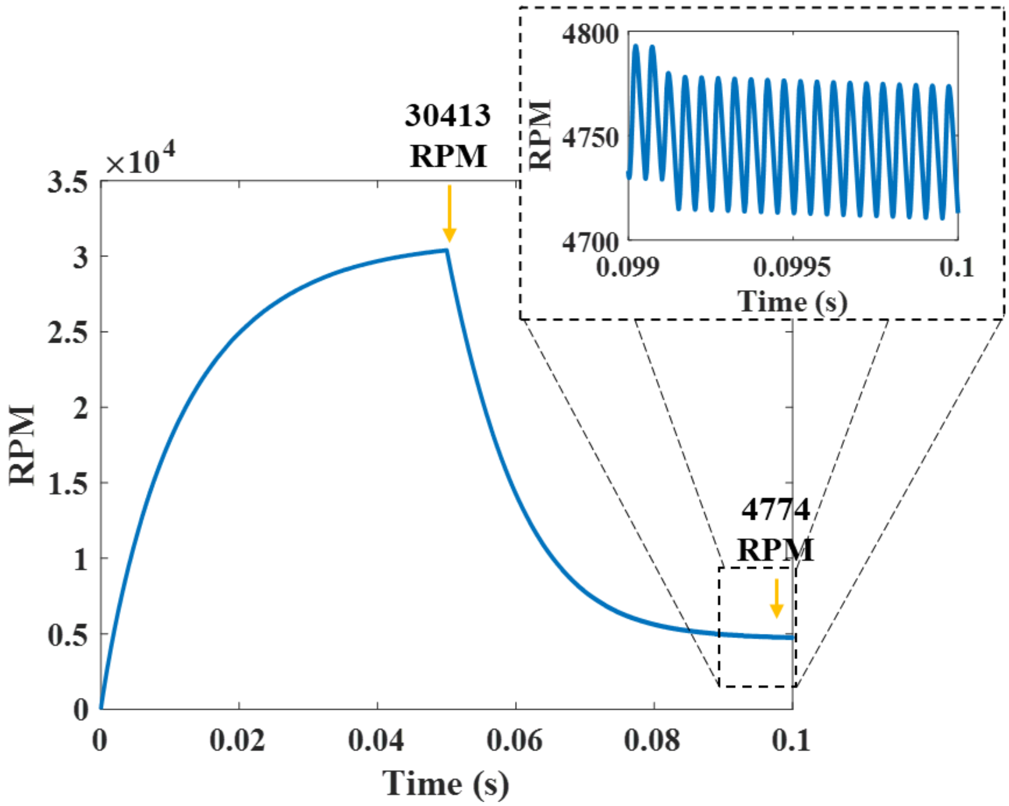

Figure 5.25. RPM versus time at 30% duty cycle for the 3-phase model

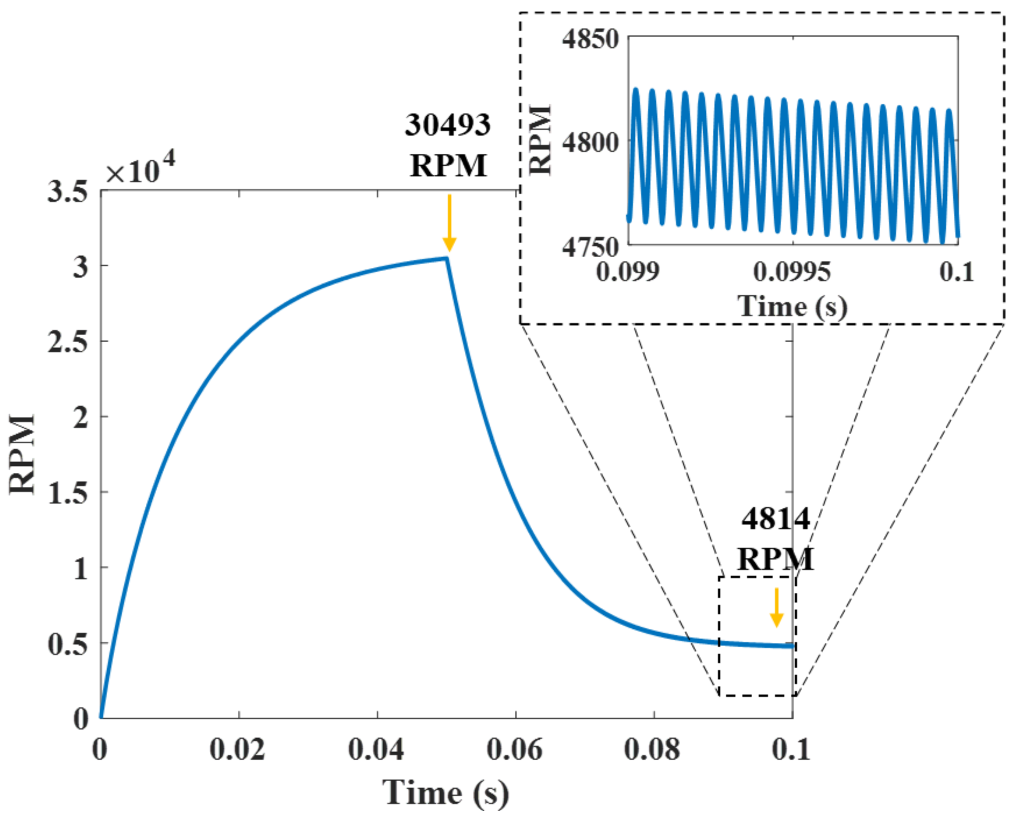

Figure 5.26. RPM versus time at 30% duty cycle for the DC model

5.1. DC Generator Model

AC PMS generators are equivalent to the AC PMS motors controlled and operated in reverse. For the sake of brevity, only the equivalent DC model is described. The equivalent circuit is shown in Figure 5.27 and described by Equation 5.101. V_{DC} is the output DC bus voltage, and i is the load current. V_{REC} is the voltage loss across the rectifier. The rectifier is essentially the opposite of an inverter, in that it converts AC voltage to DC voltage. The phase-to-phase resistance, R, is function of the wire diameter and the total length of wire used in the winding. Phase-to-phase inductance, L, is sum of the self- and mutual-inductance cause by the airgap flux, slot-leakage flux, and end-winding flux. The back-EMF, $e = k_e \Omega_E$, is the voltage induced in the stator winding due to its relative motion with the rotating magnets. Where k_e is the phase-to-phase back-EMF coefficient of the motor, and Ω_E is the angular velocity of the generator (i.e engine angular velocity).

$$\begin{cases} V_{DC} = e - V_{REC} - Ri - L\frac{di}{dt} \\ e = k_e \Omega_E, \end{cases} \tag{5.101}$$

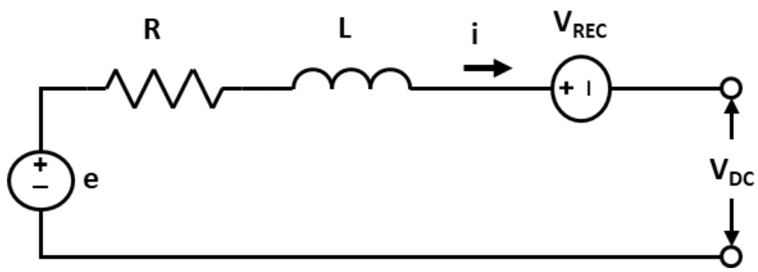

Figure 5.27. DC Generator Electric Circuit

The mechanical behavior of an electric generator is described by Equation 5.102, where the driving engine torque, Q, is the induced electromagnetic torque, Q_e, plus the inertial torque and losses.

$$\begin{cases} Q = Q_e + k_f \Omega_E + J\frac{d\Omega_E}{dt} \\ Q_e = k_t i \end{cases} \tag{5.102}$$

Here k_f is a friction coefficient, and J is the rotor/load inertia. The electromagnetic torque, Q_e, motor is a function of to phase-to-phase torque coefficient of the motor, k_t, and current.

The net efficiency of the generator is defined by Equation 5.103.

$$\eta_g = \frac{V_{DC} i}{Q \Omega_E} \tag{5.103}$$

5.2. Higher Order Performance and Losses

In addition to the ohmic voltage losses from resistance, iR, and voltage losses across the MOSFETS, V_{MOS}, $V_{ESC,}$, V_{REC}, and the torque losses from bearing friction, $k_f \Omega_E$, additional higher order losses can become important for predicting performance precisely. These losses are shown in Equations 5.104 to 5.106. Equation 5.104 modifies Equation 5.9 of the three-phase motor model. Equation 5.105 modifies Equation 5.99 of the equivalent DC motor model. Equation 5.106 modifies Equation 5.102 of the equivalent DC generator model.

$$\begin{cases} Q_e = k_f \Omega_m + J \frac{d\Omega_m}{dt} + Q_L - Q_{Iron} - Q_{Wind} - Q_{Stray} \\ Q_e = \sum_{n=a}^{c} k_{t,p} i_n \end{cases} \tag{5.104}$$

$$\begin{cases} Q_L = Q_e - k_f \Omega_m - J \frac{d\Omega_m}{dt} - Q_{Iron} - Q_{Wind} - Q_{Stray} \\ Q_e = k_t i \end{cases} \tag{5.105}$$

$$\begin{cases} Q = Q_e + k_f \Omega_E + J \frac{d\Omega_E}{dt} - Q_{Iron} - Q_{Wind} - Q_{Stray} \\ Q_e = k_t i \end{cases} \tag{5.106}$$

Here the mechanical losses of the motor are a function of the bearing friction, $k_f \Omega$, eddy current and hysteresis losses of the iron core, Q_{Iron} (N-m), aerodynamic loses of the rotor and windage, Q_{Wind} (N-m), and torque loss from stray sources, Q_{Stray} (N-m).

$$Q_{Iron} = \frac{m_{Iron}(k_h f^{\alpha} B^{\beta} + k_{ec} f^2 B^2)}{\Omega_M} \tag{5.107}$$

Iron losses, described by Equation 5.107, are higher order frequency dependent losses from hysteresis and eddy current effects that require geometric and material properties to model. In Equation 5.107, m_{Iron} (kg) is the mass of the iron stator, k_h (W/kg-Hz$^{\alpha}$-T$^{\beta}$) is the hysteresis coefficient of the iron, f (Hz) is the switching frequency, B (Tesla (T)) is the iron flux density, α and β are Steinmetz coefficients, and k_{ec} (W/kg-Hz^2-T^2) is the eddy current coefficient of the iron.

$$Q_{Wind} = C_D \pi \rho_f {\Omega_M}^2 r^4 L \tag{5.108}$$

Windage loss is from aerodynamic drag and is estimated by Equation 5.108 under the assumption of a smooth cylinder rotating within a concentric cylinder (i.e., Couette flow). In Equation 5.108, C_D is the skin friction coefficient of the rotor, ρ_f (kg/m^3) is the density of the fluid between the rotor and stator, r (m) is the radius of the rotor surface, and L (m) is the length of the rotor surface.

Stray losses can include cogging torque (torque required to start the motor rotation), losses from component and material scattering, and production losses. Cogging torque and stray losses are not easily calculated but typically represent only a minor portion of motor losses. Cogging torque losses is due to interactions with the permanent magnets and stator slots. It is position dependent and prominent at lower speeds.

An examination of the motor performance and loss parameters was conducted to characterize the contribution of each loss. The motor inductance and inertial load are transient parameters not required for steady-state performance and were not examined. To verify the results, this EMRAX 188 motor is selected instead of the KDE motor of the powertrain, as a complete set of parameters available in the public domain for this motor.

Figure 5.28 shows the efficiency contours (does not include the controller losses) of the manufacturer provided EMRAX 188 motor (solid) overlaid with the predicted efficiency (dotted).

Here only the ohmic losses (Ri) and kinetic losses ($k_f \Omega_E$) with constant parameters are included (power electronic losses are not included). As current (torque) increases efficiency decreases due to the resistance and as angular velocity increases the efficiency decreases due to friction. The model does not adequately capture the efficiency trends.

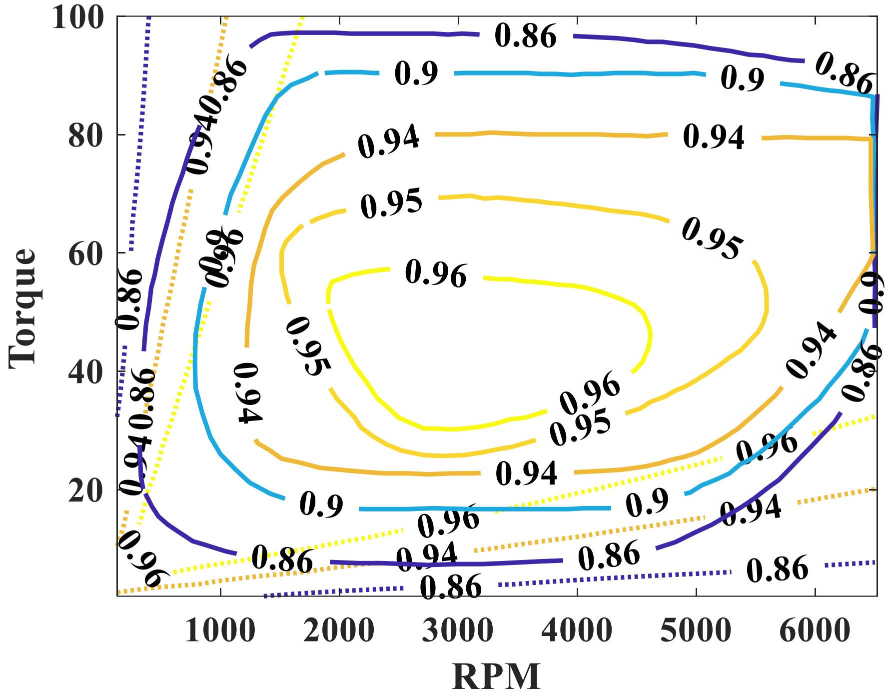

Figure 5.28. Output torque versus RPM with predicted (dotted) vs manufacturer (solid) motor efficiency contours with constant parameters and linear ohmic and kinetic losses

Next, we include the frequency dependent iron and windage losses. From the motor geometry, the iron mass, rotor radius and length are calculated. The iron is assumed to be M250-35A grade steel for the eddy current and hysteresis coefficients defined in Table 5.5. Figure 5.29 overlays the EMRAX 188 (solid) with the predicted efficiency (dotted) with the iron and windage losses included. These losses reduce efficiency with motor speed but still do not create the efficiency islands observed in the manufacturer data.

Table 5.5. Coefficients for the eddy current and hysteresis losses

Variable	Symbol	Unit	Value
Hysteresis coefficient	k_h	$\frac{W}{kg \cdot Hz^{\alpha} \cdot T^{\beta}}$	0.00778
Eddy current coefficient	k_{ec}	$\frac{W}{kg \cdot Hz^{2} \cdot T^{2}}$	3.15E-5
Steinmetz coefficient	α	m	1.231
Steinmetz coefficient	β	m	1.79

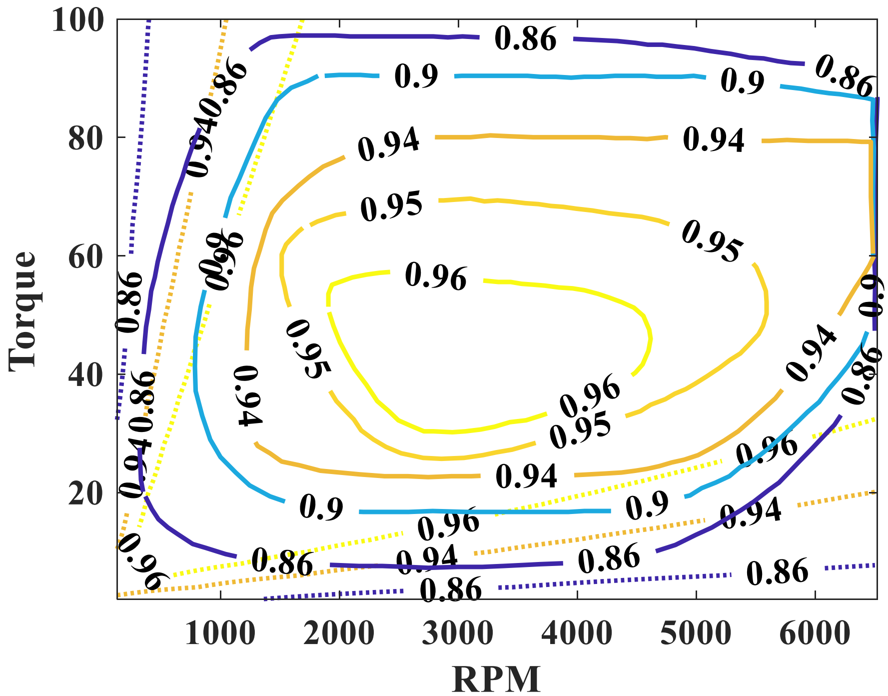

Figure 5.29. Output torque versus RPM with predicted (dotted) vs manufacturer (solid) motor efficiency contours with frequency dependent (iron and windage) losses

For speeds below 2,000 RPM, the manufacturer data contains a decaying non-linear profile in the free-running losses (losses during no-load operation). These losses are likely due to the stray losses which include the cogging torque. The motor specific stray losses can be obtained by subtracting out the previous losses and then fitting a curve decaying loss profile shown in Equation 5.109. Figure 5.3 overlays the EMRAX 188 (solid) with the predicted efficiency (dotted) with these non-linear stray losses included. This creates the boundary curves in the lower left quadrant of the efficiency plot. However, it still does not create the full efficiency island observed in the manufacturer data.

$$Q_{Stray\ (EMRAX-188)} = 7.446\Omega_M{}^{-0.5368} + 0.09221 \tag{5.109}$$

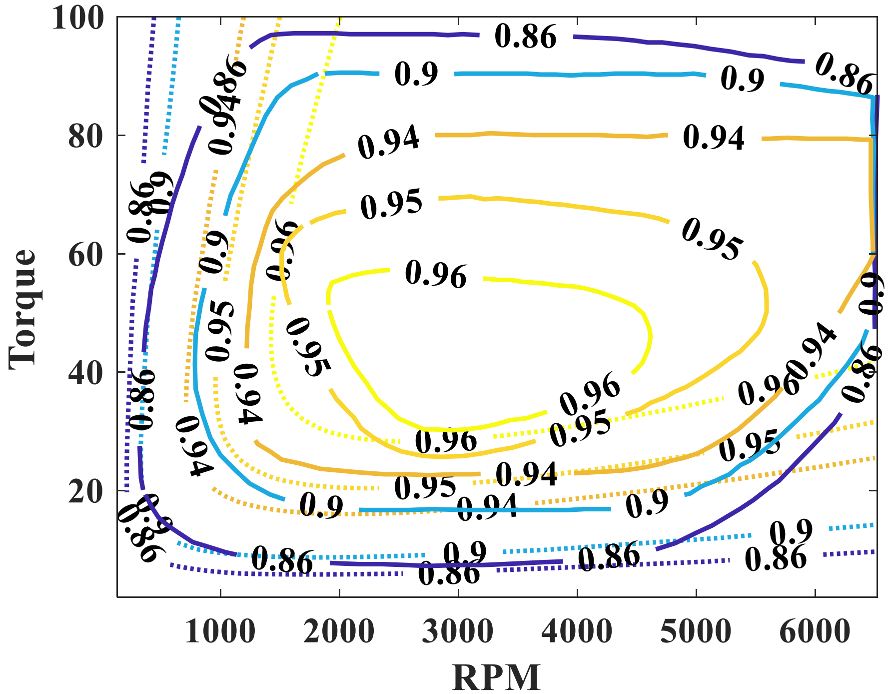

Figure 5.30. Output torque versus RPM with predicted (dotted) vs manufacturer (solid) motor efficiency contours with Stray and Cogging losses

Until this point, the motor parameters have been assumed to be constant during operation. However, these parameters may change as a function of temperature, as with resistance, or as a function of control logic, as with the back-EMF constant. Ohmic (resistive) losses in the copper windings are dissipated as heat. As currents increase, the wire temperature increases due to this heat energy. However, the resistivity of copper also increases with temperature, $R = R_o(1 + 0.00393\Delta T)$. A generic exponential temperature-resistance model was implemented, Equation 5.110, where the change in temperature is a function of ratio of operating current to maximum current, $\Delta T = 8.1323e^{2.853(i/i_{max})}$. Figure 5.31 overlays the EMRAX 188 (solid) with the predicted efficiency (dotted) with non-linear resistance. While this creates additional losses at higher torques it still does not create the closed loop efficiency contours in the continuous operation range.

$$R = R_o\left(1 + 0.03196\, e^{2.853(i/i_{max})}\right) \tag{5.110}$$

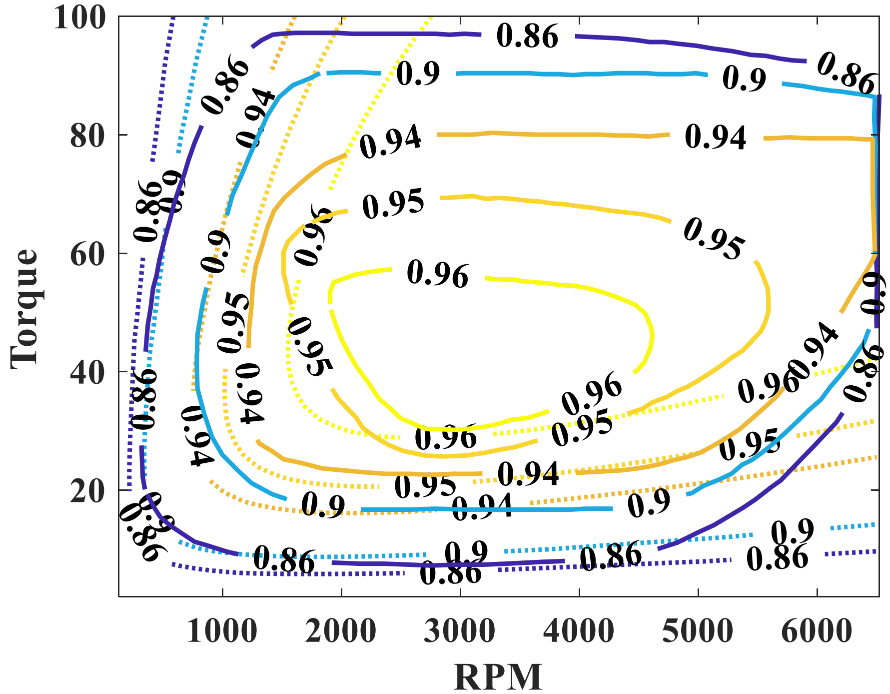

Figure 5.31. Output torque versus RPM with predicted (dotted) vs manufacturer (solid) motor efficiency contours with non-linear resistance

Advanced motor controllers have integrated software that can modulate the flux of the motor commonly referred to as flux weakening. Flux weakening uses the stator current to counter the fixed-amplitude magnetic airgap flux generated by the rotor magnet trading maximum torque for increasing motor speed. Flux weakening results in a change in torque and back-EMF coefficients. From manufacturer data, the torque and back-EMF coefficients are a function of torque and speed. Figure 5.32 overlays the EMRAX 188 (solid) with the predicted efficiency (dotted) with non-constant torque and back-emf coefficients. By modulating flux with a first-order Equation developed for the EMRAX 188, the varying torque and back-EMF coefficients create the closed loop efficiency contours in the continuous operation range. Thus, the efficiency trends and magnitudes can be modeled for even the most complex motors provided the higher order phenomena are captured in the model.

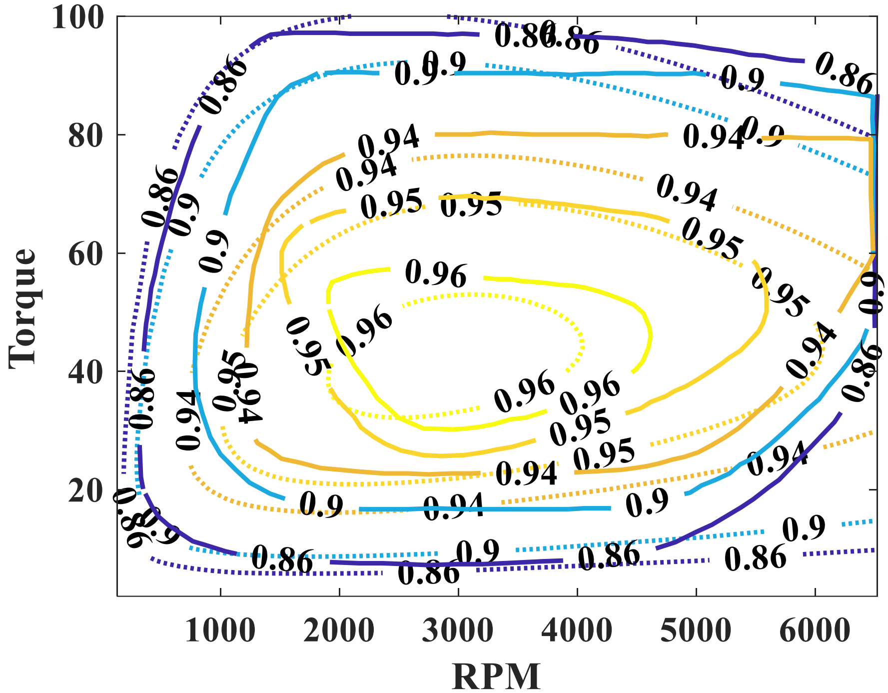

Figure 5.32. Output torque versus RPM with predicted (dotted) vs manufacturer (solid) motor efficiency contours with non-constant torque and back-EMF coefficients (i.e., Flux weakening)

5.3. Calibration of Constants and Validation

The goal of the motor performance model is to predict the required input current and voltage for a specified rotor torque and RPM. Six motor parameters (R, L, k_f, J, k_t, k_e), are typically specified by the manufacturer (alternatively they could be measured for a specific motor). The ten motor loss parameters (m_{Iron}, k_h , f, B, α, β, k_{ec}, C_D, r_r, L) are harder to find but can be calculated with motor geometric and material data available to designers.

In this section, we will utilize the DC equivalent motor and generator models in steady-state to validate the model and compare with the experiment data. We assume the resistance is constant as the motors are operating below the continuous torque limit, with sufficient cooling (i.e., minimal resistance heating). Additionally, the motors are not operating in the flux weakening regime, so the torque and back-emf coefficients are assumed to remain constant throughout motor operation. Finally, the motor core is assumed to be M250-35A grade steel for the eddy current and hysteresis coefficients and the geometric properties are calculated with manufacturer data and drawings. The manufacturer data do not provide enough details to model any startup losses, which may affect accuracy at the lower RPM boundaries.

Figures 5.33 and 5.34 plot the predicted motor efficiency as a function of power for a specified DC voltage of 25- and 50-V. The predicted motor efficiency with constant rotor torque (dotted) and RPM lines (dash-dot) are overlaid on the experimental motor efficiency, with constant torque (dashed) and RPM lines (solid) marked. The trends and magnitudes remain consistent between the experimental and predicted efficiency.

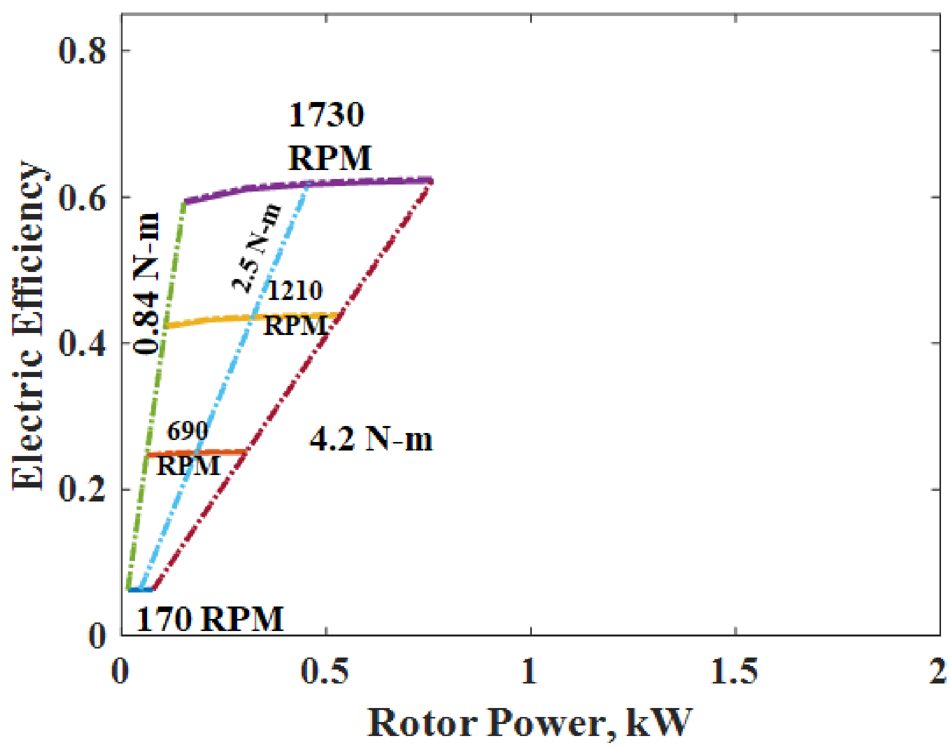

Figure 5.33. Motor Efficiency versus total output rotor power with predicted (dotted, dash-dot) and measured (solid, dashed) output RPM and torque contours for 25-V DC voltage

The predicted efficiency contours of the generator as a function of input torque and RPM are shown in Figure 5.35, with constant power lines marked. The predicted efficiency contours (dotted) are overlaid on the experimental efficiency contours (solid). As the generator converts the input torque and RPM into an output current and voltage, the efficiency can be also plotted as a function of these quantities. The predicted net efficiency contours of the generator as a function of output current and voltage is shown in Figure 5.36, with constant power lines marked. For a specified power, predicted efficiency is lower at the torque and RPM boundaries. Figure 5.37 plots the predicted generator efficiency as a function of power. The predicted generator efficiency with constant current (dotted) and voltage lines (dash-dot) are overlaid on the experimental generator efficiency, with constant current (dashed) and voltage lines (solid) marked. The trends and magnitudes remain consistent between the experimental and predicted efficiency.

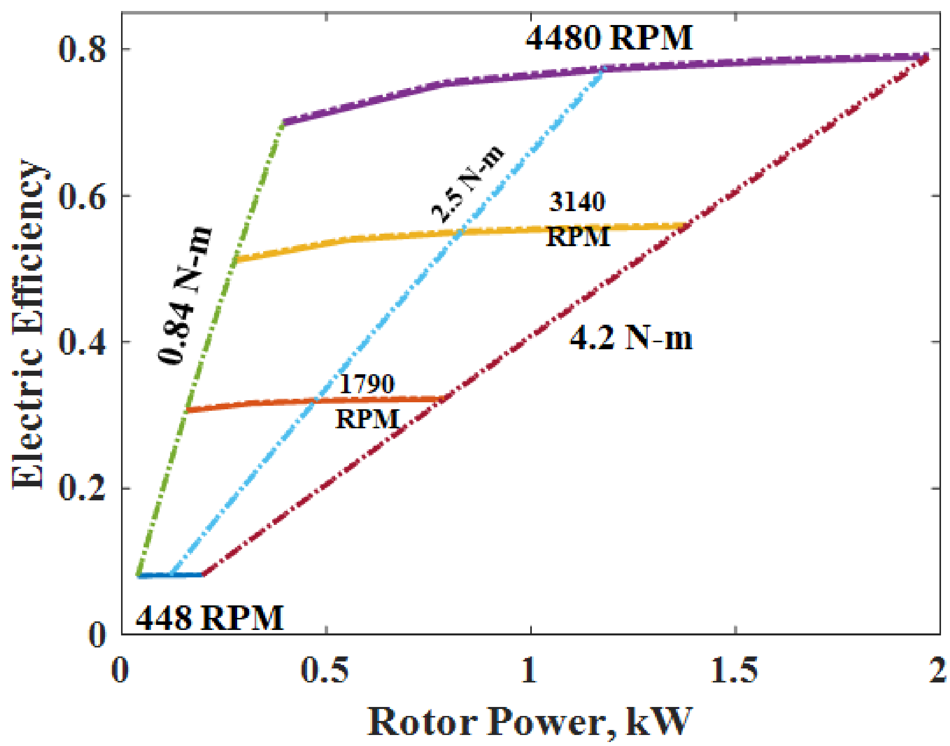

Figure 5.34. Motor Efficiency versus total output rotor power with predicted (dotted, dash-dot) and measured (solid, dashed) output RPM and torque contours for 50-V DC voltage

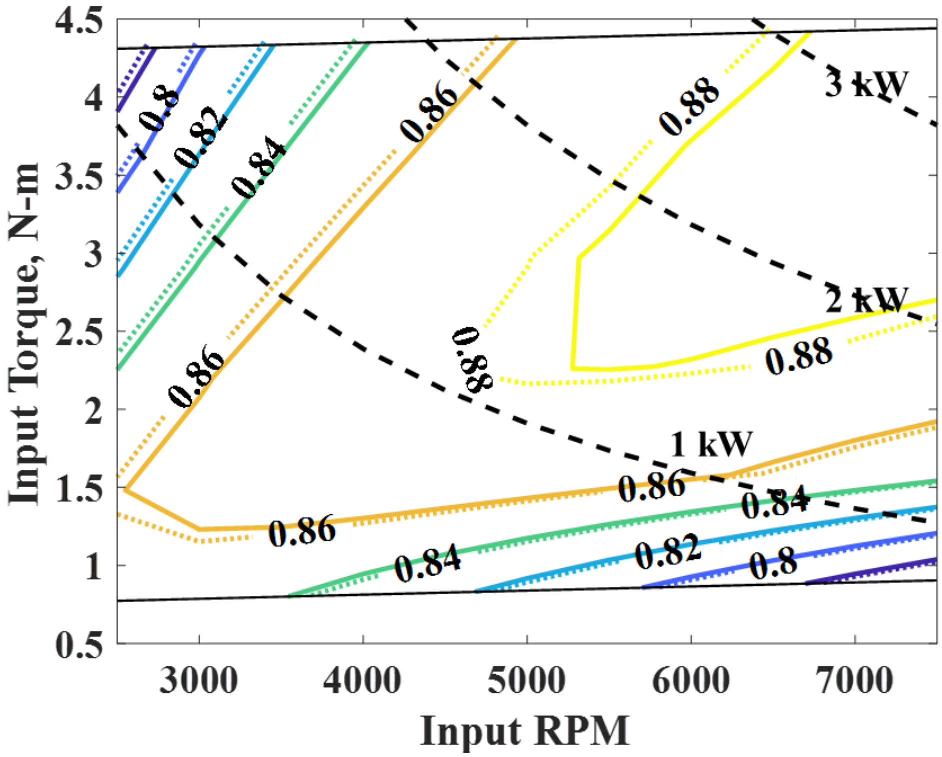

Figure 5.35. Input torque versus RPM with predicted (dotted) and measured (solid) generator efficiency contours

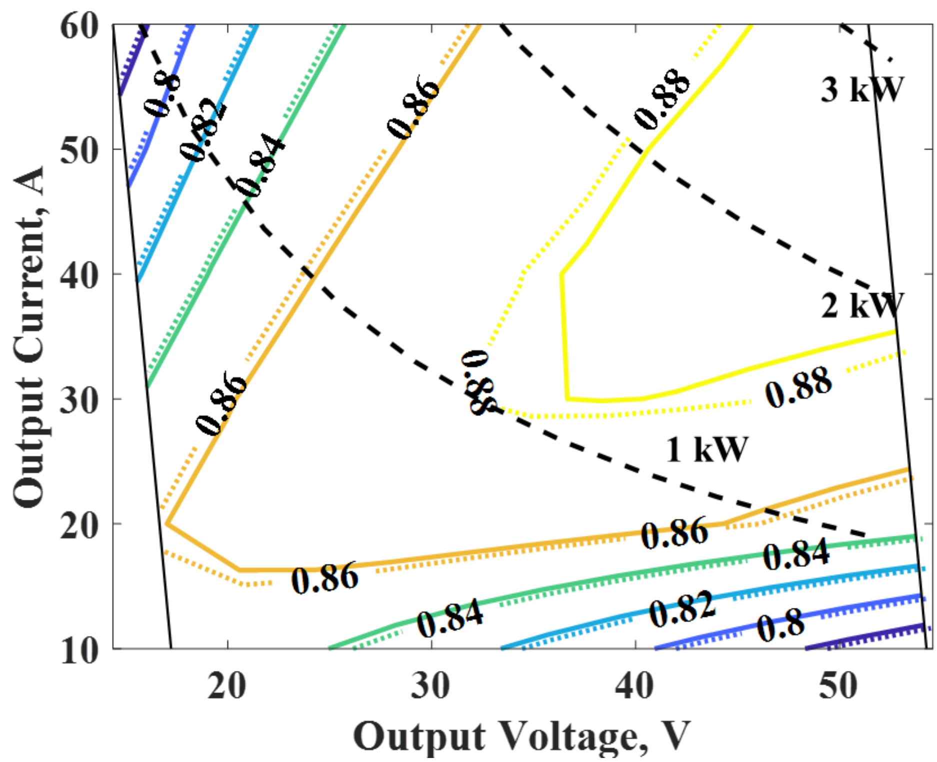

Figure 5.36. Output current versus voltage with predicted (dotted) and measured (solid) generator efficiency contours

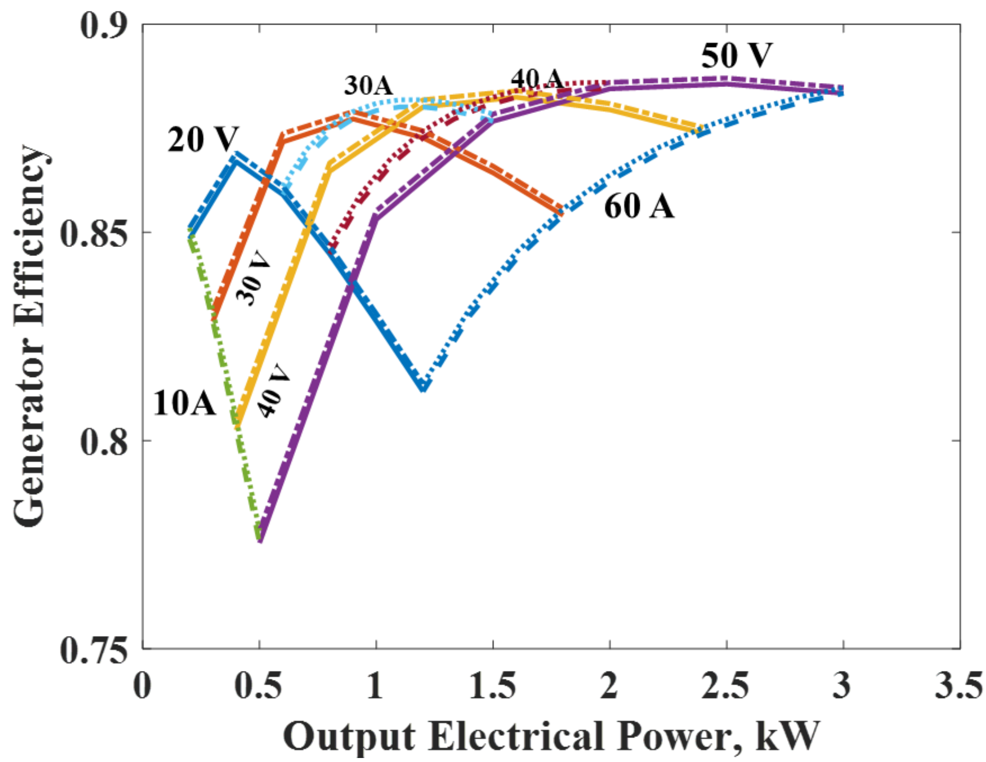

Figure 5.37. Generator efficiency versus output electrical power with predicted (dotted, dash-dot) and measured (solid, dashed) output voltage and current contours

5.4. AC PMS Motor Weight Models

Electric motors/generators scale with volume, which in turn scales with torque [23]. A curve fit of 49 commercial DC brushless motors ranging from 0.4N-m to 500 N-m is given in Equation 5.111. Motors below 13 N-m almost exclusively use air cooling and a continuous maximum torque time limit of around 3 minutes. Motors above 13 N-m are typically liquid cooled. Equation 5.111 accounts for this difference. Figure 5.38 shows the motor weight, W in kg, as a function of maximum continuous torque, Q in N-m, with dashed lines indicating an average error of 20%.

$$\begin{cases} W = 0.2519\ Q^{0.5857}, Q \leq 13\ N\text{-}m \\ W = 0.0.1062\ Q^{1.0422}, Q > 13\ N\text{-}m \end{cases} \tag{5.111}$$

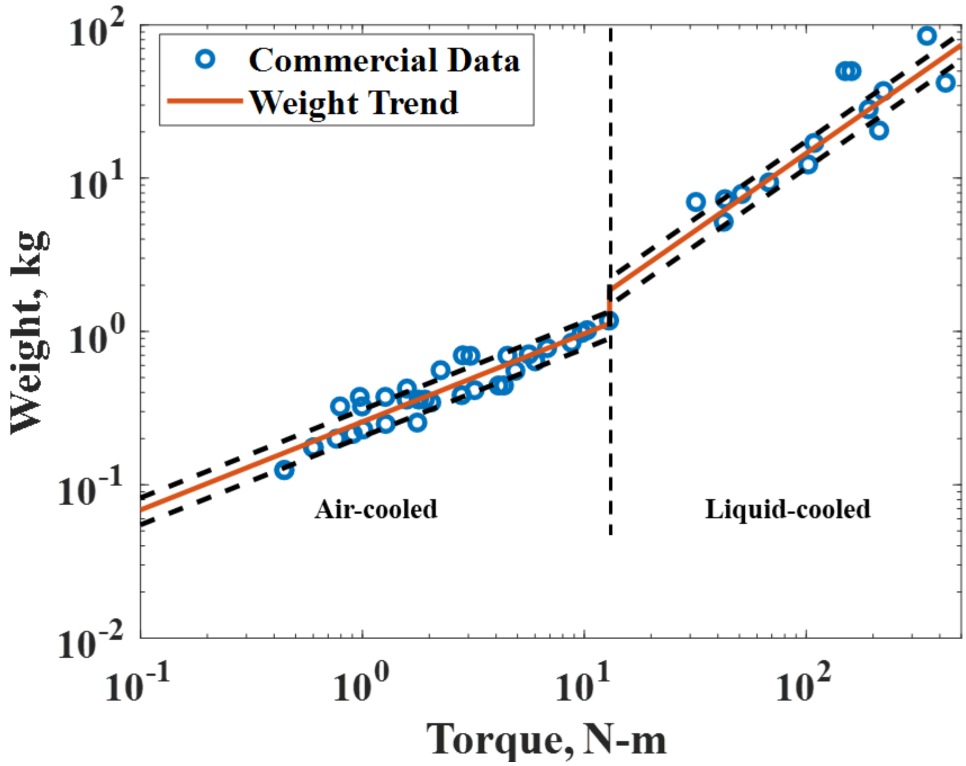

Figure 5.38. AC PMS motor/generator weight verses maximum continuous brake torque with predicted weight trends and 20% error boundaries for 51 motors

5.5. Geometric Weight Model

An alternative to the curve fit is desired for a new design. A geometric weight model proposed here is a synthesis of models developed by Meier et al. [24, 25, 26] with additional constraints [22, 27, 28] tailored specifically for the outrunner DC brushless geometry. The user inputs the maximum continuous torque, outer motor diameter, and the overall length of the motor. The model iterates 5 geometric parameters to predict the minimum weight using 3 user specified input parameters, 16 fixed input parameters, and 23 calculated parameters. These are listed in Table 5.6.

The geometry of an electric motor affects its electrical and magnetic properties. As such, the iterative process allows the examination of multiple motor geometries to minimize weight while meeting the geometric, electrical, and magnetic constraints. Figure 5.39 defines the principal geometric parameters of the motor: the magnet length (l_m), airgap length (δ), inner stator diameter

(D_i), outer stator diameter (D_s), inner rotor diameter (D_r), and the outer rotor diameter (D_o) on a cross-sectional view of an outrunner PMS motor. Figure 5.40 defines the finer details of the slot geometry: the slot tooth bore width (b_{ss0}), outer slot bore width (b_{ss1}), inner slot bore width diameter (b_{ss2}), slot tooth thickness (t_{st}), slot height (h_{ss}), slot tooth height (h_{sw}), stator yoke thickness (t_{sy}), rotor yoke thickness (t_{ry}), and the slot pitch (τ_s).

Table 5.6. Geometric model parameters (in order of appearance)

Variable	Symbol	Unit	Value
	User Specified Parameters		
Outer rotor diameter	D_o	m	Specified
Maximum continuous torque	Q	m	Specified
Motor core length	L	m	Specified
	Fixed Parameters		
Number of Slots	N_{slot}		12
Stator Yoke Thickness Function	f_{sy}		0.5
slot tooth height	h_{sw}	m	0.0005
Number of Magnets	N_{mag}		14
Remanence Flux Density (Neodymium)	B_r	Tesla	1.08
Relative permeability (Neodymium)	μ_r		1.05
Rotor Magnet Spacing Factor	k_{w1}		0.80
Slot Leakage Compensation Factor	k_{sl}		0.94
Effective Stator Length	L_{eff}	m	T-motor $0.375L$ KDE-Direct $For\ {}^{D}/_{L} < 0.9;\ L_{eff} = 0.75L$ $For\ {}^{D}/_{L} \geq 0.9;\ L_{eff} = 0.525L$ $For\ Q > 13$ N-m; $L_{eff} = 0.85L$
Fundamental Winding Factor	k_{w1}		0.933
Slot Fill Factor	f_s		For Sinusoidal Winding $f_s = 0.45$ For Trapezoidal Winding $f_s = 0.65$
Magnet Density	ρ_m	kg/m^3	7500
Copper Density	ρ_{cu}	kg/m^3	8920
Iron Density	ρ_{fe}	kg/m^3	7750
Maximum Torsional Stress	σ	Pa	250E6 (steel)

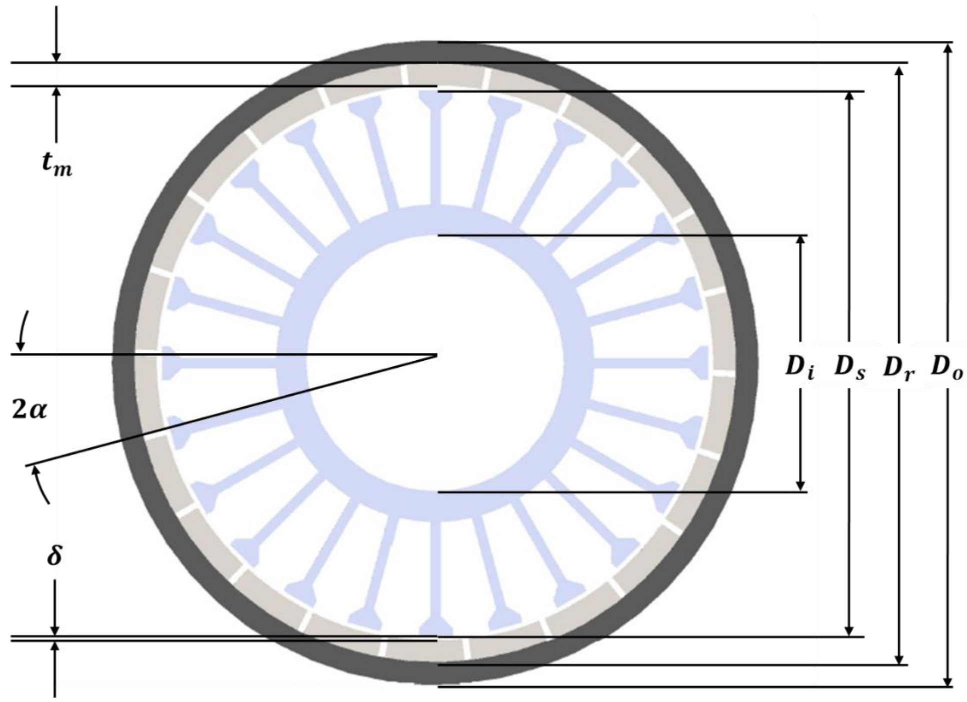

Figure 5.39. Principal motor geometric parameters

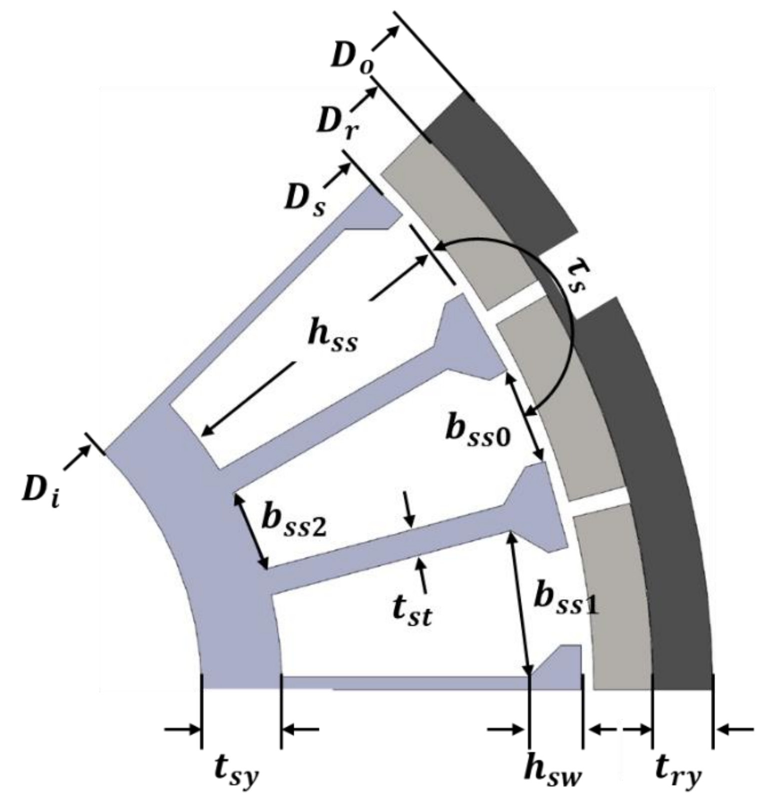

Figure 5.40. Detailed motor slot parameters

To form the motor geometry, the outer rotor diameter (D_o) is specified as a user specified input. Then the first iterative parameter, magnet thickness (t_m) in meters, is initialized. The magnet thickness influences the airgap flux density as well as the magnet weight. To reduce the number of iterative parameters, rotor yoke thickness (t_{ry}) is calculated as a function of the magnet thickness. Then the inner rotor diameter is calculated completing the rotor geometry, Equation 5.112.

$$\begin{cases} t_{ry} = t_m \\ D_r = D_o - 2t_{ry} \end{cases} \tag{5.112}$$

The airgap between the rotor and the stator allows unobstructed movement of the rotor but also influences the airgap flux density. As such, the second iterative parameter, airgap thickness (δ) in meters, is initialized. The airgap thickness is used to calculate the outer stator diameter (D_s) and slot pitch (τ_s) as in Equation 5.113. N_{slot}, the number of slots, is fixed at 12 to reduce variables for this research.

$$\begin{cases} D_s = D_r - 2t_m - 2\delta \\ \tau_s = \pi \frac{D_s}{N_{slot}} \end{cases} \tag{5.113}$$

To complete the motor geometry, the stator geometry is needed. The slot area of the stator determines the area of the copper windings and the current density of the motor. To calculate slot area, two additional iterative parameters are utilized, slot height (h_{ss}) and slot tooth thickness (t_{st}). The third iterative parameter, slot height (h_{ss}) in meters, is initialized. To minimize weight while ensuring geometric rigidity the stator yoke thickness (t_{sy}) is calculated as a function of the slot height (h_{ss}). Then with the stator yoke thickness and slot height, the inner diameter of the stator is calculated as in Equation 5.114.

$$\begin{cases} t_{sy} = f_{sy} h_{ss} \\ D_i = D_s - 2t_{sy} - 2h_{ss} \end{cases} \tag{5.114}$$

The second variable for slot area, slot tooth thickness (t_{st}), is next initialized. Then the outer slot bore width (b_{ss1}), inner slot bore width (b_{ss2}), and slot area (A_s) are calculated as in Equation 5.115. Here, the slot tooth height (h_{sw}) is fixed at 0.5 mm to minimize weight.

$$\begin{cases} b_{ss1} = \pi \frac{D_s - 2h_{sw}}{N_{slot}} - t_{st} \\ b_{ss2} = \pi \frac{D_s - 2h_{ss}}{N_{slot}} - t_{st} \\ A_s = {}^{1}\!/_{2}\,(b_{ss1} + b_{ss2})(h_{ss} - h_{sw}) \end{cases} \tag{5.115}$$

Prior to calculating the magnetic properties of the motor, the motor geometry is compared with the geometric constraints given in Table 5.8. The geometric constraints ensure motor integrity [24]. If the motor does not meet the geometric constraints the slot tooth thickness, slot height, airgap thickness, and magnet thickness are iterated, shown in Table 5.8, until they are met.

Table 5.7. Iterative parameters and iteration range (in order of appearance)

Variable	Symbol	Unit	Range
Magnet Thickness	t_m	m	$0.001 - 0.15$
Airgap	δ	m	$0.001 - 0.15$
Stator Slot Height	h_{ss}	m	$0.1D_s - 0.3D_s$
Slot Tooth Thickness	t_{st}	m	$0.3\tau_s - 5.0\tau_s$
Slot Tooth Bore Width	b_{ss0}		$0.1b_{ss1} - 0.9b_{ss1}$

Next, the maximum flux density is calculated for the magnetic properties of the motor. To calculate the maximum flux density, the Carter factor (k_c) and the flux leakage coefficient (k_{leak}) are first calculated. The Carter factor requires the final iterative parameter, the slot tooth bore width (b_{ss0}) in meters, be initialized [26]. The flux leakage coefficient is determined using a linear dependency on magnet number, N_{mag} for external rotor motors [24]. To reduce variables for this research, the number of magnets is fixed at 14. The maximum flux density can then be calculated by Equation 5.116. Here B_r, the remanence flux density of the magnet, and μ_r, the relative magnetic permeability of the magnet, are fixed parameters for a typical neodymium magnet.

Table 5.8. Geometric, magnetic, and electrical constraints (in order of appearance)

Variable	**Symbol**	**Unit**	**Range**
	Geometric		
Inner Slot Bore Width	b_{ss2}	m	$0.15h_{ss} \leq b_{ss2} \leq 0.5h_{ss}$
Slot Tooth Bore Width	b_{ss0}	m	$b_{ss0} \geq 0.0005$
	Magnetic		
Airgap Flux Density	B_δ	Tesla	$B_\delta \leq 1.1$
Rotor Yoke Flux Density	$B_{\delta ry}$	Tesla	$B_{ry} \leq 1.4$
Stator Yoke Flux Density	B_{sy}	Tesla	$B_{sy} \leq 1.4$
	Electrical		
Current Density	J	A/m	$J \leq$12.5E6

$$\begin{cases} k_c = \dfrac{\tau_s}{\tau_s - \frac{(b_{ss0})^2}{b_{sso}+5\delta}} \\ k_{leak} = 1.03 - 0.00233N_{mag} \\ B_m = \dfrac{B_r k_{leak}}{1 - \frac{\mu_r \delta k_c}{t_m}} \end{cases} \tag{5.116}$$

Finally, the air gap flux density (B_δ), stator yoke flux (B_{sy}), and rotor yoke flux (B_{ry}) are calculated as in Equation 5.117 [22, 24]. Here k_{rm}, the rotor magnet spacing factor, is a fixed parameter. Prior to calculating the electric properties of the motor, the magnetic fluxes are compared with the magnetic constraints given in Table 5.6. The magnetic constraints prevent magnet saturation of a neodymium magnet [24, 25]. If the motor does not meet the magnetic constraints the slot tooth bore width is iterated, shown in Table 5.8, until they are met.

$$\begin{cases} B_\delta = \frac{4}{\pi} B_m sin\left(\frac{\pi k_{rm}}{N_{mag}}\right) \\ B_{sy} = \dfrac{B_\delta(D_s+\delta)}{D_i+h_{sy}} \\ B_{ry} = \dfrac{B_\delta(D_s+\delta)}{D_r+h_{ry}} \end{cases} \tag{5.117}$$

Next the maximum continuous torque (Q) and motor core length (L), i.e., length without the shaft) are specified. The current density is calculated as a function of the torque, airgap flux density, and slot geometry per Equation 5.118. Here, k_{sl} is the slot leakage loss compensation factor for an outer rotor configuration (0.94), $L_{eff}$is the length of the stator (a function of motor core length as shown in Table 5.6), k_{w1} is the fundamental winding factor (as calculated for a 12 slot, 14 magnet motor), and f_s is the slot fill (fixed at 0.65 for trapezoidal motors, and 0.45 for sinusoidal motors) [26-28]. Prior to calculating the weight of the motor, the current density is compared with the electric constraints given in Table 5.8. The electric constraints ensure the motor has proper thermal management [23, 25]. If the motor does not meet the electric constraints, the slot tooth bore width is iterated, Table 5.8, until they are met.

$$J = \frac{4Q\tau_s}{k_{sl}\pi(D_s+\delta)^2 L_{eff} k_{w1} B_\delta N_{slot} A_s f_s \sqrt{2}} \tag{5.118}$$

The final step is to calculate the component weights. The magnet weight, W_{mag}, is a function of the density of the neodymium magnet, ρ_m, the magnet spacing factor, and the magnet volume as in Equation 5.119. The copper weight,W_{cu}, is a function of the density of copper, ρ_{cu}, the number of slots, the slot fill factor, slot area, and the winding length ($L_{eff} + \tau_s$) as in Equation 5.120. The iron weight, W_{fe}, is a function of the iron density, ρ_{fe}, the stator volume, and the rotor yoke volume as in Equation 5.121.

$$W_{mag} = \rho_m k_{rm} \frac{\pi L_{eff}\left(D_r^2 - (D_r - t_m)^2\right)}{4} \tag{5.119}$$

$$W_{cu} = \rho_{cu} N_{slot} f_s A_s \left(L_{eff} + \tau_s\right) \tag{5.120}$$

$$W_{fe} = \rho_{fe}\left(\frac{\pi\left(D_S^2 - D_i^2\right)}{4} - A_s N_{slot}\right) + \rho_{fe}\left(\frac{\pi\left(D_o^2 - D_r^2\right)}{4}\right) \tag{5.121}$$

In addition to the magnet, copper, and iron weights the model includes steel shaft and bearing weight, W_{SB}, as well as, aluminum bearing support and shell weight, W_{al}. The steel shaft diameter, D_{sft}, is sized for a maximum torque three times the maximum continuous torque with a minimum diameter of 8 mm. Here, σ is the maximum torsional stress for steel (250 MPa). The shaft is assumed to be 1.5 times the length of the motor. The motor is assumed to have two steel bearings with an aspect ratio of 2:1 based on the shaft diameter. The steel shaft and bearing weight, W_{SB}, a function of the iron density, ρ_{fe}, the shaft volume, and the total bearing volume, Equation 5.122.

$$\begin{cases} D_{sft} = \max\left(0.008m, \sqrt[3]{\frac{48\,Q}{\sigma\pi}}\right) \\ W_{SB} = \rho_{fe}\left(1.5L\frac{\pi D_{sft}^2}{4} + \frac{3\pi D_{sft}^3}{2}\right) \end{cases} \tag{5.122}$$

The bearings are supported by an aluminum support structure and the motor is encapsulated in a semi-protective casing. The bearing structures are assumed to be half the width of the bearing and supported by the inner stator. The protective shell is assumed to be the thickness of the rotor yoke and encapsulate the motor on all side by 75%. The aluminum weight is a function of the aluminum density, ρ_{al}, the bearing support volume, and the casing volume as shown in Equation 5.123.

$$W_{al} = \rho_{al}\left(\frac{\pi D_{sft}\left(D_i^2 - D_{sft}^2\right)}{4}\right) + \frac{3\rho_{al}}{4}\left(\frac{\pi h_{ry}\left(D_o + t_{ry}\right)^2}{4} + \frac{\pi L\left(\left(D_o + t_{ry}\right)^2 - D_o^2\right)}{4}\right) \tag{5.123}$$

The total weight is the sum of each component weight as shown in Equation 5.124. The geometry is then iterated for the minimum weight within the defined iterative range.

$$W_{total} = W_{mag} + W_{cu} + W_{fe} + W_{SB} + W_{al} \tag{5.124}$$

For example, using the KDE5215XF-330, with an outer diameter of 60 mm, motor core length of 41-mm, and maximum torque of 1.794 N-m is input and iterated over the ranges shown in Table 5.7. The minimum weight of 0.358 kg occurs with a magnet thickness of 3.5 mm, airgap thickness of 1-mm, slot height of 4.8 mm, slot tooth thickness of 2.1 mm, and slot tooth bore width of 0.43 mm. When compared to the entire database, the geometric weight model has an average error of approximately 6% and a maximum error of approximately 20%. Figure 5.41 shows the motor weight, W in kg, as a function of maximum continuous torque, Q in N-m, overlaid with ±20% error bars.

$$W_{total} = W_{mag} + W_{cu} + W_{fe} + W_{SB} + W_{al} \tag{5.124}$$

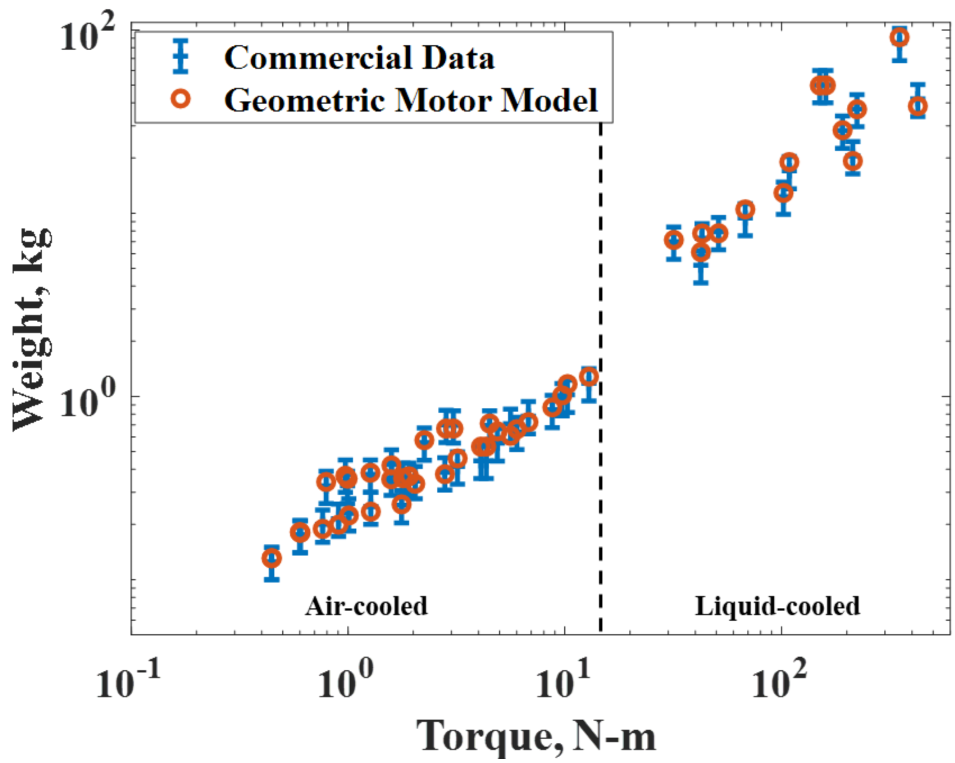

Figure 5.41. Geometric motor weight as a function of maximum continuous brake torque with 20% error boundaries for 49 motors

5.5.1. Electronic Speed Controller Weight Model

The AC PMS motors used in eVTOL typically draw power from a DC source and are controlled by an ESC or inverter. As such electric aircraft design methodologies should include ESC weight models. A curve fit with an average error of approximately 23%, Equation 5.125, is made of 45 commercial ESCs, collected from open-source engine specifications, ranging from 0.4 kW to 360 kW. In Equation 5.125, the ESCs are categorized with air-cooled and liquid cooled models. Figure 5.40 shows the ESC weight, W in kg, as a function of maximum continuous power, P in kW, with dashed 20% error lines.

$$\begin{cases} W_{ESC} = 0.04972\ P^{0.7897}\ Air\ cooled \\ W_{ESC} = 0.4655\ P^{\,0.6188}\ Water\ cooled \end{cases} \tag{5.125}$$

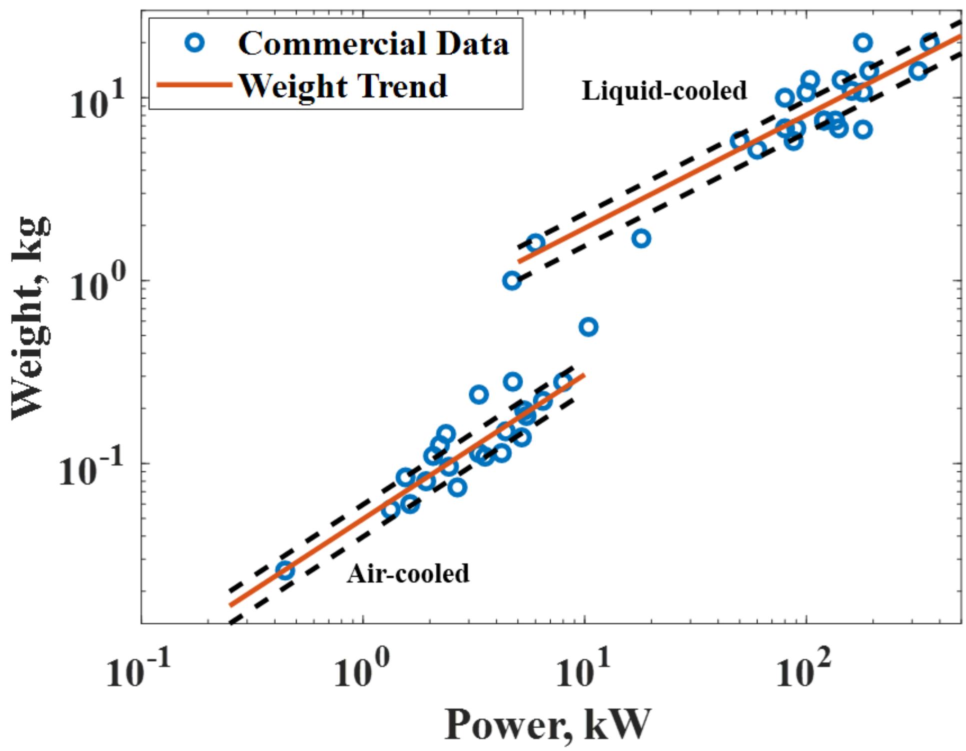

Figure 5.42. ESC/inverter weight verses maximum continuous power with predicted weight trends and 20% error boundaries for 45 ESCs

5.6. Chapter Summary and Conclusions

In this chapter, performance models and weight models were developed for AC PMS motors and generators. It was found that the 3-phase performance model can be accurately reduced to the DC equivalent model that is adequate for conceptual sizing and performance of an aircraft. The 3-phase model is still need for capturing high-frequency phase and control commutation ripples hence for power system analyses. It was found that complex phenomena such as aerodynamic drag and flux weakening are required to model the efficiency contours in detail. A weight versus torque trend was found with 49 commercial motors, with an average error less than 30%. However, due to the significant impact of hub weight in helicopter sizing, an alternative to a trendline is needed for first principal designs. As such a geometric and material-based motor weight was developed and validated. It was found to capture accurate weights within a 6% average error. As these motors require inverters (e.g., ESC), a weight versus power trend line was also constructed with 45 commercial controllers, with an average error of 23%. It was found that when AC PMS motors/generators and their controller are examined as a whole, the engine cooling schemes can significantly affect the weight trends. Thus, two sets of trendlines were given: one for air-cooled, another for liquid-cooled.

Chapter 6: Integrated Powertrain Model

This short chapter examines the integrated powertrain performance and weights. Until this point, only the individual components have been modeled. These are now unified within into a single powertrain model. The mechanical and electrical connections, outlined in Figure 2.1, are replicated through data connections integrating the models. The integrated weight model utilizes the component weight models and incorporates engine accessories.

6.1. Integrated Performance Model

The goal of the integrated model is to predict the fuel efficiency of the engine as a function of output rotor torques and speeds for a specified DC bus voltage. A specified DC bus voltage, as well as rotor torque and RPM are input for each of the four motors; although, for this research all experiments were performed with the same torque and RPM on all motors. The AC PMS motor module predicts the current required. The AC PMS generator module then predicts the engine torque and RPM at the specified DC bus voltage. Finally, the engine module predicts the bsfc. Simulation of the full system requires 3 additional motors to be programmed in parallel with the first motor, potentially adding 21 additional constants if the motor constants were different. However, for this work the same constants were used for all motors.

Figures 6.1 and 6.2 plots the predicted fuel efficiency as a function of rotor power for a specified DC bus voltages of 25- and 50 V. The predicted fuel efficiency with constant rotor torque (dotted) and RPM lines (dash-dot) are overlaid on the experimental fuel efficiency, with constant rotor torque (dashed) and RPM lines (solid) marked. The predictions remain consistent between the data. The largest predicted bsfc errors (~2%) are at 50-V as that is nearest to an RPM boundary. The conclusions from the data remained valid with the simulation. Most importantly, that the generator voltage is a key parameter in hybrid-electric. Also, that for any generator voltage and rotor RPM there is a rotor torque that maximizes overall efficiency, i.e., minimizes specific fuel consumption. Thus, collective pitch control is desired for the rotor blades.

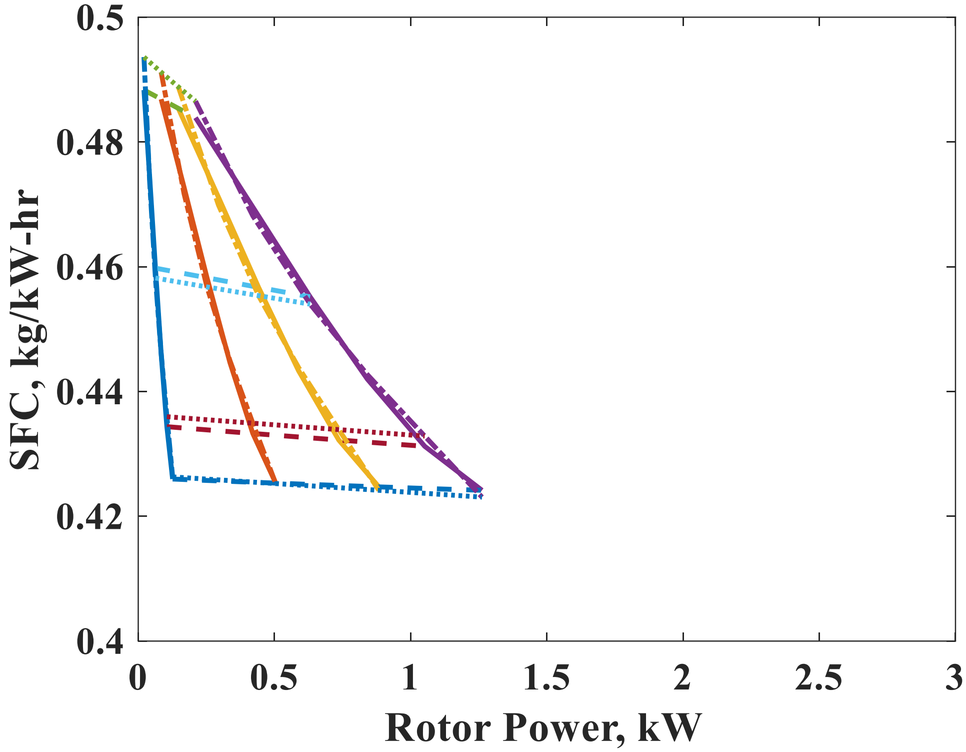

Figure 6.1. Engine specific fuel consumption versus rotor power with predicted (dotted, dash-dot) and measured (solid, dashed) constant rotor RPM and torque contours at 25-V DC voltage

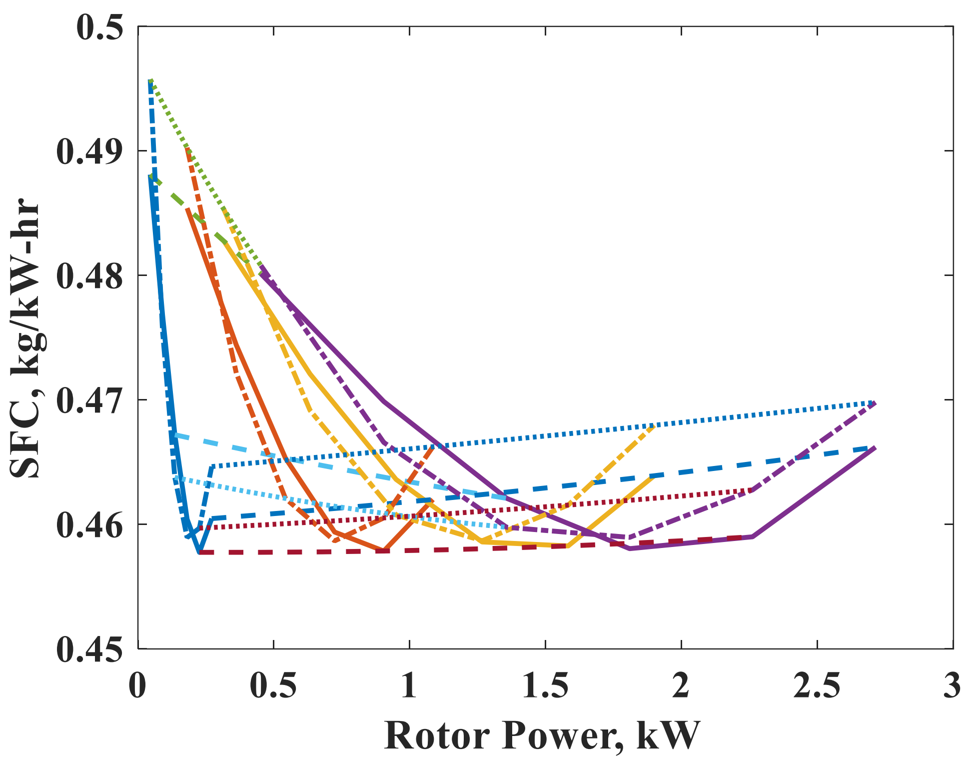

Figure 6.2. Engine specific fuel consumption versus rotor power with predicted (dotted, dash-dot) and measured (solid, dashed) constant rotor RPM and torque contours at 50-V DC voltage

6.2. Integrated Weight Model

The predicted weight of the integrated powertrain was calculated with the previously mentioned weight models. Powerplant accessories were assumed to weight 20% of the predicted engine weight [29, 30]. Table 6.1 shows the weight breakdown of the experimental powertrain, and the component weight estimates from the weight models. The engine and the electric motors were over predicted by 20%. The greatest component error came from the powerplant accessories. These are approximately 80% of the engine weight and approximately 20% of the total powertrain weight.

Table 6.1. Integrated Powertrain Weight Comparison

	Integrated Powertrain		Predicted Weight		Error	
Engine	DLE-40cc Twin 1.272 kg		3.5 kW engine 1.460 kg		+17.7 %	
Generator	KDE7215 XF-135 0.640 kg	KDE700 XF-295-G3 0.695 kg	6.01 N-m L=44.5 mm D_o=80.8 mm 0.663 kg	4.5 N-m L=74.7 mm D_o=56 mm 0.712 kg	+3.6 %	+2.4 %
Rectifier	MDS200A 0.403 kg		12.5 kW 0.365		– 9.4%	
Electric Motor	KDE7208XF-110 x4 0.445 kg x4		4.34 N-m L=35 mm D_o=80 mm 0.532 kg x4		+19.6 %	
ESC	KDEXF-UAS75HVC x4 0.114 kg x4		3.33 kW ESC 0.129 kg x4		+ 13.2 %	
Fuel Tank	VVRC 32 oz Tank 0.136 kg					
Fuel Line	Tygon Tubing 0.08 kg					
Flywheel	Fabricated 0.36 kg					
Ignition Control Module	DLE Model A-02 Ignition 0.149 kg		Powerplant Accessories (20% engine weight) 0.292kg		– 65.4 %	
Ignition Battery	6V 2500mAh NiMH 0.142 kg					
Shaft Coupler	Fabricated 0.07 kg					
Wiring	Fabricated 0.095 kg					
Total Weight	5.583 kg	5.638 kg	5.424 kg	5.473 kg	– 2.8 %	– 2.9 %

6.1. Chapter Summary and Conclusion

Using the variable calibrations from chapters 4 and 5, the predicted specific fuel consumption error of the integrated drivetrain was largest (<5%) at the engine lower torque boundary and the upper RPM boundary. Therefore, the performance models described are capable of capturing the accurate magnitudes and trends of the system performance. As a result, the key conclusions from the experimental characterization were captured by the simulation. The most important of which is that generator voltage is the crucial parameter in a rotorcraft hybrid-electric powertrain. Additionally, for any generator voltage and rotor RPM there is a rotor torque that maximizes overall efficiency, i.e., minimizes specific fuel consumption. Thus, collective pitch control is needed on the rotor blades. The weights are predicted within ±20%. The accessory overhead is approximately 80% of the engine weight and approximately 20% of the integrated powertrain weight.

Chapter 7: Summary and Conclusions

In this research, a variable-voltage hybrid-electric powertrain was constructed and tested to acquire data and understand the fundamental behavior of the system. Experiments were conducted to examine the powertrain component by component, as well as in combination with one and four distributed propulsors. Electrical load banks and a series of propellers were used to control loading. Chapter 1 introduced the motivation of the research, provided a description of the problem, and gave a survey of past work. Chapter 2 described the design and fabrication of the 4-kW, variable-voltage hybrid electric powertrain. It included descriptions of the powertrain architecture, components (engine, generator, motors, power electronics), and. Chapter 3 described the experiments. Three types of tests of progressively increasing complexity were conducted: 1) isolated engine-generator tests, 2) engine-generator tests with one electric drive, and 3) engine-generator tests with four electric drives.

Models for predicting engine fuel consumption and weight need for the design of a hybrid-electric aircraft were developed in Chapter 4. Chapter 5 developed models for motor/generator performance and weight for the design of a hybrid-electric aircraft. Finally, Chapter 6 examined the integrated powertrain performance and weights. The integrated weight model utilized the component weight models from Chapter 4 and 5 and incorporated engine accessories. Based on this work, the following conclusions are drawn. They are listed in the order they appear in the dissertation, not the order of importance.

7.1. Conclusions

The key conclusions of this dissertation are the following.

1. Small engines (below 5kW) typically lack integrated starters and must rely on external starter drives that attach to a propeller. However, in distributed electric propulsion, the propeller is mechanically isolated from the engine. Typically, these engines also lack an integrated flywheel to store energy for the compression stroke and utilize the propeller instead to provide this function. The generator typically lacks the mass moment of inertia to complete the compression stroke. Thus, a proper starting mechanism must be designed for in-flight operation.
2. Generator voltage is a key parameter in a hybrid-electric powertrain. The ability to vary this voltage with rotor operating state appears crucial for the optimal specific fuel consumption. Generator voltage is a function of engine speed. Thus, varying engine speed is important, varying rotor speed through the ESC alone is not optimal and can lead to poor overall performance.
3. For any operating state—defined by rotor torque and RPM—the generator voltage should be the minimized as far as possible. The generator voltage limits the maximum rotor RPM, so not all rotor RPM can be achieved at the same generator voltage. Hence, the best generator voltage will vary with rotor RPM as needed during a certain mission segment. This implies for an RPM controlled aircraft, generator voltage is not simply a criterion for design but also for control, if the best specific fuel consumptions are to be achieved.
4. For any generator voltage and rotor RPM, there is a rotor torque that maximizes overall efficiency, i.e., minimizes specific fuel consumption. A method for adjusting the rotor torque, such as collective pitch control is also desired if the best specific fuel consumption is to be achieved.

5. For an integrated powertrain, specific fuel consumption is a function of generator voltage (i.e., engine speed), rotor RPM, and rotor torque—in that order of importance. By analyzing a reduction in power scenario representing a hover-to-cruise transition, it was found that the most efficient change in power results from a combination of reducing engine RPM and increasing rotor torque, and vice versa.
6. Greater torque and lower RPM are generally desired from rotors of a hybrid-electric aircraft because the overall system is influenced more by the engine-generator than the electric motor. This mode of operation is fundamentally different from an all-electric drive, where lower torque and higher RPM is normally the most beneficial
7. Of all the principal components for the system—engine, generator, and motors—the generator appears crucial for achieving maximum power at a given rotor RPM. Given an engine and a set of motors, the generator should be selected or designed for the maximum current corresponding to the maximum rotor torque desired at a certain RPM. Improper selection of the generator can result in a rotor starved of torque.
8. Unsteady gas dynamics and transient thermodynamic effects are required to model the engine in detail. These effects can be captured by a simple physic-based model of bsfc contours if the thermal efficiency is calibrated with experimental data. After calibration the predicted bsfc error was largest (~2%) at the engine lower torque boundary and the upper RPM boundary.
9. The weight versus power trend found with 72 commercial engines showed an average error of 20%. It was found that when reciprocating engines are examined as a whole (i.e., 2-stroke, 4-stroke, diesel, gasoline), the engine core material can

significantly affect the weight trends. Engines below 30 kW power almost exclusively use aluminum cores compared to the iron/steel cores used at higher powers.

10. A 3-phase performance model can be accurately reduced to a single-phase DC equivalent model that is adequate for conceptual sizing and performance of an aircraft. The 3-phase model is still needed for power system analyses.
11. Complex phenomena such as aerodynamic drag and flux weakening are required to model the electric drive performance more accurately.
12. The weight versus torque trend found with 49 commercial motors showed an average error of 20%. The geometric and material-based motor weight developed displayed a 6% average error.
13. The weight versus power trend of the ESC from 45 commercial controllers showed an average error of 23%.
14. The predicted specific fuel consumption error of the integrated drivetrain model was largest (<5%) at the engine lower torque boundary and the upper RPM boundary. Therefore, the performance models described are capable of capturing the accurate magnitudes and trends of the system performance. As a result, the key conclusions from the experimental characterization were captured by the simulation.
15. The generator voltage is the crucial parameter in a rotorcraft hybrid-electric powertrain.

16. For any generator voltage and rotor RPM there is a rotor torque that maximizes overall efficiency, i.e., minimizes specific fuel consumption. Thus, collective pitch control is needed on the rotor blades.

7.2. Contributions of Presented Research

This research presented one of the first fundamental characterization of a variable-voltage hybrid-electric powertrain for eVTOL aircraft. The key contributions are listed as follows:

1. A new 4-kW, hybrid-electric test capability was built at the University of Maryland
2. Data at over 500 points were collected
3. It was established that design and operation of the powertrain is closely coupled to the aircraft.
4. Detailed engine, motor, and generator models were developed and validated. These can be used for future aircraft design.

7.3. Future Work

Future work should focus on incorporating engines and architectures of increasing scale and performance. These include

1. 4-stroke and heavy-fuel reciprocating engines and thereafter turboshaft like engines
2. Incorporation of additional DC power sources for strategic needs, such as batteries or capacitors for transient power requirements.
3. The 4-kW powertrain was meant for a 50-lb VTOL UAS. In the future, this avenue should be pursued, and flight testing conducted.

Chapter 8: Bibliography

[1] Dean, F., Curtiss X-Planes: Curtiss-Wright's VTOL Effort 1958-1965, Schiffer Publishing Ltd, Atglen, 2001.

[2] Rhodes, W., "Initial military flight tests of the X-22A VSTOL research aircraft," *Journal of Aircraft*, Vol. 7, No. 2, Mar 1970, pp. 169-174.
https://doi.org/10.2514/3.44142

[3] Josephs III, L. and Hesse, W., "Survey of significant technical problems unique to VSTOL encountered in the development of the XC-142A," *Journal of Aircraft*, Vol. 3, No. 1, Jan 1966, pp. 3-10.
https://doi.org/10.2514/3.43699

[4] Gohardani, A., "A synergistic glance at the prospects of distributed propulsion technology and the electric aircraft concept for future unmanned air vehicles and commercial/military aviation," *Progress in Aerospace Sciences*, Vol. 57, Feb 2013, pp. 25-70.
https://doi.org/10.1016/j.paerosci.2012.08.001

[5] Datta, A, and Johnson, W. "Powerplant design and performance analysis of a manned all-electric helicopter," *Journal of Propulsion and Power*, Vol. 30, No. 2, Mar 2014, pp. 490-505.
https://doi.org/10.2514/1.B34843

[6] Friedrich, C., and Robertson P. "Hybrid-electric propulsion for automotive and aviation applications," *Council of European Aerospace Societies Aeronautical Journal*, Vol. 6, No. 2, Jun 2015, pp. 279-290.
https://doi.org/10.1007/s13272-014-0144-x

[7] Friedrich, C., and Robertson P "Hybrid-electric propulsion for aircraft," *Journal of Aircraft*, Vol. 52, No. 1, Jan 2014, pp. 176-189.

https://doi.org/10.2514/1.C032660

[8] Brown, S., and Hagen, C. “Optimized Engine Performance for a 1 KW UAV Hybrid Powertrain,” ASME Paper ICEF2017-3555, Proceedings of Internal Combustion Engine Division Fall Technical Conference, Seattle, WA, October 15-17, 2017.

[9] Dehesa, D., Menon, S., Brown, S., and Hagen, C. “Dynamic Analysis of a Series Hybrid–Electric Powertrain for an Unmanned Aerial Vehicle,” *Journal of Propulsion and Power*, Vol. 38, No. 1, Jan 2022, pp. 84-96.

https://doi.org/10.2514/1.B38261

[10] Ricci, M., Varahamurthy, V., and Hicks, R., “Power System Characterization and Flight Testing of a >55 lb Hybrid-Electric Multirotor,” Proceedings of the American Helicopter Society 78th Forum, Ft. Worth, TX, May 10-12, 2022.

[11] Mi, C., and Masrur, M., Hybrid electric vehicles: principles and applications with practical perspectives, 2nd ed., John Wiley & Sons, Hoboken 2017.

[12] Doateo T., Carla, A., and Avanzini, G. “Fuel consumption of rotorcrafts and potentiality for hybrid electric power systems,” *Energy Conversion and Management,* Vol. 164, May 2018, pp 429-442.

https://doi.org/10.1016/j.enconman.2018.03.016

[13] Wall, T. and Meyer, R., “Hybrid Electric Aircraft Switched Model Optimal Control,” *Journal of Propulsion and Power*, Vol. 36, No. 4, Jul 2020, pp. 488-497.

https://doi.org/10.2514/1.B37419

[14] Voskuijl, M., van Bogaert, J., and Rao, A. G., “Analysis and Design of Hybrid Electric Regional Turboprop Aircraft,” *Council of European Aerospace Societies Aeronautical Journal*, Vol. 9, No. 1, Mar 2017, pp. 15–25.

https://doi.org/10.1007/s13272-017-0272-1

[15] Lee, D.,Lim, D., and Yee, K. “Generic Design Methodology for Vertical Takeoff and Landing Aircraft with Hybrid-Electric Propulsion,” *Journal of Aircraft*, Vol. 59, No. 2, Mar 2022, pp. 278-292.

https://doi.org/10.2514/1.C036214

[16] Mills, B., and Datta, A. “Fundamental Studies of Variable-Voltage Hybrid-Electric Powertrains,” *Journal of the American Helicopter Society*, Vol 66, No. 2, Apr 2021, pp. 1-14. https://doi.org/10.40509/JAHS.66.022009

[17] Govindarajan, B., Sridharan, A., and Chopra, I., “A Scalability Study of the Multirotor Biplane Tailsitter using Conceptual Sizing,” Proceedings of the 74th Annual Forum & Technology Displayof the American Helicopter Society, Phoenix, AZ, May 14–17, 2018.

[18] Taylor, C., The Internal-Combustion Engine in Theory and Practice Volume I: Thermodynamics, Fluid Flow, Performance 2nd Edition, The Massachusetts Institute of Technology Press, Cambridge, 1985.

[19] Blair, G., Design and Simulation of Two-Stroke Engines, 1st ed, Society of Automotive Engineers, Inc, Warrendale, 1996.

[20] Menon, S., and Cadou, C., “Scaling of Miniature Piston-Engine Performance, Part 1: Overall Engine Performance,” *Journal of Propulsion and Power*, Vol. 29, No. 4, Jul 2013, pp. 774–787.

https://doi.org/10.2514/1.B34638

[21] Goering, C. and Cho, H., “Engine model for mapping bsfc contours”, *Mathematical and Computer Modelling*, Vol 11, Jan 1988, pp.514-518

https://doi.org/10.1016/0895-7177(88)90546-8

[22] Hendershot, J.., and Miller T. Design of brushless permanent-magnet motors, 1st ed., Magna Physics Pub., Mentor 1994.

[23] Honsinger, V. B. "Sizing Equations for electrical machinery," *Institute of Electrical and Electronics Engineers Transactions on Energy Conversion* Vol 2, No. 1, Mar 1987, pp. 116-121.

https://doi.org/10.1109/TEC.1987.4765812

[24] Karnavas, Y., Chasiotis, I. , Korkas, C.., and Amoutzidis, S.. "Modelling and multiobjective optimization analysis of a permanent magnet synchronous motor design," *International Journal of Numerical Modelling: Electronic Networks, Devices and Fields,* Vol. 30, No. 6, Nov 2017, pp. e2232.

https://doi.org/10.1002/jnm.2232

[25] Chasiotis, I. and Karnavas, Y., "A computer aided educational tool for design, modeling, and performance analysis of Brushless DC motor in post graduate degree courses," *Computer Applications in Engineering Education,* Vol. 26, No. 4, Jul 2018, pp: 749-67.

https://doi.org/10.1002/cae.21897

[26] Pyrhonen, J., Jokinen, T., Hrabovcova. V., Design of Rotating Electrical Machines, 2nd Ed., John Wiley & Sons, West Sussex, 2013.

[27] Libert, F., and Juliette S., "Investigation on pole-slot combinations for permanent-magnet machines with concentrated windings," 16th International Conference on Electrical Machines, Sep 2004, pp. 530-535.

[28] Magnussen F., and Sadarangani C., "Winding factors and Joule losses of permanent magnet machines with concentrated windings,", in Proceedings of IEEE International Electric Machines & Drives Conference (IEMDC), Vol. 1, June 2003, pp. 333–339.

[29] Harris, F. "Introduction to Autogyros, Helicopters, and Other V/STOL Aircraft Volume II: Helicopters," NASA/SP–2012-215959 Vol II, Oct 2012.

[30] Johnson, W. "NDARC NASA Design and Analysis of Rotorcraft," NASA/TP–20220000355, Jan 2022.